Standard measurement system for SI traceable measurement of high voltage pulses up to 500 kV in the nanosecond and sub-nanosecond range

Mohammad Saif Khan

université PARIS-SACLAY

Standard measurement system for SI traceable measurement of high voltage pulses up to 500 kV in the nanosecond and sub-nanosecond range

Système de mesure étalon pour la mesure traçable au SI des impulsions haute tension jusqu'à 500 kV dans le domaine nanoseconde et sub-nanoseconde

Thèse de doctorat de l'université Paris-Saclay

École doctorale n° 575, Electrical, Optical, Bio : Physics and Engineering (EOBE)
Spécialité de doctorat : Génie électrique
Graduate School : Sciences de l'ingénierie et des systèmes. Référent : CentraleSupélec

Thèse préparée dans l'unité de recherche **Laboratoire de Génie Electrique et Electronique de Paris (Université Paris-Saclay, CentraleSupélec, CNRS)** sous la direction de **Yann LE BIHAN**, Professeur à l'Université Paris-Saclay, la co-supervision de **Mohamed AGAZAR**, Ingénieur de recherche au Laboratoire national de métrologie et d'essais

Thèse soutenue à Paris-Saclay, le 9 janvier 2023, par

Mohammad Saif KHAN

Composition du Jury

Membres du jury avec voix délibérative

Eric LABOURE Professeur à l'Université Paris-Saclay, GeePs	Président
Charles JOUBERT Professeur à l'Université Claude Bernard Lyon 1, Ampère	Rapporteur & Examinateur
Laurent PECASTAING Professeur à l'Université de Pau et des Pays de l'Adour, SIAME	Rapporteur & Examinateur
Michael STOCK Directeur du Département de Métrologie Physique, BIPM	Examinateur

THÈSE DE DOCTORAT

NNT : 2023UPAST011

université PARIS-SACLAY
DOCTORAL SCHOOL
Electrical, Optical, Bio: Physics and Engineering (EOBE)

Titre : Système de mesure étalon pour la mesure traçable au SI des impulsions haute tension jusqu'à 500 kV dans le domaine nanoseconde et sub-nanoseconde

Mots clés : Haute puissance pulsée, étalon de mesure, diviseur de tension, étalonnage, incertitude de mesure

Résumé : Le travail de cette thèse de doctorat est dédié au développement d'un système de mesure étalon pour assurer la traçabilité SI des hautes puissances pulsées dans le domaine nanoseconde et subnanosecond (HPPNS). Cette traçabilité est nécessaire pour les mesures exactes et précises des formes d'onde de tension qui constituent l'élément clé des systèmes basés sur la haute puissance pulsée. Un système d'étalonnage a été développé pour la caractérisation d'impulsions haute tension d'amplitudes jusqu'à 500 kV avec des temps de montée aussi faibles que quelques centaines de picosecondes.

Le système de mesure HPPNS développé est divisé en quatre composants : le diviseur de tension, la charge de terminaison, les connecteurs haute tension et les cônes de transition. Le diviseur de tension est le composant central de ce système de mesure car il permet l'analyse des formes d'onde HPPNS à travers un oscilloscope calibré en abaissant les amplitudes de tension des formes d'onde HPPNS à des niveaux adéquats qui peuvent être mesurés à travers un oscilloscope sans déformation de forme d'onde. Le diviseur de tension conçu par calculs analytiques et numériques a une valeur élevée du rapport de division qui est relativement constante en fonction de la fréquence jusqu'à au moins 2 GHz, ainsi que des réponses de phase linéaires. Cependant, ses performances en termes de mesure exacte et précise des formes d'onde HPPNS incidentes dépendent également des caractéristiques de la charge de terminaison de ligne de transmission puisque les réflexions d'une charge de terminaison de ligne insuffisamment adaptée pourraient conduire à une mauvaise interprétation de la forme d'onde mesurée à la sortie du diviseur. Une charge de terminaison de ligne de 50 Ω est développée et caractérisée. Elle possède des propriétés d'isolation élevées pour des amplitudes de tension jusqu'à 500 kV et un coefficient de réflexion maximum de -27 dB en fonction de la fréquences jusqu'à 2 GHz.

La caractérisation du système de mesure HPPNS complet a été réalisée en deux étapes. Premièrement, le système de mesure HPPNS a été caractérisé à de faibles niveaux de puissance d'entrée par deux méthodes différentes, à savoir la caractérisation au VNA et la caractérisation par une méthode de mesure d'atténuation haute fréquence traçable au SI. Les résultats obtenus à partir de ces deux méthodes ont été comparés aux résultats de la modélisation CST et tous ces résultats se sont avérés en bon accord les uns avec les autres. Ces caractérisations ont démontré que le système de mesure HPPNS développé possède un rapport de division élevé d'environ 85 dB, une bande passante de 2 GHz et une réponse de phase linéaire. De plus, un atténuateur commercial ayant une bande passante de 7 GHz a été ajouté en sortie du diviseur et tout ce système a été re-caractérisé par les deux méthodes basse puissance. Les résultats obtenus sont les suivants : près de 110 dB de rapport de division, un bande passante de 2 GHz et une réponse de phase linéaire. Dans la deuxième étape de caractérisation, ce système a été testé à des niveaux de puissance élevés via un générateur de Marx. Différentes formes d'onde haute tension de pics de tension aussi élevés que 300 kV et de temps de montée aussi bas que 420 picosecondes ont été mesurés avec succès grâce à ce système et un budget d'incertitude a été établi. Les incertitudes de mesure pour ces mesures à haute tension ont été calculées à 3,4 % pour les pics de tension et à 87 picosecondes pour les paramètres temporels.

Title : Standard measurement system for SI traceable measurement of high voltage pulses up to 500 kV in the nanosecond and sub-nanosecond range

Keywords : High pulsed power, measurement standard, voltage divider, calibration, measurement uncertainty

Abstract : The work of this PhD thesis is dedicated to developing a standard measurement system to ensure the SI traceability of high pulsed power in the nanosecond and subnanosecond domain (HPPNS). This traceability is mandatory for the accurate and precise measurements of the voltage waveforms which constitutes the key element of systems based on high pulsed power. A calibration system has been developed for the characterization of high voltage pulses of amplitudes up to 500 kV with rise times as low as few hundreds of picoseconds.

The developed HPPNS measurement system is divided into four components: The voltage divider, the termination load, the high-voltage connectors, and the transition cones. The voltage divider is the central component of this measurement system as it permits the analysis of HPPNS waveforms through a calibrated oscilloscope by lowering the voltage amplitudes of the HPPNS waveforms to adequate levels which could be measured through an oscilloscope and without waveform deformation. Some voltage dividers of the scientific literature are discussed and compared. The voltage divider designed through analytical and numerical calculations has a high value of the division ratio which is relatively constant as a function of frequency up to at least 2 GHz, together with a linear phase response. However, its performances in terms of measuring accurately and precisely the incident HPPNS waveforms depend also on the characteristics of the transmission line termination load since the reflections from an inadequately matched line termination load could lead to the misunderstanding of the measured waveform at the output of the divider. A 50 Ω line termination load is developed and characterized. It has high insulation properties for voltage amplitudes up to 500 kV and a maximum reflection coefficient of -27 dB as a function of frequencies up to 2 GHz.

The characterization of the complete HPPNS measurement system was carried out in two steps. Firstly, the HPPNS measurement system was characterized at low levels of input power by two different methods, namely, VNA characterization and characterization through a SI traceable high frequency attenuation measurement method. The results obtained from these two methods were compared to the CST modelling results and all of these results were found to be in good agreement with each other. These characterizations demonstrated that the developed HPPNS measurement system possesses a high division ratio of around 85 dB, a bandwidth of 2 GHz, and a linear phase response. Furthermore, a 7 GHz bandwidth commercial attenuator was added at the output of the divider and this whole system was re-characterized by both low power methods. The results obtained are as follows: almost 110 dB of division ratio, a bandwidth of 2 GHz and a linear phase response. In the second characterization step, this system was tested at high power levels through a Marx generator. Different high voltage waveforms of voltage peaks as high as 300 kV and rise times as low as 420 picoseconds were successfully measured through this system and an uncertainty budget is drafted. The measurement uncertainties for these high voltage measurements were calculated to be 3.4 % for the voltage peaks and 87 picoseconds for the temporal parameters.

Remerciements

Tous mes remerciements aux personnes qui ont cru en moi et qui m'ont permis de mener à terme cette thèse qui s'est déroulée au sein de deux laboratoires : le Laboratoire National de métrologie et d'Essais (LNE) et le laboratoire de Génie électrique et électronique de Paris (GeePs).

Ce travail n'aurait jamais pu être mené à terme sans l'encadrement de M. Yann Le Bihan, Professeur à l'Université Paris-Saclay, et de M. Mohamed Agazar, Ingénieur de recherche au LNE.

Je tiens à adresser un grand merci à mon directeur de thèse Yann pour son aide précieuse et ses conseils qui auront largement contribués à l'accomplissement de ce travail. Ses compétences, sa rigueur scientifique et sa clairvoyance m'ont beaucoup apporté. Elles ont été et resteront des moteurs de mon travail de chercheur. J'ai aussi énormément apprécié ses qualités humaines, son enthousiasme et son implication tout au long de ce travail doctoral. Je remercie également mon co-encadrant Mohamed. Je lui suis reconnaissant pour la confiance et l'autonomie qu'il m'a accordées pendant ce travail doctoral.

Je tiens à exprimer mes plus vifs remerciements à mes collègues de l'atelier mécanique du LNE pour les conseils et pour la qualité des réalisations des différentes pièces du système de mesure étalon développés dans le cadre de cette thèse. Je pense en particulier à : Tony Delauney, Michael Coince, Fabrice Becuwe, Thierry Cernic et Maurice Camus.

J'adresse toute ma gratitude à mes collègues Patrick Espel, Djamel Ziane et Matthieu Thomas de l'équipe Balance du Watt du LNE pour leurs aides dans le traitement des données et la rédaction de ce manuscrit et pour la préparation et l'organisation de la soutenance de la thèse. Par la même, j'adresse mes remerciements à mes collègues du département métrologie électrique haute fréquence du LNE, spécialement à Alexis Litwin, Remy Picou, Omer Moreau, Alain Dursent, François Ziadé et Jean-Marie Lerat, pour leurs implications lors de la caractérisation haute fréquence du système de mesure développé. Je n'oublie pas Emmanuel Patois et Soureche Soccalingame pour leurs aides inestimables dans le traitement des données.

Je remercie M. Charles Joubert, Professeur à l'Université Claude Bernard Lyon 1 et M. Laurent Pecastaing, Professeur à l'Université de Pau et des Pays de l'Adour, qui

ont accepté d'examiner mon travail et d'en être les rapporteurs. Je suis reconnaissant à M. Eric Labouré, Professeur à l'Université Paris-Saclay pour l'honneur qu'il m'a accordé en acceptant de présider le jury de ma thèse. Je tiens aussi à remercier M. Michael Stock du Bureau International des Poids et Mesures (BIPM) pour sa participation en tant qu'examinateur.

J'exprime mes remerciements amicaux à M. Claude Marchand, directeur du GeePs pour l'accueil bienveillant dans son laboratoire. J'en profite pour remercier amicalement tous les collègues pour leur soutien et sympathie.

Mes remerciements s'adressent également à M. Hubert Berry, responsable du pôle métrologie électrique du LNE pour ses encouragements, son soutien et l'opportunité qu'il m'a donnée de continuer mon projet professionnel au sein du pôle. Je remercie également M. Pierre-Jean Janin, responsable du département métrologie électrique basse fréquence où j'ai réalisé cette thèse.

Enfin, en complément de cette longue liste, j'adresse mes sincères remerciements à toutes les personnes formidables que j'ai rencontrées pendant ma thèse au LNE et au GeePs. Merci pour leur disponibilité et leur sérieux.

Résumé

Cette thèse présente le développement d'un nouveau système de mesure étalon, traçable au Système international d'unités (SI), d'impulsions haute tension de temps de monté de l'ordre de la nanoseconde et sub-nanoseconde et d'amplitude dans la gamme des 500 kV. Ce type d'impulsions constitue l'élément clé des systèmes basés sur la haute puissance pulsée.

Le chapitre 1 donne un aperçu global des technologies de haute puissance pulsée. Ce terme signifie que l'énergie est accumulée pendant une période relativement longue puis restituée en une courte période pour fournir une très grande quantité de puissance à une charge donnée, ou en d'autres termes à une application donnée. Selon les applications, la puissance micro-onde résultante est ensuite envoyée vers la cible à travers un guide d'onde ou une antenne. Par exemple, une puissance de 100 W pendant 100 ms pourra être convertie en une puissance de 1 GW pendant 10 ns de durée. Cela équivaut à la puissance d'une centrale nucléaire, même si pendant cette durée l'énergie fournie n'est que de 10 J. Les techniques de génération et de mesure de ces impulsions ainsi que leurs nombreuses applications tant sur le plan militaire que civil sont largement décrites. Historiquement, les charges typiques étaient principalement des applications liées à la défense telles que, entre autres, les diodes à faisceau de particules chargées et les plasmas. Cependant, grâce à la déclassification de cette technologie, différentes applications médicales et civiles ont vu le jour au cours des dernières décennies. Un autre avantage des systèmes basés sur cette technologie est qu'ils sont, la plupart du temps, compacts et portables. Les technologies de puissance pulsée nanoseconde et sub-nanoseconde concernent généralement des systèmes capables de produire des impulsions de forte puissance de durées allant de 10^{-11} à 10^{-7} secondes. Les appareils fonctionnant sur cette échelle de temps peuvent fournir des puissances d'impulsion de sortie allant de dizaines de mégawatts à des centaines de térawatts et ont trouvé leurs applications dans des laboratoires de niveau national ainsi que des objets de notre vie quotidienne. Parmi ces applications, citons l'imagerie médicale, la radiothérapie, le traitement du cancer, les radars à pénétration de sol (GPR), la purification de l'air, la pasteurisation des aliments, le traitement de l'eau

et des déchets, le traitement des polluants gazeux et le traitement des cendres d'incinération.

Pour la plupart de ces applications, la puissance pulsée générée doit être contrôlée avec précision pour éviter l'irradiation inutile des objets ciblés et se prémunir des effets secondaires éventuels. Ce contrôle passe par un raccordement des appareils à un étalon primaire. Aujourd'hui, cet étalon n'existe pas. L'oscilloscope est l'un des meilleurs candidats pour mesurer les paramètres électriques et temporels des impulsions. Cependant, les tensions d'entrée nominales de la plupart des oscilloscopes large bande sont limitées à des niveaux de tension de quelques volts. Ils doivent donc être associés à des diviseurs de tension ayant des rapports de division adaptés et une large bande passante. En effet, les amplitudes des tensions d'impulsion peuvent varier de quelques dizaines de kilovolts à quelques milliers de kilovolts dans la gamme de fréquences allant de dizaines de mégahertz à plusieurs gigahertz. De plus, l'intégration du diviseur dans le système doit être non invasive pour le signal mesuré. Différents types de diviseurs sont présentés et discutés dans ce chapitre.

Les utilisateurs de systèmes impulsionnels haute puissance, dans la plupart des cas, développent leurs propres systèmes de génération et de mesure, et sans travaux métrologiques concrets. De plus, les appareils de mesure commerciaux fiables et polyvalents pour ce niveau de puissance ne sont pas disponibles ou sont très rares sur le marché. Les étalonnages de ces systèmes de mesures ne sont généralement effectués qu'à de faibles niveaux d'amplitude par rapport aux systèmes de mesures commerciales existantes, qui ont des bandes passantes inadapté et des tensions d'entrée limitées à quelques kilovolts, et parfois à des fréquences adaptées à l'aide d'analyseurs de réseaux vectoriels mais cela toujours à plus faible niveau de puissance que leurs niveaux de fonctionnement. Par conséquent, la validité de la mesure repose exclusivement sur ces instruments commerciaux et à de faibles niveaux de puissance : la traçabilité n'est alors pas assurée.

L'objectif de la thèse est donc d'assurer la traçabilité au SI des mesures de puissance pulsée nanoseconde et sub-nanoseconde pour accompagner les industriels et les laboratoires de recherche dans ce domaine. Une infrastructure de métrologie doit être développée qui doit être capable d'effectuer des mesures traçables de tous les paramètres des impulsions haute tension rapides, tel que la tension de crête, le temps de montée, la durée d'impulsion et le temps de descente de l'impulsion et cela

pour tous types d'impulsions. Pour atteindre cet objectif, un étalon de mesure doit être développé pour mesurer des impulsions dont les amplitudes de tension maximales sont 500 kV, dont les temps de montée sont compris entre quelques centaines de picosecondes et quelques nanosecondes et dont les durées d'impulsion sont inférieures à 100 nanosecondes. Les incertitude-types visées doivent être inférieures à 5 % pour la tension et inférieures à 1 ns pour les mesures temporelles. En résumé, l'objectif de la thèse est de développer un système de référence qui permettra à terme aux industriels et aux laboratoires de recherche d'étalonner leurs systèmes de génération et de mesure. En effet, la mesure de ces paramètres de la puissance pulsée est réalisée au moyen d'un oscilloscope. Cependant les niveaux de tension acceptables par un oscilloscope impliquent la mise en place d'un diviseur de tension qui s'intercale entre la source impulsionnelle HT et un oscilloscope.

Le travail principal a consisté en la conception, la réalisation et la caractérisation d'un diviseur de tension capacitif calculable (CCVD). Les deux premières étapes du travail sont présentées dans le chapitre 2. Le concept de diviseur choisi est celui basé sur le diviseur capacitif par lignes coaxiales couplées. Un tel diviseur permet en effet de mesurer des pics de tension allant de quelques kilovolts à plusieurs mégavolts dans des bandes de fréquences très larges s'étendant jusqu'à quelques gigahertz. Suivant ce principe, illustré en Fig.1.a), un diviseur de tension a donc été développé en remplaçant un tronçon de la ligne de transmission coaxiale principale en sortie du système de génération d'impulsions, d'impédance caractéristique Z_0, par un tronçon de deux lignes de transmission concentriques, d'impédances caractéristiques Z_1 et Z_2. Un aspect important à prendre en considération est que l'impédance résultant de l'association de ces deux lignes doit être égale à celle de la ligne principale sur laquelle la mesure est effectuée, c'est-à-dire $Z_0 = Z_1 + Z_2$. Le rapport de division d'un tel diviseur ne dépend que des capacités linéiques respectives C_1 et C_2 des lignes Z_1 et Z_2. Le calcul détaillé du rapport de division (DR) de la tension d'entrée sur la tension de sortie est basé sur le modèle géométrique du CCVD illustré sur la Fig.1.b). On peut remarquer que l'électrode intermédiaire, l'électrode1, utilisée pour former la deuxième ligne de transmission concentrique ne couvre pas toute la circonférence de la surface externe du diélectrique (PTFE) et a une largeur limitée seulement à une valeur ***d*** de quelques centimètres. Cette limitation s'explique par la nécessité de satisfaire les conditions de quasi-stationnarité qui sont présentées dans ce chapitre.

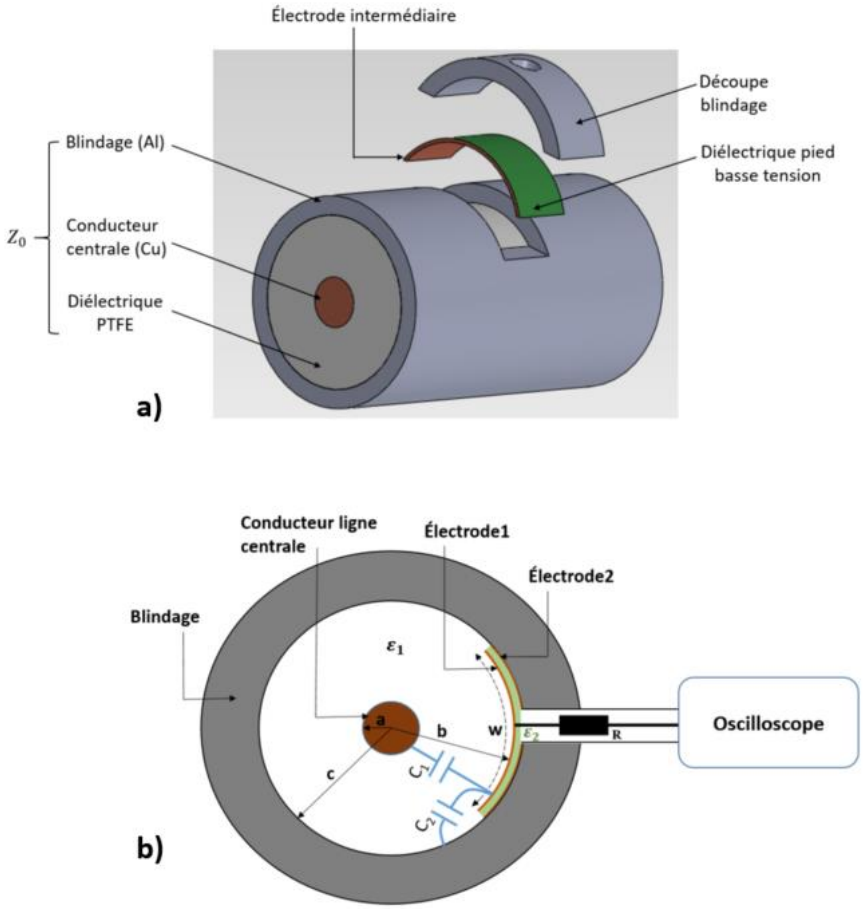

Fig. 1. A) Un exemple de conception de diviseur basée sur le principe des lignes de transmission coaxiale ; b) Modèle géométrique du CCVD (une coupe transversale) : a, b et c sont les différents rayons de la ligne haute tension, de l'électrode insérée et du blindage respectivement ; d est la longueur de l'électrode1 ; $\varepsilon_1$et $\varepsilon_2$sont les permittivités relatives des lignes d'impédances caractéristiques respectives Z_1 et Z_2; et R représente la résistance d'adaptation de 50 Ω à la sortie du diviseur. C_1 and C_2 sont les capacités linéiques des bras hautes tensions et basse tension du CCVD.

Pour les diviseurs de tension basés sur ce principe, la conception du condensateur de bras basse tension C_L formé par la capacité linéique C_2 est la partie la plus critique. Elle détermine non seulement le rapport de division mais aussi sa réponse en fréquence et la stabilité à long terme du CCVD. De plus, sa géométrie doit faciliter le dépôt de la couche diélectrique de SiO_2 (permittivité relative ε_2) pour former le bras basse tension. Afin d'avoir un dépôt de film diélectrique mince et homogène, il est nécessaire que la surface de dépôt de l'électrode1 soit lisse non seulement pour éviter les perforations dans les couches minces déposées mais aussi pour éviter l'accumulation locale de charges qui pourraient créer des champs électriques suffisamment élevées pour provoquer le claquage diélectrique du condensateur. Par conséquent, une géométrie spéciale de l'électrode1 a été conçue pour limiter l'épaisseur du dépôt de couche mince

de diélectrique SiO_2. La conséquence de cette limitation se traduit par un rapport de division maximal égal à environ 17000 :1, ce qui permet l'utilisation du CCVD pour analyser des impulsions haute tension jusqu'à 170 kV directement à travers un oscilloscope. Afin de mesurer les pics de tension jusqu'à 500 kV, un atténuateur commercial calibré supplémentaire de 20 dB, d'une bande passante de 7 GHz sera intégré, à la sortie du CCVD.

La conception du diviseur est détaillée dans son intégralité, depuis l'analyse analytique et la modélisation électromagnétique jusqu'à la fabrication des éléments finaux. Les tests intermédiaires et la validation des performances attendues des principaux éléments de ce diviseur sont également présentés. Les calculs réalisés confirment, comme espéré, que le CCVD possède un rapport de division plat et une réponse de phase linéaires en fonction de la fréquence jusqu'à 2 GHz.

Le chapitre 3 est consacré à la conception et à la réalisation des autres composants du système : une charge coaxiale 50 Ω de terminaison, des connecteurs mâle et femelle haute tension et des cônes de transition d'impédance caractéristique de 50 Ω. En effet, dans un système de mesure destiné à mesurer des impulsions transitoires rapides à haute tension, après un diviseur de tension de précision CCVD, un composant important est le dispositif de charge. Il sert à obtenir une terminaison adaptée à la ligne de transmission avec son impédance caractéristique et à dissiper l'énergie présente dans l'onde incidente. Par conséquent, pour la charge de terminaison à bande ultralarge haute tension, un temps de réponse faible avec une large bande passante de fréquence et des propriétés d'isolation élevées doivent être obtenus en même temps. Ces aspects concernant la charge deviennent plus cruciaux lorsqu'il s'agit d'impulsions haute tension de niveaux d'amplitude jusqu'à 500 kV et dans le domaine de la sub-nanoseconde.

De plus, pour réaliser cette charge coaxiale de terminaison de 50 Ω, le choix de la résistance appropriée constituant le conducteur principal de la charge coaxiale est critique. Parmi plusieurs types de résistances présentes sur le marché, une résistance massive en céramique a été choisi. L'aspect massif confère à la résistance des propriétés peu inductives et permet de répartir uniformément l'énergie et la puissance dans tout le corps en céramique. Ainsi constitué, la résistance résiste à des températures de fonctionnement élevées et permet une dissipation de puissance élevée. Afin d'estimer l'écart de la valeur de la résistance par rapport à sa valeur en continue (DC) lors de

l'application d'impulsions haute tension, une résistance en céramique de la même famille d'une valeur 51,5 Ω (50 Ω±10%) a été testée en lui appliquant différentes impulsions dont les amplitudes varient de 3 kV à 12 kV avec un temps de montée de 1,2 µs et une durée de 50 µs. On a ainsi pu démontrer expérimentalement que les valeurs mesurées de la résistance sont en accord avec la valeur DC dans l'incertitude de mesure absolue de 1 Ω. De la même manière, l'effet de chauffage dans la résistance a été étudié en lui appliquant de façon répétitive (1 000 fois) une impulsion avec un cadencement de 1 s. Cette impulsion a une amplitude de tension de 12 kV avec un temps de montée 1,2 µs et une durée de 50 µs. Les résultats obtenus démontrent que les valeurs mesurées sont toujours en bon accord avec la valeur DC de la résistance, dans la même valeur d'incertitude de mesure que celle mentionnée précédemment.

Une charge de 50 Ω basée sur une structure de diélectrique exponentielle coaxiale avec une résistance cylindrique a été développée dans le cadre de cette thèse avec les performances d'adaptation espérées jusqu'à plusieurs gigahertz. La charge conçue est présentée en Fig.2.a). Les résultats des simulations dans le domaine fréquentiel concerné, jusqu'à 2 GHz, présentés dans la Fig.2.b), montrent que la géométrie modélisée pour la charge terminale de 50 Ω possède un coefficient de réflexion maximale de -30 dB, ce qui est une valeur acceptable et aura des effets presque négligeables sur les impulsions mesurées à la sortie du CCVD. Des analyses TDR (Time Domaine Reflectometry) montrent que la variation de la valeur de l'impédance de la charge est très minime environ 1 Ω. Au final, une charge de la valeur 50 Ω suivant cette géométrie a été conçue.

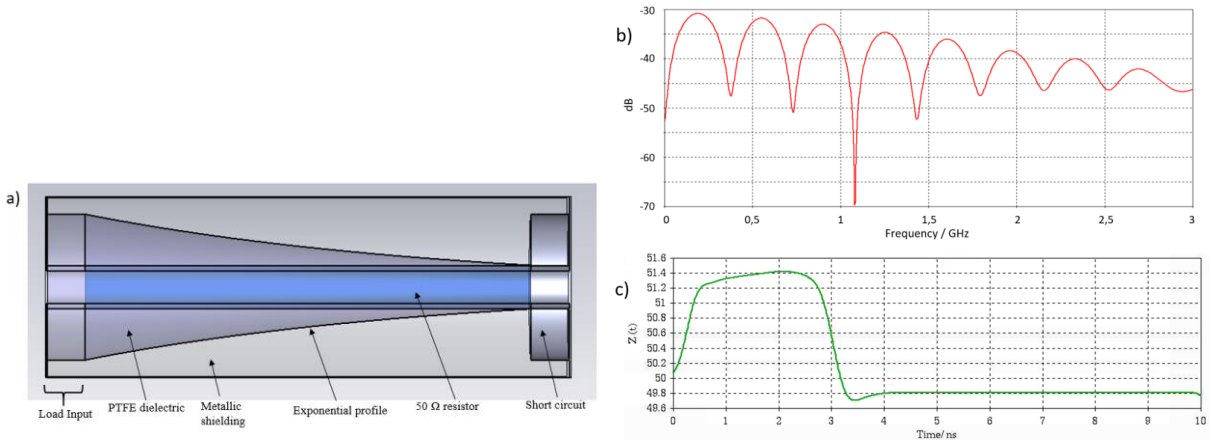

Fig. 2. a) Géométrie de la charge 50 Ω ; b) Coefficient de réflexion de la charge ; c) Analyse TDR de la charge

Les connecteurs haute tension mâle et femelle d'une impédance caractéristique de 50 Ω et les cônes de transition d'impédance ont été également développés dans ce travail de thèse. Ils sont nécessaires pour connecter différents éléments du système de mesure entre eux, tels que la charge au CCVD et même assurer la connexion du système de mesure complet au générateur d'impulsions haute tension pour les mesures. De ce fait, chaque composant du système de mesure a été développé avec ses propres connecteurs haute tension. Ces connecteurs sont capables de fournir une bonne isolation aux amplitudes de tension au moins jusqu'à 500 kV pour les impulsions étudiées.

Tous les composants développés du système de mesure complet doivent être ensuite caractérisés afin d'évaluer leurs réponses en fonction de la fréquence dans la bande passante concernée jusqu'à 2 GHz. Ces caractérisations sont effectuées en termes de paramètres S, à de faibles niveaux de puissance, par le biais d'analyseurs de réseau vectoriel (VNA), qui possède des connecteurs de type N à ses entrées de dimensions différentes des connecteurs mâles et femelles haute tension développés. Pour connecter les composants du système de mesure au VNA, des cônes de transitions d'impédance caractéristique de 50 Ω sont nécessaires, permettant de garder une impédance caractéristique constante tout en assurant une transition entre les dimensions des connecteurs haute tension et les connecteurs Type-N. Ces cônes de transition possèdent des connecteurs haute tension mâles ou femelles à une extrémité et des connecteurs de type N à l'autre extrémité. L'ensemble de ces composants développés complète le système de mesure d'impulsion.

Le chapitre 4 porte sur les caractérisations et la validation du système de mesure développé dans cette thèse. Les procédures expérimentales de caractérisation du système de mesure sont présentées. Dans un premier temps, les caractérisations ont été réalisées pour les différents composants, constituant le système de mesure, à travers un VNA calibré et les résultats obtenus ont été comparés aux résultats de modélisation CST de chaque composant en termes de paramètres S. Ces résultats se sont avérés en bon accord. Ensuite, le système de mesure complet a été caractérisé par deux méthodes différentes, à savoir la caractérisation au VNA puis la caractérisation par une méthode de mesure du facteur d'atténuation, traçable au SI, à haute fréquence (HF). De plus, deux mesures HF1 et HF2, à un intervalle de deux mois par la méthode HF ont été effectuées afin de vérifier la cohérence des résultats de caractérisation

obtenus. L'incertitude de mesure étendue absolue de ces mesures HF est de 0,15 dB pour toutes les fréquences concernées jusqu'à 3 GHz. Comme présenté en Fig.3, les résultats obtenus à partir de toutes ces méthodes expérimentales ont été comparés aux résultats de la modélisation CST et tous ces résultats se sont avérés en bon accord les uns avec les autres.

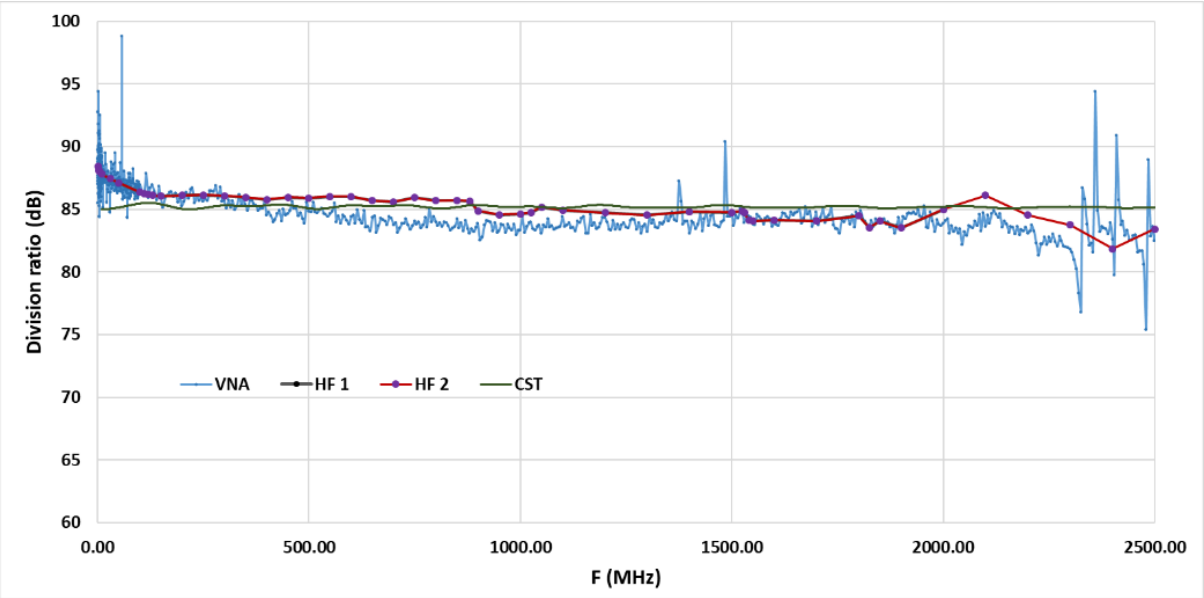

Fig. 3. Comparaison de différents résultats de caractérisation obtenus pour le système de mesure complet

Ces caractérisations ont été réalisées à des niveaux de puissance faibles et ont confirmé la bande passante, le rapport de division et la phase du système développé. De plus, le système de mesure a ensuite été caractérisé en intégrant l'atténuateur supplémentaire de 20 dB et les câbles coaxiaux, indispensables pour permettre les mesures jusqu'à 500 kV. Différentes formes d'onde d'amplitude de tension allant jusqu'à 300 kV et des temps de montée aussi réduits que 420 ps ont été mesurés avec succès grâce à ce système. Un bilan d'incertitude est également présenté.

Toutes les mesures effectuées montrent que l'instrument de référence développé dans le cadre de cette thèse permet de mesurer des impulsions nanosecondes et sub-nanosecondes jusqu'à des niveaux de tension de l'ordre de 300 kV. Les incertitudes-types associées ont été estimées. Elles sont de 3,4 % pour les pics de tension et de 87 ps pour les paramètres temporels. Le Tableau I ci-dessous résume les objectifs et les valeurs atteintes dans cette thèse.

Tableau I Valeurs ciblées et atteintes des différents paramètres d'impulsion dans la thèse

Paramètres d'impulsions	**Valeurs ciblées**		**Valeurs atteintes**	
	Valeurs	**Incertitude (k=2)**	**Valeurs**	**Incertitude (k=2)**
Amplitude (V)	$V \leq 500$ kV	3 % to 5 %	$V \leq 300$ kV	3,4 %
Temps de monté (t_r)	Quelques centaines de picosecondes à quelques nanosecondes	Quelques centaines de picosecondes (incertitude absolue)	420 ps $\leq t_r \leq$ 7,8 ns	87 ps
Durée (t_d)	$t_d \leq 100$ ns	Quelques centaines de picosecondes (incertitude absolue)	530 ps $\leq t_d \leq$ 16,3 ns	87 ps

Contents

LIST OF FIGURES

LIST OF TABLES

GENERAL INTRODUCTION

This PhD dissertation introduces a new standard measurement system, traceable to the International System of units (SI), for accurate and precise measurements of high voltage nanosecond and sub-nanosecond pulses for voltage amplitudes up to 500 kV. These pulses are paramount elements of systems based on High Pulsed Power (HPP).

Since its establishment in 1960s, the HPP range of technologies has found its applications in various domains and has now become one of the rapidly growing areas of research [1]. This is principally due to the fact that these pulses have relatively low energy content though they are capable of delivering very high levels of power. Historically, the first applications were all military, such as, among others, high frequency transmitters, radars, satellites and space probes, pulsed power thrusters, and intense electromagnetic interferences. However, after declassification of many of these works, several civil and medical applications have emerged in recent years. Among them, the most important ones are ground penetration radars (GPR), X-ray machines, cancer treatment, monitoring of human organs, pasteurization of food and vulnerability testing of electronic equipment, proving the strong potential of innovation that lies behind these technologies. For these applications, nanosecond and sub nanosecond pulsed power need to be measured with good levels of uncertainties in order to achieve better control of the voltage impulses used in these applications in terms of amplitude and time parameters, which will provide efficient results and avoid any side effects and unnecessary irradiation of the targeted objects.

In general, the HPP systems consist of three major parts; namely, a HPP generator, a measurement system and a load. This thesis is about the second part of the HPP systems, the measurement system. The measurement system in the HPP domain usually consists of a voltage divider, a low voltage transmission line (habitually a coaxial cable) and an oscilloscope or a digitizer. For the analysis of the waveforms generated by the HPP generators through oscilloscopes or through digitizers, a voltage divider is mandatory which could lower the amplitude of the high voltage pulses generated, usually of tens of kilovolts to several hundreds of kilovolts, to the nominal input voltage levels of the waveform analyzing instruments. In addition, the divider should be capable of measuring accurately, not only the amplitude of the signal but also the precise waveform of the signal, without any deformation or loss of information. For this, it is necessary to know the division ratio with a good uncertainty level and the

bandwidth of the divider should be compatible with the frequencies of the spectrum of the pulse signal.

The voltage dividers in the HPP technologies are most often developed by the laboratories working in these domains themselves because commercial devices for this level of power cannot be found or very rare in the market. More importantly, another issue lies behind the fact that the calibrations of these dividers are generally carried out at low levels of amplitude by comparison with existing commercial probes, which are themselves limited in terms of voltage peaks, generally up to 10 kV, and also in terms of bandwidths. Indeed, until today, for the fast rising voltage peaks in the HPP domain, there is still no measurement standard and the National Metrology Institutes (NMIs) still do not issue calibrations of such dividers. Therefore, the validity of the measurement is based exclusively on the voltage limits of these commercial probes; and for higher amplitude levels, the traceability is absent. Thankfully, very recently, a NMI has proposed the traceability of these fast high voltage pulses, but this traceability is limited to only voltage amplitudes up to 100 kV and that too for the pulse rise times of only up to few nanoseconds [2]. However, for even faster pulses and for higher voltage amplitudes the traceability remains completely absent.

It is in this context that this thesis takes place. The work presented in this dissertation concerns the study, the conception and the characterization of a complete, SI traceable, calculable measurement standard system capable of measuring accurately and precisely, i.e. with good levels of uncertainties, the high pulsed power in the nanosecond and sub-nanosecond domain (HPPNS) of pulses of voltage amplitudes up to 500 kV. The developed measurement system consist principally of three main components, namely, a voltage divider, a transmission line termination load and high voltage connectors that were specially developed in this thesis as the connectors capable of withstanding these high levels of voltage peaks are not available in the market.

This manuscript is organized as follows:

In the first chapter, an overview of the sector of the high pulsed power in the nanosecond and subnanosecond domain (HPPNS) is presented. To place the reader in the context and to demonstrate the importance of this study, this chapter starts with some concise details about some important applications of the HPPNS in the domains such as military, civil and medical. The next part of this chapter describes the technologies and methods used to generate and to measure HPPNS, which are important aspects for the comprehension of the HPPNS domain. Furthermore, SI traceability coverage and limits

are also presented for the HPPNS, which explains to the reader the need of this study. Finally, the detailed objectives that we fixed to attain in this thesis work are discussed.

The chapter two describes the study and the conception of the central element of the measurement system of the HPPNS, that is a voltage divider based on the principle of the transmission line. A though analysis of the most critical part of this divider which is the low voltage arm is presented. This element determines not only the division ratio of the divider but also its frequency response. These two criteria determine the efficiency of the divider to measure very fast high voltage pulses in a precise and accurate manner. The electromagnetic modellings are also presented which are intensively used to optimize the response of the divider. The last part of this chapter demonstrates the mechanical realization and some important preliminary testing of this divider.

The third chapter is all about the 50 Ω transmission line termination load and the high voltage connectors developed in this thesis work. The 50 Ω load is another essential element of the HPPNS measurement system which is destined to perform two critical roles. The first one is the matched termination for the transmission line with its characteristic impedance and the second one consists of the dissipation of the energy present in the incident high voltage pulse. Consequently, for the high voltage ultrawideband pulse termination load, a fast response time with a wide frequency bandwidth and high insulation properties are achieved at the same time. The high bandwidth of this load is obtained with a special load geometry, which is studied thoroughly and presented together with an electromagnetic modelling and the mechanical conception. In addition, the connectors capable of withstanding voltage peaks as high as 500 kV are unavailable in the market. The connectors developed are of 50 Ω characteristic impedance, as the main transmission line characteristic impedance, and are capable to provide good insulation to the voltage amplitudes at least up to 500 kV for nanosecond and sub-nanosecond pulses.

The chapter four is dedicated to the characterization of the developed HPPNS measurement system. The characterizations are performed in terms of scattering (S) parameters. These characterizations have been carried out in two phases. Firstly, each component such as the voltage divider, the 50 Ω termination load and the connectors are characterized in order to evaluate their footprints on the whole measurement system. Secondly, the complete measurement system is characterized for its attenuation in the concerned frequency bandwidth. This last step is carried out using two different measurement setups for the consistency of the obtained results, namely, a calibrated Vector Network Analyzer (VNA) and then an SI traceable high frequency attenuation measurement setup. An explanation of both of these characterization methods are

presented in this chapter. The results obtained through these characterizations are compared with the electromagnetic modelling and, as awaited, all the results found to be in very good agreement with each other. Finally, the HPPNS measurement system was successfully employed to measure high voltage pulses of amplitudes ranging from 100 kV to 300 kV with rise times as fast as 420 picoseconds.

In the end, which marks the beginning of the SI traceability of the HPPNS, the manuscript reminds the objectives, the results obtained and the main contributions of this thesis. Perspectives opened by this work are mentioned in this last part.

.

CHAPTER

1

This very first chapter of this thesis gives an overview of the domain of the pulsed power technology. The evolution of this domain from a classified military technology to a technology essential in our daily lives can easily be observed. Some of the aspects such as applications, generation and measurement techniques of these high voltage rapid pulses has been described. Finally, the problems related to the accurate and precise measurements of these pulses and the lack of metrological traceability at these voltage levels has been discussed ending with the objectives of this thesis work.

Chapter 1: High Pulsed Power at nanosecond and sub-nanosecond level (HPPNS): An introduction

The term High Pulsed Power (HPP) refers to the technologies where energy is accumulated during a relatively long period of time and then released in a short period, in a form of pulse, to deliver a very large amount of power to a given load, or in other words to a given application. Generally, the HPP systems are composed of a primary source of energy and a load, separated by a HPP generator, which transfers the energy from the source to the load. The phenomena such as, the storage and the release of energy take place in this generator, which is, in principle, a power amplification and pulse forming system that is charged by a DC or a pulsed source of energy. The generated pulse is nothing else than the kinetic energy of an electron beam that is coupled to a microwave signal for pulse durations of tens to hundreds of nanoseconds. This microwave energy, in most of the applications, is then projected towards the target through a waveguide and an antenna.

Basically, this technology amplifies the input power by compressing the time, to extremely higher values of the output pulsed power, while keeping constant the energy

content between the input and the output, before it could be delivered to the target load. For example, as presented in the Fig.1, a power of 100 Watts during 100 milliseconds could be converted to a power of 1 gigawatt for 10 nanoseconds of duration. This is equivalent to the power output of a nuclear power plant, although for this duration the energy provided is only of 10 Joules.

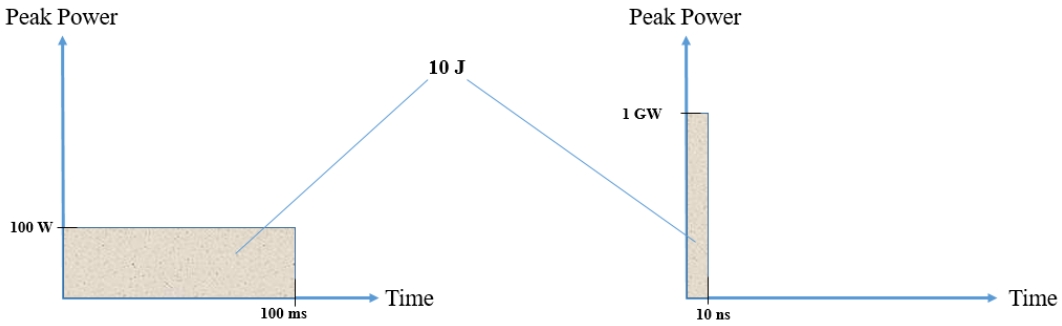

Fig. 1 Principal of generation of Pulsed Power

Historically, typical loads were primarily defense related applications such as among others, charged particle beam diodes and imploding plasmas [3]. When the load is an antenna, it is possible to generate electromagnetic waves in form of pulses and the frequency band of the wave thus radiated can cover a very broad spectrum. However, thanks to the declassification of this technology, different medical and civil applications have emerged in the past few decades. The evolution of the domain of pulsed power has been essentially dictated by some key applications that require a very large amount of power in a very short time period. Another benefit of the systems based on this technology is that they are, most of the time, compact and portable. They can be easily installed and transported without deploying a considerable amount of effort.

The high pulsed power in the domain of nanosecond and sub-nanosecond (HPPNS) technologies usually deal with systems capable of producing high voltage pulses that could attain voltage peaks of few hundreds of kilovolts and of durations ranging from 10^{-11} to 10^{-7} seconds. The devices operating on this time scale can deliver output pulse powers from tens of megawatts to hundreds of terawatts and have found their applications from national level facilities to objects of our daily life. Among them, the most important ones are inertial nuclear fusion, production of super power laser, neutron pulses, X-ray machines, particle accelerators, ionizing radiation, medical imaging, radiotherapy, cancer treatment, ground-penetrating radars (GPR), air purification, pasteurization of food, water and waste treatment, treatment of gas

pollutants and treatment of incarnation ashes. Some of these applications are detailed in the following sub-sections.

1.1. Applications

1.1.1. Underground and on-surface sensing: ground penetrating radars (GPR)

Since more than half a century the detection of buried targets has been a problem of great interest in many applications such as, detection and identification of buried conduits, minerals, chemicals, archaeological sites and landmines [4]. Every year thousands of people lose their lives or are mutilated due to undetected sub-surface landmines. Moreover, it becomes difficult to locate and identify debris present inside most soils due to their high attenuation factor. The microwave based underground sensing systems have been successfully developed and used for the detection of such kind of targets. These systems work on the principle of radars and are most of the time constituted of a pulse generator linked to antennas for transmission and reception of waveforms. The system detects targets through the reflection of an electromagnetic wave. This wave illuminates the intended target, which in return reflects a part of the incident wave back to a receiving antenna. The return of the reflected wave justifies the presence of the target. The time taken by the signal carried by the wave to travel from the transmitting antenna to the target and to return to the receiving antenna indicates the distance at which the target is located. The characteristics of the reflected signal make it possible to specify the direction, nature and shape of the object. A significant tool based on such principle is ground penetrating radar (GPR). These systems operate on frequencies ranging from few hundreds of megahertz to few gigahertz to achieve a good ground penetration as well as a rich in information spatial resolution for objet discrimination. GPR systems have the advantage that, due to their relatively small size, they could be easily transported by some airborne structures for larger area scanning of buried structures and at the same time could be used near the surface without deploying huge logistics. The imaging technique is, most of the time, based on the same technique as a synthetic aperture radar (SAR) [5]. The principle consists in synthesizing an antenna that is more directive than a classic antenna. This is done by moving the radiating

element laterally which gives an impression of an antenna array, this is called aperture synthesis. The processing, by integration, of the signals received makes it possible to reconstitute an electromagnetic image of the scene.

The detection procedure of a conducting cylinder of 60 cm of diameter, 90 cm of length buried under 30.48 cm from the ground surface by a GPR is very well demonstrated in the paper published by S. Vitebskiy [6] in the year 1997. His system measures VV (vertical transmit, vertical receive) and HH (horizontal transmit, horizontal receive) polarizations and operates in the time domain with an instantaneous bandwidth of approximately 0.1 to 1.5 GHz, and with an approximate peak radiated power of 150 kW. The procedure is illustrated in the Fig.2.

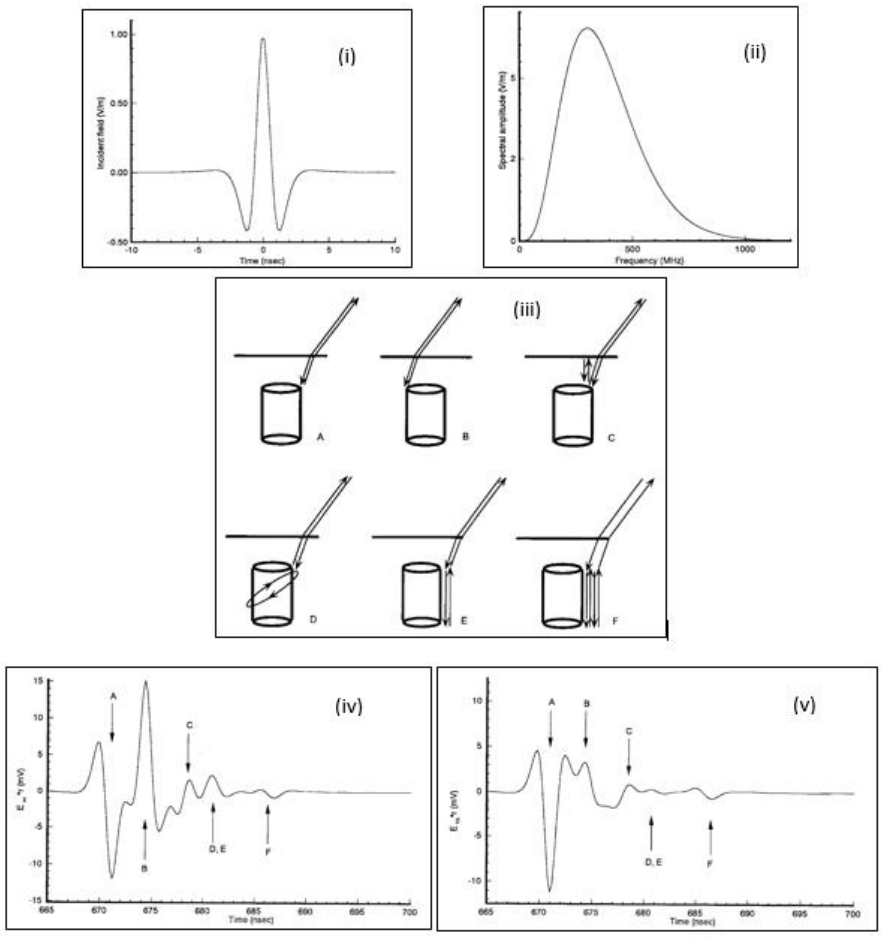

Fig. 2. Detection procedure of a GPR [6]. (i) emitted time domain pulse, (ii) frequency domain spectrum of the emitted pulse, (iii) scattering phenomenology of the wave fronts from a buried cylinder, (iv) VV time domain backscattering fields, (v) HH time domain backscattered fields

1.1.2. Electromagnetic jamming

Communication devices based on radio frequency have become an inseparable part of our daily life. The radio frequencies have the ability to propagate in all directions and one of the consequences of this "wild spread" of radiofrequency waves is the ease with which a malicious person can jam a network, even being outside the space where the wireless network is supposed to be deployed. The attack by jamming signals consists in intentionally emitting a signal, which covers the frequency bands employed by a communication system in order to disturb the reception of a communication device. Generally, the power levels of jamming signals are similar to that of communication signal power levels. Thus, the jamming signals can degrade the performance of the communication networks without really damaging the communication devices. The consequences associated with possible interference are various. But in some areas, jamming can make ineffective many functions, sometimes even the functions that are related to the security of the system itself. On the other hand, jamming could be advantageous in some sectors such as in the sector of defense. It could be used to protect people, military convoys, public personalities etc. Furthermore, the ill-intentioned groups are more diverse and, consequently, the areas of conflict have grown. As a result, technical means are increasingly mobile and more innovative. The threat is no longer clearly located, it can strike anywhere and anytime. The use of IEDs (Improvised Explosive Devices) is a problem against which the regular armed forces must fight assiduously in all current conflicts. Easily manufactured at low cost and controlled remotely, they are easily available and easy to use for ill-intentioned individuals and groups. Protective interference is now mandatory on high-risk sites. These devices also cause many victims among the civilian population. This is why military convoys tend to be equipped with jamming systems capable of destroying these weapons. These systems consist of a source of pulsed electrical energy and a suitable antenna capable of emitting electromagnetic radiations rending non-functional the radiofrequency devices such as remote controls, mobile phones etc.

1.1.3. Biomedical domain

Jean-Antoine Nollet documented the first ever effects of the electric sparks on humans in his book published in the year 1749 [7]. He observed the formation of red spots when electric fields were applied to human skin, which is most probably caused by the phenomenon of irreversible electroporation (IRE). During a long time, it has been a common belief that the cell destruction was principally due to the temperature rise around the targeted cells; however, in the year 1967, it was proven by Sale et al. that the cell death was essentially related to the electric field parameters [8]. Since then, a lot of progress has been achieved in terms of living cell exposure to high voltage electrical pulses. Furthermore, taking into account the electrical properties of human tissues, high voltage electrical pulses are also used to remotely monitor internal organs of human body without damaging human tissues. The details of these phenomena can be found in the following sub sections.

1.1.3.1. Cancer treatment - Oncology:

There has been a considerable amount of studies on the effects of the application of high voltage pulses on living cells. A detailed review of the effects of high voltage pulses in the domain of oncology has been presented by Geboers et al. [9], the following section has been inspired by their findings. The application of high voltage pulses triggers a number of processes that occur at cellular levels. One of the most important one is electroporation. Electroporation is permeabilization of the cell membrane by the application of high voltage pulses. This phenomenon is very advantageous from the point of view of cancer treatment. In the year 1987, Okino et al. [10], was able to successfully introduce a considerable amount of bleomycin, a cancer treatment drug, into the cell membrane by electroporation. He observed a decrease in tumor cell size of around 17 % of the initial mass just four days after the treatment. This lead to the birth of electrochemotherapy (ECT). Later, electroporation was successfully employed to transport other non-permanent molecules such as DNA, dyes and proteins into the cell membrane. There are two kinds of electroporations; it could be either reversible or irreversible. Reversible electroporation occurs when the membrane permeability increases transiently and the cell regains its stability. It is mainly used in the ECT, gene electrotransfer (GET), and electrofusion. On the other hand, irreversible electroporation

occurs when the magnitude and duration of the applied pulses surpass the adaptive capacity of the cells and result in cell death.

The application of high voltage pulses rends permeable tumor cells, which in return facilitates the ion transfer into the cells. The electric fields primarily interact with the cell membrane and modify its resting potential. In addition, when the transmembrane potential exceeds a critical value, the membrane becomes unstable resulting in the formation of small pores. The pore formation is essentially initiated by the penetration of water molecules into the lipid bilayer, leading to the reorientation of the adjacent lipids, with their polar head groups pointing towards these water molecules. This process is presented in the Fig.3, where four needle electrodes are inserted around the tumor (brown) within healthy tissue (beige), phase A is just before the application of high voltage pulse; phase B represents the cell behavior during the application of pulses, cell permeabilization and the passage of chemotherapy particles can be observed; and phase C represents the closing of pores and cell death after the penetration of chemotherapy particles.

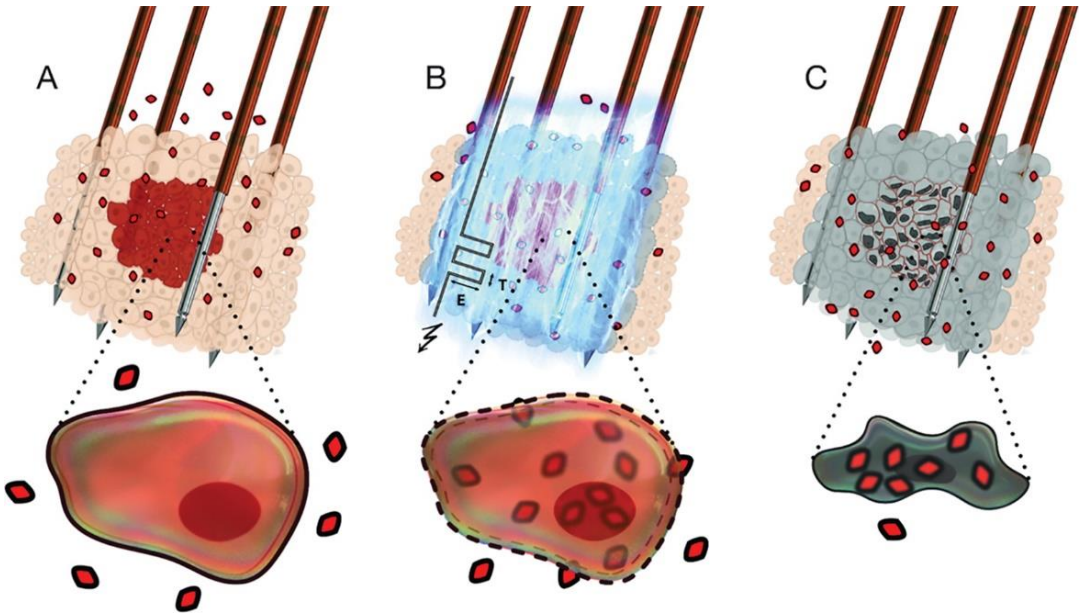

Fig. 3. Electrochemotherapy (ECT), bottom line shows a zoom of phenomena occurring at cellular level of the tumor cells [9].

An effect of the exposure of a cell to a pulsed electric field can also lead to the electroporation of the inner organelle[1] membranes. However, the voltages induced to inner organelle membranes by these electric fields are several folds smaller than the voltages induced on the plasma membrane, causing the electroporation of the latter only. Furthermore, it has been reported by Kotnik and Miklavcic [11] that the induced voltage by an external pulsed electric field on an organelle membrane cannot exceed to that of cell plasma membrane, given that the electrical properties of the organelle interior is very similar to those of cytosol, and both the membranes are similar in nature. Moreover, in the case of mitochondria, which possesses a membrane thicker than that of the cell, the voltage induced can be higher but the electric field will remain less than the electric field in the cell membrane, leading to the electroporation of the cell membrane but not that of the organelles.

1.1.3.2. Monitoring human organs and tissues

High voltage fast pulses have gained a considerable amount of interest in the past few decades and many researches in terms of monitoring human organs and tissues based on these pulses have emerged. Most of these researches are based on ultra-wideband (UWB) technology. The UWB is a wireless communication technology that introduces a wide approach of wireless communication techniques in various domains. It works in the frequency range of 3.1 GHz to 10.6 GHz and the power spectrum density (PSD) of -41.3 dBm/MHz as recommended by the American Federal Communication Commission (FCC) [12], as shown in the Fig.4 [13], and the International Commission on Non-Ionizing Radiation Protection (ICNIRP) [14]. Studies have shown that this technology can be very efficiently used in the medical domain without having side effects on the target and with a good penetration ability to human tissues. Based on the differences in the dielectric properties of human tissues, this technology can be employed to detect, for example, breast cancer, or for the organ movement detection like heart rate and respiratory detection.

[1] An organelle is a subcellular structure that has one or more specific jobs to perform in the cell, much like an organ does in the body. Among the more important cell organelles are the nuclei, which store genetic information; mitochondria, which produce chemical energy; and ribosomes, which assemble proteins.

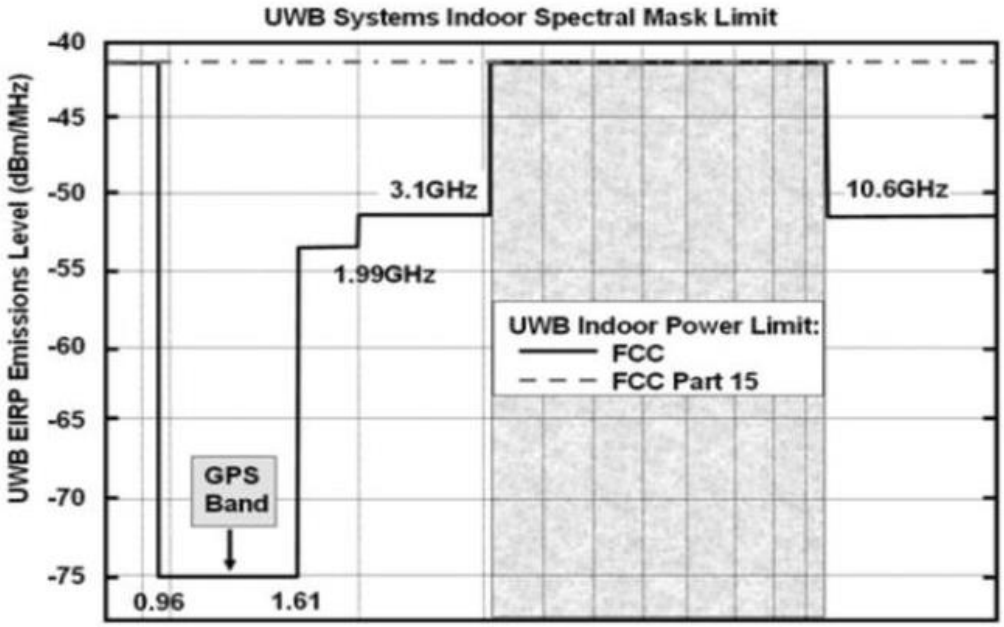

Fig. 4 Indoor power spectrum mask from FCC [12]

The most interesting part of the UWB technology is the possibility to monitor the motion of internal organs of the human body with a remote non-contact approach. Another non-negligible advantage of these systems is the low energy content of the electric field emitted with a considerable amount of power; rending this technology possible for applications such as cardiac biomechanics assessment, chest movement assessment, Obstructive Sleep Apnoea (OSA), soft-tissue biomechanics research, Sudden Infant Death Syndrome (SIDS) monitors, vocal tract studying, non-invasive biochemical study of soft tissues such as brain and infrared spectral imaging [15].

1.2. Generation

It is well established that the pulsed power technology is relatively cheaper and more simple than other architectures aiming to produce high current, high voltage or ion accelerators [16]. The fundamental purpose of all pulsed power systems is to convert low power slow input into high power fast output, keeping constant the energy content of the input and the output. In many application areas of the high power electromagnetic pulses, the requirement of the output power levels of test facilities in laboratory or in industry have been continuously increasing and the technologies capable of supplying these levels of power have been continuously adapted to meet the needs.

There are two main types of principles that are employed to generate these levels of pulsed powers, namely, Marx generators and pulse transformers. The main difference between these two principles is the means of energy storage. In the case of pulse transformers, the energy is accumulated in the magnetic field of a current carrying inductive circuit and then released to the load through circuit breakers, while in the case of Marx generators an electrical field energy is stored in fast capacitive energy banks, such as low-inductance capacitors and liquid dielectric pulse forming lines, and transferred to the using nanosecond high-current closing switches. Each type of generator has its own relative advantages and drawbacks. Many factors are taken into account and depending upon the characteristics of the output pulse required, the choice is made for the generation principle. Both of these principles are described in the following section.

1.2.1 Marx Generator

Marx generator is a device capable of generating megavolts levels of output pulses from only few tens of kilovolts of input. It was first described by Erwin Otto Marx in 1924. This generator finds most of its applications when a large amount of energy is required under a high voltage in a short time, generally in a single pulse regime. However, today, the Marx generator is beginning to establish itself more and more in applications where repetitive pulses are required [16]–[32]. It is probably one of the simplest and most economical solutions for producing high voltage pulses.

In fast pulse technology, capacitive Marx generators operating with spark gaps are in most common use. Marx generators consists of multiple storage banks, usually capacitors. These storage banks are charged in parallel, to a voltage V_0, through charging resistors or in some cases inductors, can be used for better charging efficiency and repetition rate of the generated pulse. Once the capacitors are charged, switches are activated in an avalanche mode such that they connect all the stages in series and the output voltage pulse is generated. The theoretical output voltage of the pulse reaches an amplitude equal to $n \times V_0$, where n is the number of stages. The working principle of the n stage Marx generator is presented in the Fig.5. Each stage consists of a capacitor or a combination of capacitors of an equivalent capacitance ***C***, a charging resistor ***Rc***, and a switch ***Sw*** which is usually spark-gaps. In some applications, the resistors ***Rc*** are replaced by inductances to reduce energy losses and save battery autonomy for repetitive operations.

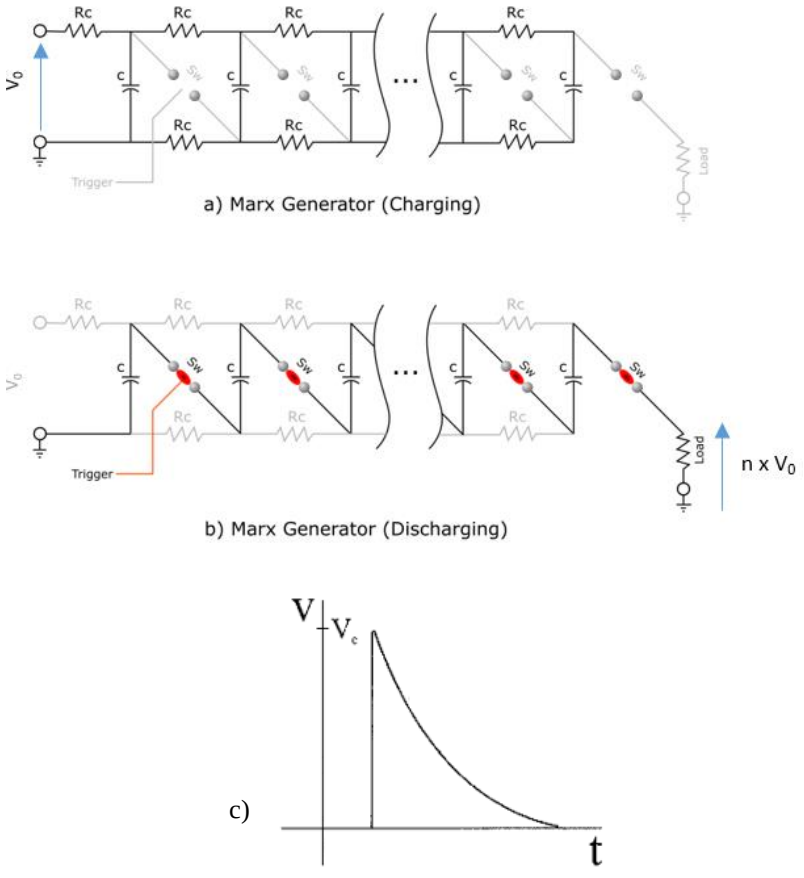

Fig. 5. Marx generator circuit of n stages; a) Charging phase of the Marx generator; b) Discharging phase of the Marx generator; c) Typical waveform generated by a Marx generator

In principle, there is no limitation in the number of stages to be switched, therefore there is no limitation in the amplitude of the output voltage. Generally, the Marx generators are used in the production, at very low recurrence rates, of very high voltage pulses of relatively long duration for applications requiring the implementation of significant amount of energies (Z-machine, accelerators). However, more compact and less energetic versions can be easily developed for applications at higher repetition rates, of hundreds of Hertz. The Marx generators are designed so that the switching of each stage produces a transient state capable of switching of the stages that follow. In general, the complete switching of these generators is done in a time between a few nanoseconds and a few microseconds. They can deliver their energy during a time depending on the value of their capacitance i.e. the energy stored per stage, the total parasitic inductance of the generator and the damping resistors. This duration can vary from a hundred nanoseconds to a few milliseconds and the amplitude of the voltage decreases exponentially during this phase, defining the duration of the pulse thus generated.

The output voltage pulse of a typical Marx generator resembles a standard RC decay. However, for low impedance loads where the parasitic inductance of the Marx generator and that of the load would produce a wave shape of a typical RLC circuit. Furthermore, to obtain a desired pulse shape, a supplementary pulse conditioning system connected to the Marx output is required. For example, a Pulse Forming Line (PFL), which is a combination of supplementary peaking switches [33], [34], is required to obtain square, Gaussian or bipolar pulses at the output of the Marx generator. The size of the PFL could represent some disadvantages when the size of the total pulsed power system is a primary concern for some applications. On the other hand, Marx generators based on Pulse Forming Network (PFN) could come handy where the total size of the pulsed power system is a critical issue. A PFN is made from a number of discrete inductors and capacitors, which are integrated in each stage of the Marx generator and could be optimized easily to produce the required voltage pulse shape. This type of generator produces a rectangular output pulse, with the duration of the pulse dependent upon the values and number of L and C components in the pulse-forming network and the number of repeated stages. This system combines the high output power capabilities of a Marx generator with the compact pulse conditioning properties of a PFN [19], [27], [35], [36]. When ignited, the voltage of each stage is added in the desired pulse shape at the Marx output. Moreover, the pulse repetition frequency (PRF) is another requirement parameter, which changes considerably the designing procedure of the Marx generator.

Most Marx generators are built with fix spark gaps, and the operating range is determined by changing the pressure and/or the nature of the insulating gas present in chamber. They can even be connected in parallel to obtain even smaller rise times by reducing the total inductance of the system, given that the erection of each Marx generator must be reproducible and reliable. Reproducibility can be obtained by minimizing the erection time which could be achieved by triggering each gap or coupling the untriggered gaps to earlier gaps [20]. The output pulse voltages of the Marx generators working in oil can reach up to multimillion volts. However, Marx generators capable of generating one million volts could be very well designed in air by taking special care to avoid flashovers.

1.2.2. Pulse transformers

A transformer that couples a source of pulses of electrical energy to a load is a pulse transformer. First pulse transformers dates back to the early years of Second World War, where they were used to generate quasi-rectangular voltage pulses to supply power to the microwave magnetrons for radar systems and due to the observed effects of varying current upon the output frequency of the magnetron, the engineers then named them as pulsers. One of the early airborne systems supplied 1 μs pulses of 12 kV at 12 A at a frequency of 1 kHz [37]. Pulse transformers are pulsed power supplies that generate bursts of high frequency current at very high voltages. They are relatively simple, compact, and cheap which facilitates their use in wide range of applications from particle acceleration to insulation testing [38]. A simplest form of a pulse transformer is an automobile ignition coil. Pulse transformers are also widely used in the applications such as radars systems, klystron and magnetron modulators, which require a nearly rectangular pulse in addition with specific pulse rise time and overshoot.

Pulse transformers are principally used in many special circuits and applications where the pulse shape, and not the maximum transfer of energy, is the primary consideration [38]–[50]. Often, for example, certain limits are placed upon the rate of rise, the percentage of droop throughout the pulse, and the shape and magnitude of the backswing voltage. In most of the applications in which the pulse transformer supplies the main pulse power to a microwave electron tube, a negative polarity pulse is applied to the tube's hot cathode.

The Fig.6.a. shows the equivalent circuit of a pulse transformer as standardized by IEEE [51]. According to this standard, for a given transformer, the values of many circuit elements are the same for pulse and wideband applications and these elements are essentially independent of the core excitation. They include the transformer ratio $\boldsymbol{n}$, $\boldsymbol{R_{cu1}}$ and $\boldsymbol{R_{cu2}}$ primary and secondary winding resistances, primary and secondary leakage inductances $\boldsymbol{L\sigma_1}$ and $\boldsymbol{L\sigma_2}$, and transformer capacitances such as the distributed capacitances $\boldsymbol{C_1}$ and $\boldsymbol{C_2}$, and interwinding capacitance $\boldsymbol{C_{12}}$. However, some of the equivalent circuit elements associated with the nonlinear magnetic core, such as the magnetizing inductance $\boldsymbol{L_{mag}}$ and the core-loss resistance $\boldsymbol{R_{Fe}}$, are highly dependent on the type of excitation. This circuit can be reduced to the Fig.6.b in order to simplify the analysis of the transient behaviour for operation with rectangular pulse voltages during the rising phase of the pulse if n >> 1 [37].

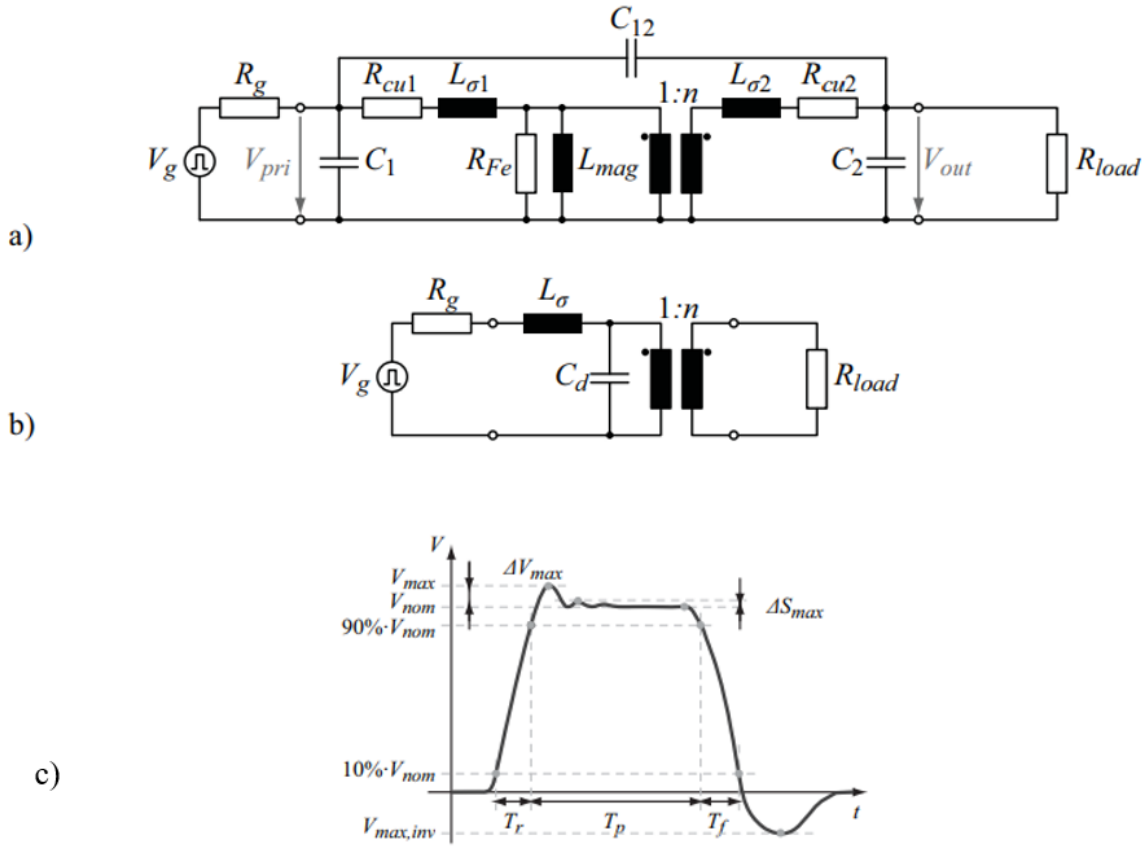

Fig. 6. a) Equivalent circuit of a pulse transformer as standardized by the IEEE; b) simplified equivalent circuit during the rising of the pulse [52]; c) Typical waveform generated by a power modulator

1.3. Measurement techniques

HPPNS systems need high voltage, steep rise time and short duration of pulses, and require accurate and precise measurements for all these parameters. These systems are sometimes located at remote or inaccessible sites, or even in outer space, and at times release a large amount of explosive energy during the operation. For accurate measurements, the measurement system must present a negligible load on the pulsed power supply so as not to distort the pulse waveform or draw significant amount of power from the supply. Furthermore, the characteristics of the measurement system, relative to the nature of the pulse being measured, are extremely decisive for the accuracy of measurement of pulse properties. Especially in terms of the response time of the system. For example, a measuring system having a rise time of 5 nanoseconds is incapable of accurately measuring the peak voltage of a pulse whose duration is 1 nanoseconds. On the other hand, measurement of a pulse with 20 nanosecond duration would be within the capability of a 10 nanosecond system, provided the pulse is approximately rectangular in shape. Furthermore, the phase characteristics of the measuring system should be such that the time of transmission of all significant frequency components in the pulse is constant (i.e., linear phase shift) [53]. Furthermore, other precautions are necessary in pulse measurements such as adequate shielding of measuring equipment, cable length which may introduce resonance effects, proper terminations, and nonlinear behavior of circuit elements.

Today, modern applications require coaxial connections for interference free signal transmission through coaxial cables to the measurement instrument, such as a calibrated oscilloscope. An oscilloscope is one of the best candidate to not only to measure the electrical parameters of the pulses but also the temporal ones. However, the nominal input voltages of most of the oscilloscopes are limited to very low voltage levels. Wherefore, using an oscilloscope to analyze the time and voltage evolution of signals of several hundred of kilovolts requires the use of voltage dividers and that too with a significant value of the division ratio. A schematic of the HPPNS measurement system is presented in the Fig.7.

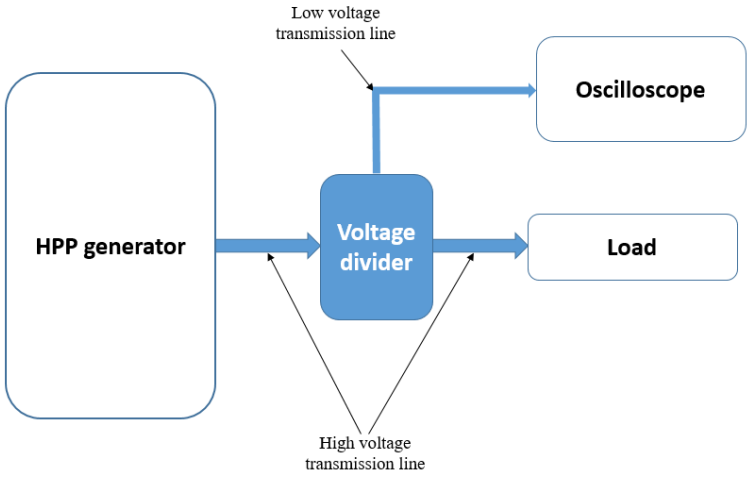

Fig. 7. Block diagram of HPPNS measurement system

Voltage dividers are the most important instrument in high voltage measurements systems, as the magnitude of the peak voltages in HPPNS systems could vary from tens of kilovolts to thousands of kilovolts in the frequency range from hundreds of megahertz up to few gigahertz. Consequently, the voltage divider used in the measurement system should possess an extremely high division ratio and a wide bandwidth simultaneously. For example, a HPP system based on high voltage pulses of voltage peaks of 500 kV with rise times (t_r) of 0.5 nanoseconds requires a voltage divider of a division ratio of around 10^5:1 with a high cut off frequency (f_c) of 0.7 GHz given by the equation 1 [54]

$$f_c = \frac{0.35}{t_r} \tag{1}$$

The value in the numerator depends on the pulse shape and varies from 0.4 to 0.34 (~0.34 for a Gaussian pulse). Therefore, to minimize distortions of the pulse shape, the bandwidth of the measuring circuit and equipment should be higher than the frequency f_c [55]. In addition, the integration of the voltage divider in the HPP system should be non-invasive to the signal being measured.

In general, there are four types of dividers that could be used to measure high voltage pulses, namely, resistive voltage divider, capacitive voltage divider, D-dot sensors and capacitive voltage divider based on the transmission line principle. These dividers are presented in the following sections.

1.3.1. Resistive voltage divider

To measure high voltage pulses resistive voltage dividers could be used to attenuate the high voltage signal to an adequate low level signal that could be measured through an oscilloscope. These are simplest form of voltage dividers based on discrete resistors or resistive elements [56]–[63]. A schematic of the principle is shown in the Fig.8, where ***V1*** is the high voltage peak generated by the high voltage pulse generator, ***R1*** is the high voltage arm resistor of the divider and ***R2*** is the low voltage arm resistor of the divider where the divided low voltage pulse ***V2*** is measured.

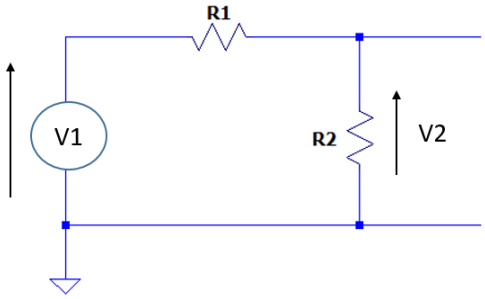

Fig. 8. Schematic of a resistive voltage divider

Taking into account the high input impedance of the oscilloscope with respect to the low voltage arm resistor ***R2***, the division ratio ***DR*** of the divider is given by the equation (2):

$$DR = \frac{V_1}{V_2} = \frac{R_1 + R_2}{R_2} \tag{2}$$

In this kind of dividers, the values of the resistors are generally chosen to be high so that the insertion of the measurement probe causes negligible effects in the circuit where the measurement is to be carried out and to avoid too much current consumption in the measurement circuit. However, the skin effect in the resistive elements, the parasitic capacitances and the self-inductance of the conventional wire wound resistors causes undesirable resonance and ringing, which eventually deforms the edges of the measured pulse [64]. The use of these dividers is therefore limited to the measurement of signals in a band extending only up to a few tens of megahertz and possibly presenting a DC component too. It is therefore not suitable for measuring signals with fast edges whose frequency spectrum extends up to several hundred megahertz or even a few gigahertz, which is the concerned frequency range for HPPNS systems.

1.3.2. Capacitive voltage divider

Capacitive voltage dividers are generally used to measure fast signals [54], [64]–[71]. This divider provide high division ratios and fast response time for measurements of high voltage rapid pulses. The principle of the capacitive voltage divider is presented in the Fig.9, where ***V1*** is the high voltage peak generated by the high voltage pulse generator, ***C1*** is the high voltage arm capacitor of the divider and ***C2*** is the low voltage arm capacitor of the divider where the divided low voltage pulse ***V2*** is measured through the oscilloscope represented by its input impedance ***R0*** and ***C_oscillo***. A 50 Ω matching resistor ***R1*** is used between the low voltage arm of the divider and the oscilloscope to avoid the creation of standing waves.

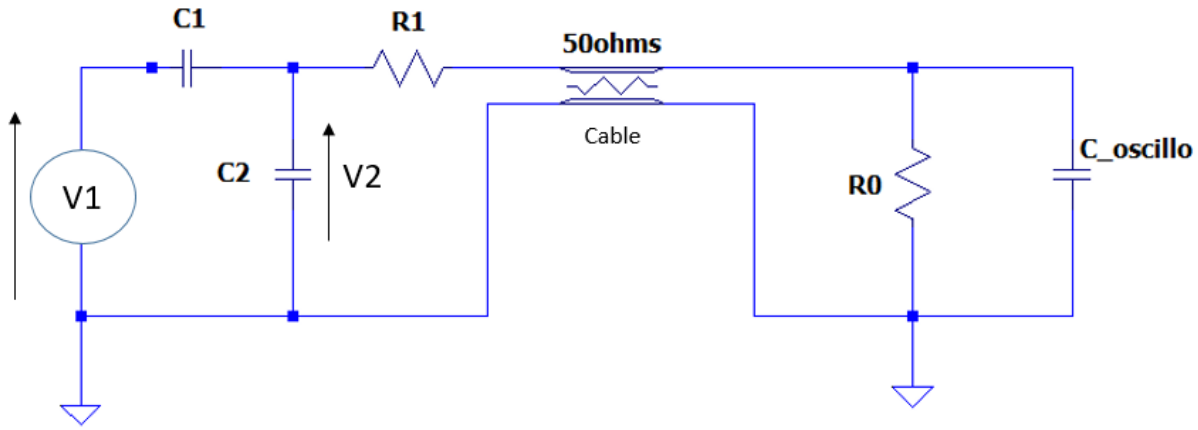

Fig. 9. Schematic of a capacitive voltage divider

For the sake of a substantial division ratio, to measure high pulse peak voltages, the value of the capacitor of the low voltage arms ***C2*** must be chosen to be high as compared to the high voltage arm capacitor ***C1***. The internal capacitance of the oscilloscope ***C_oscillo***, which is in the range of few pF, can be therefore considered negligible in front of the capacitance ***C2*** and the division ratio ***DR*** of the divider can be expressed by the equation (3).

$$DR = \frac{V_1}{V_2} = \frac{C_1 + C_2 + \dfrac{1}{j(R_0 + R_1)\omega}}{C_1} \tag{3}$$

For high frequencies, if we neglect the parasitic elements, such as connection inductances, capacitances between metallic conductors and surroundings, and cable

lengths, the bandwidth of the capacitive voltage divider is theoretically infinite on the high frequency side. Thus, as long as the bandwidth of the oscilloscope is compatible with the signal to be measured, the ***DR*** of the divider can be calculated by the equation 4.

$$DR = \frac{C_1 + C_2}{C_1} \tag{4}$$

Great care must therefore be taken in the mechanical production of these dividers in order to minimize the values of the parasitic elements but also in the transmission of this attenuated signal to the oscilloscope.

However, in reality, the above mentioned parasitic effects cannot be neglected at high frequencies and are very difficult to be estimated and corrected. In the Fig.9, the measurement cable connected between the divider and the oscilloscope, due to a high value resistor on the output side ***R0*** (1 M***Ω)***, a reflection phenomenon appears at this end. To avoid the establishment of standing waves, this measurement cable is adapted, at its end on the divider side, by a resistance ***R1*** of value equal to its characteristic impedance (see Fig.9). Thus, a voltage step arriving at the terminals of ***C2*** sees its amplitude divided by two at the cable input because of the divider formed by the ***50 ohms*** resistance and the characteristic impedance of the cable. The voltage wave crosses the measurement cable and then is reflected at its end. The reflection due to the oscilloscope input impedance (similar to an open circuit on the divider bandwidth) doubles the amplitude of the incident signal. The oscilloscope therefore measures the original amplitude of the high voltage step. The reflected wave crosses the cable again then is absorbed by the ***50 ohms*** resistor since ***C2*** is equivalent to a short circuit for high frequencies. Without the ***50 ohms*** resistance, a standing wave phenomenon would appear in the measurement cable. It would be the cause of a significant degradation of the shape of the measured signal by adding oscillations. In reality, during this phenomenon, the capacitor ***C2*** does not really works as a short circuit and continues to keep discharging and its discharge time is of the order of magnitude of the time taken by the wave to make a round trip in the cable causing an overshoot on the measured pulse. Consequently, the overshoot becomes more and more significant for longer cable lengths [72].

As a result, the above mentioned parasitic elements limit the bandwidth of the divider to only few hundreds of megahertz and the divider becomes inefficient for the measurements of the high voltage pulses in the domain of nanosecond and sub-nanoseconds.

1.3.3. D-dot sensors

In principle, D-dot sensors are capacitive voltage dividers; however, due to their construction they possess better characteristics such as wide frequency bandwidth, high linearity, and good stability than the capacitive voltage divider principle mentioned in the section *1.3.2*, and are widely used to realize the non-contact measurement of transient electric fields [73]–[78]. Moreover, they function on a passive non-contact measurement method that is simple to implement and non-intrusive to the measurement setups. A D-dot sensor installed in a coaxial transmission line and its equivalent circuit are presented in the Fig.10, where $\boldsymbol{C_1}$ is the high voltage arm capacitance between the sensor and the high-voltage electrode with the voltage $V_1(t)$ generated by the HPP generator and $\boldsymbol{C_2}$ is the low voltage arm capacitance between the sensor and the grounded shielding of the transmission line.

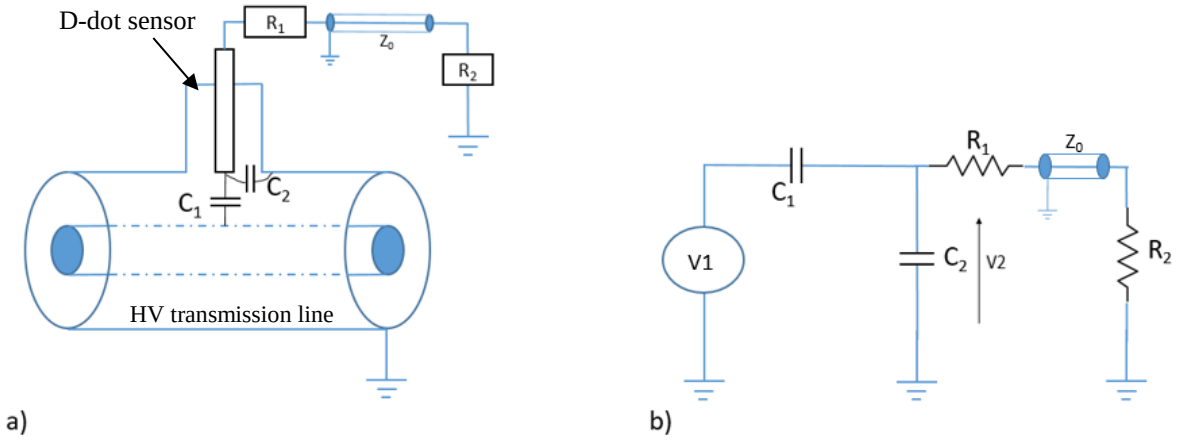

Fig. 10. a) D-dot sensor mounted on a high voltage (HV) coaxial transmission line; b) equivalent electrical circuit of a D-dot sensor

The output of the sensor, $V_2(t)$, is transmitted to a oscilloscope through a pickup resistor R_1 and a cable of the characteristic impedance Z_0, which is matched with the input impedance of the oscilloscope R_2. In the case where the characteristic time constant, defined as the product of resistance and capacitance of the detector circuit, is sufficiently small as compared to the rise time (t) of the pulse to be measured, $(R_1 + Z_0)(C_1 + C_2) \ll$ t, the output voltage of the sensor can be expressed by the equation (5) [79]–[81]:

$$V_2(t) = (R_1 + Z_0) \cdot C_1 . \frac{dV_1(t)}{dt} \quad (5)$$

It can be noticed from the equation (5) that the output is in a derivative form and it is necessary to integrate this signal to determine the actual value of the output. This can be done either by inserting an integrator device in the measurement chain or can also be done mathematically. This functioning regime of the sensor is called differentiating regime.

On the other hand, for the higher characteristic time constant of the sensor as compared to the rise time of the signal, $(R_1 + Z_0)(C_1 + C_2) \ll$ t, the output of the sensor is directly proportional to the input pulse, and this functioning regime of the sensor is called self-integrating regime given by the equation:

$$V_2(t) = \frac{C_1}{C_1 + C_2} \cdot V_1(t) \tag{6}$$

These functioning regimes are presented in the Fig.11, which represents the frequency characteristics of the capacitive voltage dividers as a function of characteristic time constant of the divider $\boldsymbol{\omega\tau}$, where $\boldsymbol{\tau}$ is the time constant of divider [81].

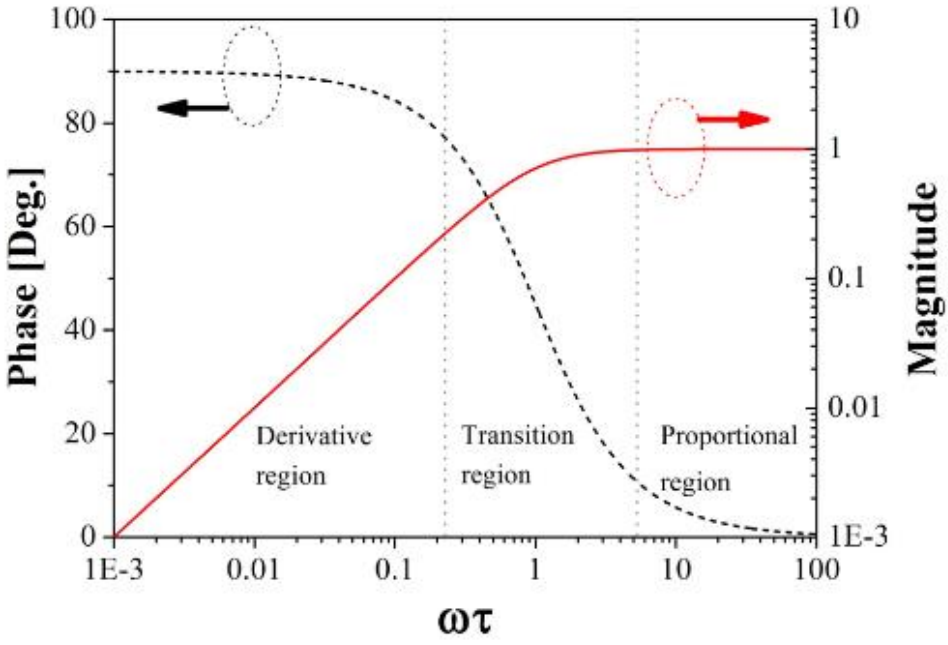

Fig. 11. Frequency response characteristic of the capacitive voltage dividers showing different working regimes (modes) as a function of characteristic time constant ($\boldsymbol{\omega\tau}$) of the divider [81].

Mostly, the D-dot sensors are designed to work in the derivative regime because they are relatively easy to fabricate than the ones working in the proportional regime, but on the cost of accuracy and precision. Indeed, sensors working in the proportional regime need a lot of precaution during fabrication and require extensive 3D electromagnetic modelling as no other reference divider is available to verify the exactitude of the signals measured through these dividers, which rends the calibration of these dividers a tiresome task. However, they are more accurate and precise, if developed correctly, than the ones working in the derivative regime because the errors from the passive integrators or through mathematical operations during the integration of the derivative signal can be avoided.

1.3.4. Capacitive voltage divider based on transmission line principle

To avoid above mentioned problems in the precise and accurate measurements of high voltage fast pulses, in nanosecond and sub nanosecond domain, this fourth type of voltage divider based on transmission line principle could be very efficient. This principle was first presented by M. Blanchet in 1971 [82]. The capacitors of this divider are sections of coaxial lines as presented in the Fig.12.a), where $\boldsymbol{V_{in}(t)}$ is the high voltage peak generated by the high voltage pulse generator, $\boldsymbol{Z_0}$ is the characteristic impedance of the main high voltage transmission line, $\boldsymbol{Z_1}$ and $\boldsymbol{Z_2}$ are the characteristic impedances of the divider section of the main transmission line, $\boldsymbol{R_0}= \boldsymbol{Z}= 50\ \Omega$, R is the 50 Ω input impedance of the oscilloscope and $\boldsymbol{V_{out}(t)}$ is the low voltage pulse measured at the oscilloscope input. A practical design of the capacitive voltage divider based on transmission line principle is shown in the Fig.12.b).

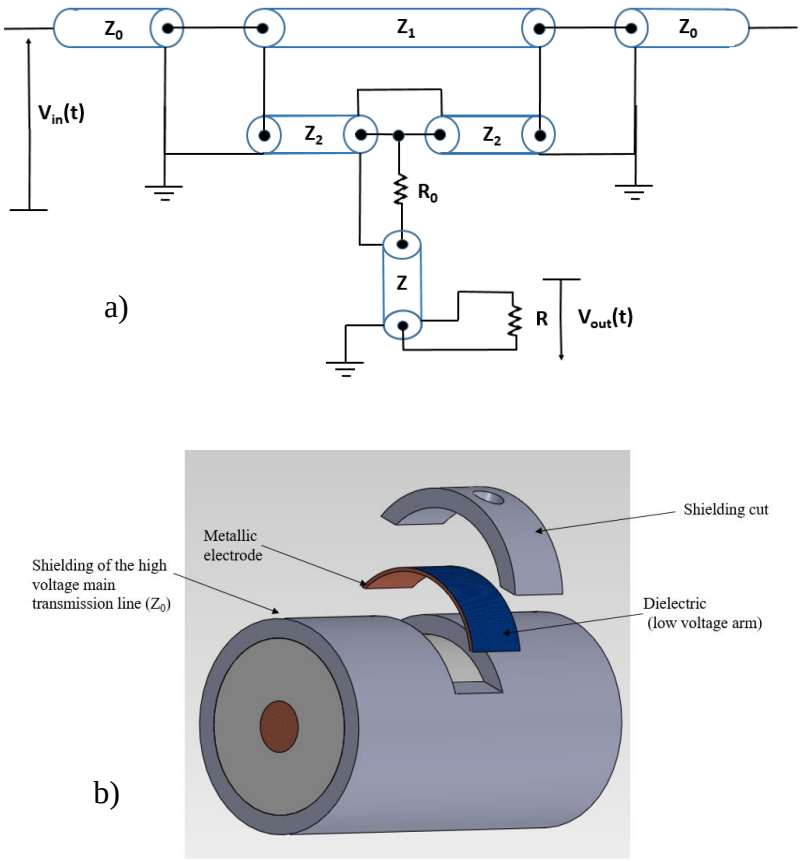

Fig. 12. a) Principle of capacitive voltage divider based on transmission line; b) an example of conception of the divider

Following this principle, a capacitive voltage divider if formed by replacing a section of the high voltage coaxial transmission line of characteristic impedance Z_0, by a section of two concentric coaxial transmission lines, with characteristic impedances Z_1 and Z_2. Given that the characteristic impedance resulting from the association of these two transmission lines is equal to that of the line in which the measurement is made: $Z_0 = Z_1 + Z_2$. In practice, as shown in the Fig.12.b, this is generally done by opening a part of the shielding of the high voltage main transmission line of characteristic impedance Z_0, and inserting a metallic electrode with a dielectric placed on its outer curved surface. After this process, the shielding is closed again. The transmission line with the characteristic impedance Z_1 is formed between the electrode and the central conductor of the main transmission line and the one with characteristic impedance Z_2 is formed between the electrode and the shielding.

During the transmission of a signal in the main transmission line, the high voltage pulse crosses the inner conductor of the impedance line Z_1. The voltage available in this

line is sampled via a coaxial cable ***Z***, each end of which has a 50 Ω resistor R_0 and ***R***. Sampling is generally carried out at an equal distance from the ends of the impedance line section Z_2, the region where the TEM mode of propagation of the voltage wave is best established. The 50 Ω resistor R_0 upstream of the cable ***Z*** plays the same role of the matching resistor as explained for the *capacitive voltage divider* in the paragraph *1.3.2*. It helps to avoid the creation of standing waves in the circuit as the characteristic impedance of the line Z_2 is generally kept very low for high division ratios. Furthermore, it doubles the dividing ratio of the divider when the oscilloscope is used on its 50 Ω input impedance. The voltage division ratio (***DR***) between the real signal $V_{in}(t)$ and the measured attenuated signal $V_{out}(t)$ is based solely on the capacitances per unit length C_1 and C_2 of the lines Z_1 and Z_2 respectively, as presented in the equation (7), thus avoiding the negative effects generated by the parasitic impedances present in the circuit.

$$DR = 2\frac{Z_0}{Z_2} = 2\frac{Z_1 + Z_2}{Z_2} = 2\frac{C_1 + C_2}{C_1} \tag{7}$$

This principle of dividers can be used to measure voltage peaks ranging from a few kilovolts to several megavolts and in a very wide frequency bands extending up to few gigahertz. The efficient working of this type of voltage divider is subjected to choosing the appropriate materials and respecting the necessary dielectric distances.

1.4. SI traceability

1.4.1. The International System of Units: SI

It all started in Paris in the year 1799, when to perform correct measurements of length and mass, the first ever measurement standards in form of two platinum standards representing the metre and the kilogram were deposited. These standards are shown in the Fig.13. This marked the birth of the Metric system, the forerunner of the present International System of Units – the SI system.

Fig. 13. Platinum standards kilogram and meter

The SI is the only system of units that is universally recognized, so that it has a distinctive advantage in establishing an international dialogue. There are seven base units in the SI, presented in the Table 1, from the combination of which many other units are defined in various domains and are called derived units. Some of the derived units in the domain of electricity and magnetism are presented in the Table 2. Each base unit is unique and provides a sound theoretical basis upon which the most accurate and reproducible measurements can be made. However, there are other units, non-SI units, which are defined in terms of SI units, such as among others, minute, hour, day as units of time.

Table 1. Base units in the SI

Base quantity		**Base unit**	
Name	**Typical symbol**	**Name**	**Symbol**
time	t	second	s
length	l, x, r, etc.	metre	m
mass	m	kilogram	kg
electric current	I, i	ampere	A
thermodynamic temperature	T	kelvin	K
amount of substance	n	mole	mol
luminous intensity	Iv	candela	cd

Table 2. Derived electrical quantities and SI units

Derived quantity	**Derived unit**	**Symbol for unit**	**Expression in terms of other units**
Frequency	hertz	Hz	s^{-1}
Force	newton	N	$m .kg .s^{-2}$
Energy	joule	J	N.m
Power	watt	W	J/s
Electric charge	coulomb	C	A.S
Electric potential difference	volt	V	W/A
Capacitance	farad	F	C/V
Electric resistance	ohm	Ω	V/A
Electric conductance	siemens	S	A/V
Magnetic flux	weber	Wb	V.S
Magnetic flux density	tesla	T	Wb/m^2
Inductance	Henry	H	Wb/A

Since 2018, the definition of the SI units is established in terms of a set of seven defining constants. The complete system of units can be derived from the fixed values of these defining constants, expressed in the units of the SI. These particular constants were chosen after having been identified as being the best choice, taking into account the previous definition of the SI, which was based on seven base units and some of the units were defined by physical artefacts, and progress in science. They are chosen in such a way that any unit of the SI can be written either through a defining constant itself or through linear combinations of these defining constants. Most importantly, the numerical values of the seven defining constants have no uncertainty. These seven defining constants of the SI and the seven corresponding units they define are presented in the Fig.14. The units such as hertz (Hz), joule (J), coulomb (C), lumen (lm), and watt (W), are related to the base units second (s), metre (m), kilogram (kg), ampere (A), kelvin (K), mole (mol), and candela (cd), according to Hz = s^{-1}, J = kg m^2 s^{-2}, C = A s, lm = cd m^2 m^{-2} = cd sr, and W = kg m^2 s^{-3} [83].

Defining constant	Symbol	Numerical value	Unit
hyperfine transition frequency of Cs	$\Delta\nu_{Cs}$	9 192 631 770	Hz
speed of light in vacuum	c	299 792 458	m s^{-1}
Planck constant	h	$6.626\,070\,15 \times 10^{-34}$	J s
elementary charge	e	$1.602\,176\,634 \times 10^{-19}$	C
Boltzmann constant	k	$1.380\,649 \times 10^{-23}$	J K^{-1}
Avogadro constant	N_A	$6.022\,140\,76 \times 10^{23}$	mol^{-1}
luminous efficacy	K_{cd}	683	lm W^{-1}

Fig. 14. Seven defining constants and the units they define [83]

1.4.2. Metrology

As it is very well known that the science is completely dependent on the measurements and good measurements can significantly increase the value, the effectiveness, the quality and even the better comprehension of results. However, the question arises that how to judge a good measurement and what is the level of confidence in the performed measurement. This is where the metrology comes into play.

Metrology is defined in VIM, International vocabulary of metrology [84], as the science of measurement and its applications. It includes all theoretical and practical aspects of measurement, whatever the measurement uncertainty and field of application. It covers three main activities:

1. The **definition** of internationally accepted units of measurement.
2. The **realization** of units of measurements by scientific methods.
3. The establishment of **traceability** chains by determining and documenting the value and accuracy of a measurement and disseminating that knowledge.

The two most important aspect of metrology that is concerned in this thesis work are the measurement standards and the traceability chain to SI. A measurement standard or etalon, is defined as the material measure, measuring instrument, reference material or measuring system intended to define, realise, conserve or reproduce a unit or one or more values of a quantity to serve as a reference. Whereas a traceability chain is an unbroken chain of comparisons, all having stated uncertainties, which ensures that a measurement result or the value of a standard is related to reference at highest levels, ending at the primary standard. A traceability chain is presented in the Fig.15.

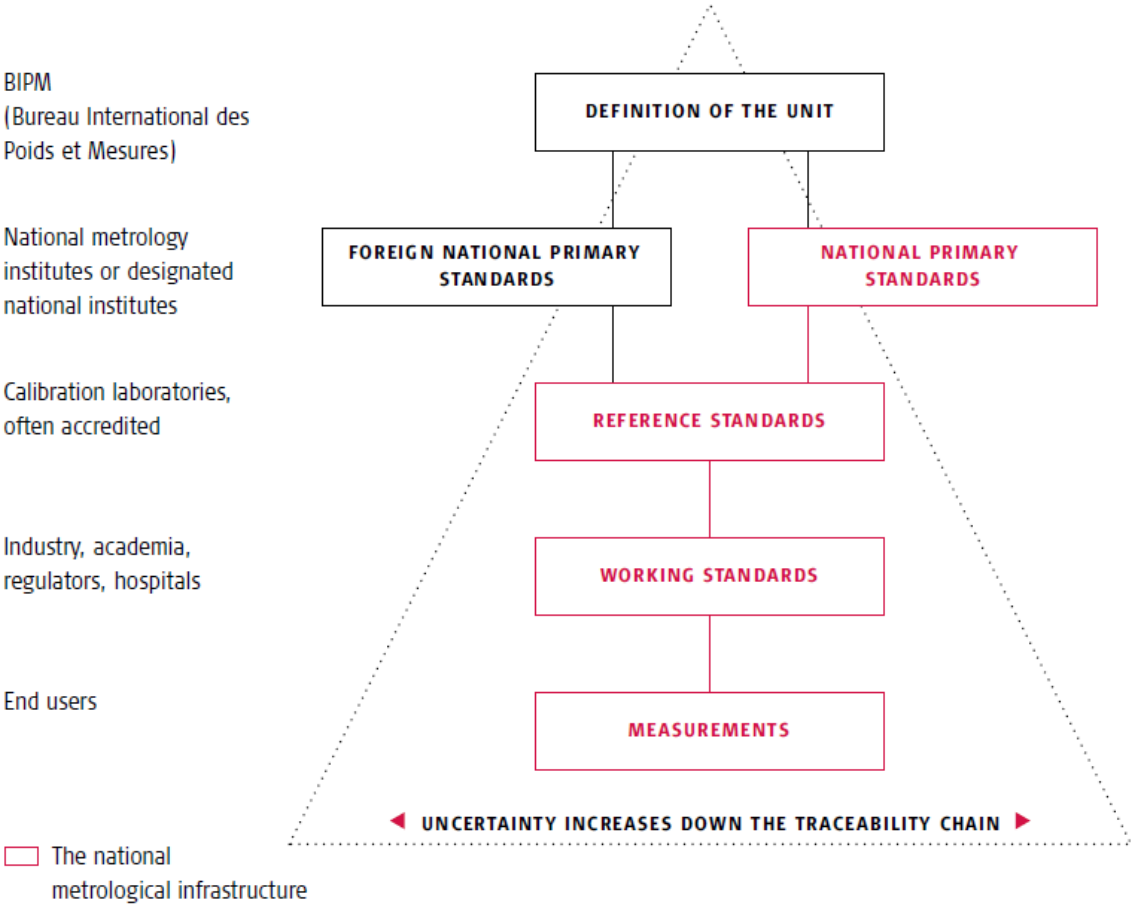

Fig. 15. Traceability chain [85]

Additionally, a basic tool in ensuring the traceability of a measurement is the calibration of a measuring instrument, measuring system or reference material. Calibration determines the performance characteristics of an instrument, system or reference material. It is an operation that, under specified conditions, in a first step, establishes a relation between the quantity values with measurement uncertainties provided by measurement standards and corresponding indications with associated measurement uncertainties and, in a second step, uses this information to establish a relation for obtaining a measurement result from an indication. Moreover, a calibration may be expressed by a statement, calibration function, calibration diagram, calibration curve, or calibration table. In some cases, it may consist of an additive or multiplicative correction of the indication with associated measurement uncertainty. The capabilities of National Metrology Institutes (NMI) to perform calibrations are resumed in CMCs (Calibration and Measurement Capabilities) and are published in the BIPM (Bureau International des Poids et Mesures) key comparison database (KCDB) of the CIPM-MRA (Comité International des Poids et Mesures – Mutual Recognition Arrangement).

1.4.3. SI traceability of the HPPNS

During the past few decades, there has been a lot of progress in terms of generations of the high voltage fast pulses in the domain of nanosecond and sub-nanosecond and new applications keeps emerging very frequently in military, civil and medicals sectors. For these applications, nanosecond or sub nanosecond pulsed power need to be controlled with sufficient uncertainties (less than 5 %) in order to achieve efficient results without irradiating the targeted objects, or the intermediate ones, and to achieve a better control of the pulsed power. For most of the research laboratories, in almost all cases, the generation and the measurement systems in these technologies are most often developed by the laboratories itself and are without any concrete metrological traceability. Moreover, reliable and versatile commercial devices for this level of power are not available or very rare in the market. The calibrations of these systems are generally carried out only at low levels of amplitude by comparison with existing commercial probes, which have limited bandwidths, and sometimes at higher frequencies using Vector Network Analysers and that too at low power. Therefore, the validity of the measurement is based exclusively on these commercial instruments and at low power levels; and the traceability is not then assured.

The metrology is very well established for high voltage microsecond and millisecond pulses up to voltage amplitudes of few million-volts [86]. However, the NMIs still do not issue calibrations for high voltage faster pulses in the domain of nanosecond, and the metrology is absent for these kind of pulses. For instance, the fastest rise time covered by the CMC is limited to 6 ns and that too for voltage peaks only up to 100 kV and for faster pulses with higher voltage peaks than 100 kV the traceability is completely absent [2], [86].

1.5. Aim of the thesis

The aim of this thesis is to accompany the industries and research laboratories in the domain of high voltages nanosecond and sub-nanosecond pulses to perform precise and accurate measurements. A metrology infrastructure must be developed which should be capable to insure SI traceable measurements of all the parameters of high voltage fast pulses, such as the peak voltage, rise time, pulse duration and pulse fall time and that for all kinds of pulses. To obtain this objective, a measurement standard system should be developed for measurements of high voltage fast pulses. The capabilities of the measurement system to measure the concerned pulse parameters are listed in the Table 3.

Table 3. Objectives related to pulse parameters to be measured with concerned target uncertainties

Pulse parameters	**Target**	
	Values	**Uncertainty (k=2)**
Voltage amplitude (V)	$V \leq 500$ kV	3 % to 5 %
Rise time (t_r)	few hundreds of picoseconds to few nanoseconds	few hundreds of picoseconds (absolute uncertainty)
Duration (t_d)	$t_d \leq 100$ ns	few hundreds of picoseconds (absolute uncertainty)

This thesis work aims to provide industries and research laboratories a standard calibration system traceable to the SI for their HPPNS generation and measurement systems.

CHAPTER

2

An overall view of the design of a calculable capacitive voltage divider is presented in this chapter. This divider is the most critical component of the standard measurement system developed in this thesis work. A systematic conception of the divider is illustrated from analytical analysis and numerical electromagnetic modelling to the fabrication of the final elements constituting the divider. Intermediate and post-production testing and validation of the awaited performance of the main elements of this divider are also presented.

Chapter 2: Conception and Modelling of a Calculable Capacitive Voltage Divider (CCVD)

Voltage dividers, also very frequently called voltage sensors [2], [75], [81], for high voltage measurements are an essential ingredient for successful operation of many pulsed power systems [87]. These systems demand very rapidly rising voltages and consequently require accurate and precise measurement of high transient voltages of very short rise times [54]. However, as mentioned in the previous chapter, the conventional voltage dividers, such as, resistive and capacitive and even D-dot sensors are unsuitable in the monitoring of these fast voltage transients. Moreover, even if we have a suitable voltage divider that is capable of measuring these high transient voltages without perturbations and with a good accuracy and precision, the absence of metrology for these high voltage transients still makes it difficult to be sure about the parameters measured of these high voltage rapid pulses. The measurement standard system developed in this thesis work aims to respond to the above-mentioned needs as well as to ensure the SI traceability of high voltage pulses in the domain of nanosecond and sub-nanosecond. This measurement standard is calculable and calibrated through SI

traceable standards. The central element of this measurement system is a calculable large bandwidth voltage divider.

This chapter is a thorough description of the voltage divider developed in this thesis work, from the choice of the working principle to the electrical and electromagnetic modelling and the optimization of the divider response in the required frequency bandwidth. Different elements constituting the divider are also described and the different mechanical parts developed are presented. Testing and validation of these parts are also detailed.

2.1. Prerequisites and the choice of the principle

For the measurement of high voltage pulses in the domain of nanosecond and sub-nanosecond, the voltage divider developed must make it possible to observe, without disturbing the high voltage circuit, transient voltage pulses delivered by the pulse generators. A broadband oscilloscope is then used in the measurement chain to acquire these signals, as represented in the Fig.7 of the chapter 1. The main requirements for the development of the voltage divider are as follows:

I. The frequency band covered by the divider must be compatible with the rapidity of the temporal variations of the pulses to be measured. Actually, the rise time of nanosecond or sub-nanosecond impulse voltage is very short, and the wave tail time can reach up to several tens of nanoseconds. Therefore, it is necessary to develop a broadband voltage divider for measuring common nanosecond and sub-nanosecond impulse voltages accurately. In our case, we want the divider to have a high cut-off frequency that allows it to measure sub-nanosecond rise and/or fall times. From equation (1), to measure a pulse with a rise time of 0.5 ns, the divider should have a high cut-off frequency superior than 0.7 GHz. Similarly, to measure pulses with slower rise or fall times of values around 5 nanoseconds, the low cut-off frequency should not be more than few tens of MHz.
II. A flat frequency response of the voltage divider is required. The attenuation factor or in other words the division ratio of the divider must possess linear phase responses as a function of frequency to avoid any deformation of the incident pulse.

III. The division ratio must be high enough to be able to perform waveform analysis through oscilloscopes with a sufficiently high signal-to-noise ratio. For example, to measure voltages of 100 kV, with an oscilloscope whose maximum range is 1V/div (10V full scale), the division ratio of the divider must be at least 10^4:1, i.e. an attenuation of approximately 80 dB. To increase further this attenuation, commercial attenuators can complete the measurement chain between the divider and the oscilloscope.

IV. The device must be able to withstand very high voltages. In this work, peak voltages up to 500 kV are aimed. Therefore, the choice of insulating components and the mechanical design must take into account the distances imposed by the dielectric strengths of each insulating material used.

V. High level of electromagnetic immunity is required for interference free measurements of signals.

The principle of voltage dividers presented in the section *1.3*, such as the resistive and the capacitive voltage dividers are unsuitable to meet above–mentioned requirements specially because the highest values of the bandwidths that can be attained with these dividers are still lower than bandwidths of the signals, at least 0.7 GHz, that is to be measured in this thesis. On the other hand, supplementary integrator necessary in the case of D-dot sensors induce errors in the measurements of the waveforms rendering these sensors inappropriate for the accurate and precise measurements of high voltage pulses in the domain of nanosecond and subnanosecond. The most appropriate divider principle capable to respond to the requirements of the signals to be measured in this thesis is a voltage divider based on the transmission line capacitive voltage divider principle, which is described in the paragraph *1.3.4*. A voltage divider based on this principle is developed and presented in the following sections.

2.2. Analytical model of the CCVD

Following the principle of a voltage divider based on the transmission line principle, a voltage divider is obtained by replacing a section of the main coaxial transmission line at the output of the pulse generation system, of characteristic impedance $\boldsymbol{Z_0}$, by a section of two concentric transmission lines, of characteristic impedances $\boldsymbol{Z_1}$ and $\boldsymbol{Z_2}$. An important aspect to take under consideration is that the impedance resulting from the association of these two lines has to be equal to that of the main line in which the measurement is made, i.e. $\boldsymbol{Z_0 = Z_1 + Z_2}$. The division ratio of such divider can be expressed using the equation (7), described in the previous chapter, and it depends only upon the capacitances per unit length $\boldsymbol{C_1}$ and $\boldsymbol{C_2}$ of the lines $\boldsymbol{Z_1}$ and $\boldsymbol{Z_2}$ respectively. A detailed derivation of the equation (7) is presented in this section based on a geometrical model of the *CCVD* shown in the Fig.16, where it can be noticed that that the intermediate electrode, the ***Electrode1***, used to form the second concentric transmission line does not cover the whole circumference of the dielectric $\boldsymbol{\varepsilon_1}$ and has a width limited only to a value ***d***. This is principally due to the fact that the characteristic dimension of this electrode must satisfy the conditions of quasi-steadiness. This condition is discussed more in detail in the section *2.2.2.2* of this chapter.

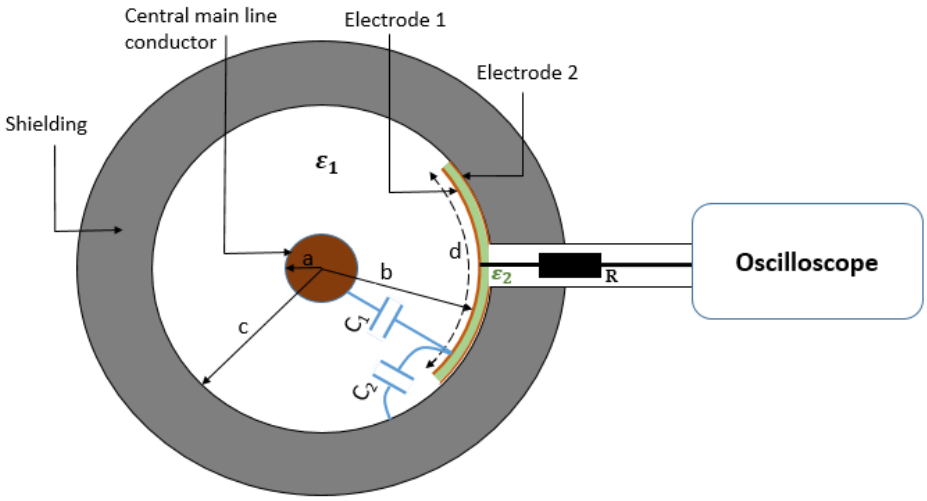

Fig. 16. Geometrical model of the CCVD (a cross section) with its output connected to an oscilloscope: a, b and c are the different radii of the high voltage line, inserted coaxial electrode and the shielding respectively; d is the width of the Electrode1; ε_1 and ε_2 are the relative permittivity of the dielectrics of the lines Z_1 and Z_2 respectively; and R represents the matching 50 Ω resistor at the output of the divider.

During the transmission of transverse electromagnetic (TEM) wave along a coaxial line, the electric field intensity is directed radially along the axis normal to the cylindrical surface. The expression of the electric field intensity ($\boldsymbol{E_r}$) with respect to the radial vector $\hat{r}$ for a coaxial lines can be found using Gauss's law[2]:

$$E_r = \frac{Q}{2\pi\varepsilon_0 L r} \tag{8}$$

where $\boldsymbol{Q}$ is the total charges enclosed in the central conductor of infinitely long length $\boldsymbol{L}$ and $\boldsymbol{r}$ is the radius of the Gaussian closed surface between the conductors. Furthermore, the potential difference between the inner and the outer conductor radii $\boldsymbol{a}$ and $\boldsymbol{b}$ of the transmission line with a dielectric of permittivity $\boldsymbol{\varepsilon_1}$ can be given by the equation (9):

$$V_{ab} = -\int_{r=b}^{r=a} E_r\, dr = -\int_{r=b}^{r=a} \frac{Q}{2\pi\varepsilon_0\varepsilon_1 L}\frac{dr}{r} = \frac{Q}{2\pi\varepsilon_0\varepsilon_1 L} ln\left(\frac{b}{a}\right) \tag{9}$$

Similarly, the potential difference between the ***Electrode1*** and the shielding with a dielectric of relative permittivity $\boldsymbol{\varepsilon_2}$ can be found to be:

$$V_{bc} = -\int_{r=c}^{r=b} E_r\, dr = -\int_{r=c}^{r=b} \frac{Q}{2\pi\varepsilon_0\varepsilon_2 L}\frac{dr}{r} = \frac{Q}{2\pi\varepsilon_0\varepsilon_2 L} ln\left(\frac{c}{b}\right) \tag{10}$$

where, ***Electrode1*** is at floating potential with induced charges –Q on its inner surface and +Q on its outer surface.

The voltage applied to the coaxial line, V_{ac} is the sum of these two voltages:

$$V_{ac} = V_{ab} + V_{bc} \tag{11}$$

Furthermore, in the Fig.16, the 50 Ω resistor $\boldsymbol{R}$ upstream of the cable plays the same role as in the case of the capacitive voltage divider previously presented in the section *1.3.2*, in addition to its impedance matching role between the coaxial cable connecting the

[2] The net electric flux through any hypothetical closed surface is equal to $\frac{1}{\varepsilon_0}$ times the net electric charge within that closed surface [88], where ε_0 is the permittivity of free space.

oscilloscope and the *CCVD*, it doubles the dividing ratio of the divider. Therefore, the division ratio ***DR*** of the divider can be calculated as:

$$DR = 2 \cdot \frac{V_{ab} + V_{bc}}{V_{bc}} = 2 \cdot \frac{\frac{1}{2\pi\varepsilon_0\varepsilon_1} ln\left(\frac{b}{a}\right) + \frac{1}{2\pi\varepsilon_0\varepsilon_2} ln\left(\frac{c}{b}\right)}{\frac{1}{2\pi\varepsilon_0\varepsilon_2} ln\left(\frac{c}{b}\right)} \tag{12}$$

Moreover, the capacitance per unit length $\boldsymbol{C_x}$ (F/m) between these cylindrical conductors can be calculated through the relation, where $\boldsymbol{V_x}$ is the potential difference between the two cylindrical conductors:

$$C_x = \frac{Q}{V_x L} \tag{13}$$

which gives from equations (9) and (10):

$$C_1 = \frac{Q}{V_{ab} L} = \frac{2\pi\varepsilon_0\varepsilon_1}{ln\left(\frac{b}{a}\right)} \tag{14}$$

$$C_2 = \frac{Q}{V_{bc} L} = \frac{2\pi\varepsilon_0\varepsilon_2}{ln\left(\frac{c}{b}\right)} \tag{15}$$

where $\boldsymbol{C_1}$ is the capacitance per unit length between the central conductor of the main transmission line and the ***Electrode1***; and $\boldsymbol{C_2}$ is the capacitance per unit length between the ***Electrode1*** and the shielding of the main transmission line.

By replacing the equations (14) and (15) in the equation (12), we get the value of the ***DR*** which is solely dependent on the capacitances per unit length of the capacitors formed:

$$DR = 2 \cdot \frac{V_{ab} + V_{bc}}{V_{bc}} = 2 \cdot \frac{\frac{1}{C_1} + \frac{1}{C_2}}{\frac{1}{C_2}} = 2 \cdot \frac{C_1 + C_2}{C_1} \tag{16}$$

Furthermore, since both the capacitors formed by these capacitances per unit lengths, the high voltage arm capacitor $\boldsymbol{C_H}$ of capacitance per unit length $\boldsymbol{C_1}$ and the low voltage arm capacitor $\boldsymbol{C_L}$ of capacitance per unit length $\boldsymbol{C_2}$, are the segments of a cylindrical

capacitors, their capacitance values can be calculated through their respective capacitances per unit length [89]:

$$C_H = \frac{2\pi\varepsilon_0\varepsilon_1}{\ln\left(\frac{b}{a}\right)} \cdot L \cdot \frac{d}{2\pi b} \tag{17}$$

$$C_L = \frac{2\pi\varepsilon_0\varepsilon_2}{\ln\left(\frac{c}{b}\right)} \cdot L \cdot \frac{d}{2\pi b} \tag{18}$$

where ***L*** and ***d*** are the length and the width of the *Electrode1* represented in the Fig.16.

According to the equation (16), to attain high values of ***DR*** of the divider, the value of the low voltage arm capacitance per unit length $\boldsymbol{C_2}$ must be chosen to be very high to that of the high voltage arm $\boldsymbol{C_1}$.

Furthermore, the low voltage arm capacitor is functionally an electric field strength sensor and for low thickness of the intermediate electrode, the ***Electrode1***, the distributions of the electric and magnetic fields in the line are not modified by its introduction. Therefore, it can very well provide measurements with minimal distortions of a pulse shape up to the subnanosecond ranges [90]. The design of the different parts of the *CCVD* is given in the following sub-sections.

2.2.1. High voltage arm

During the first phases of the development, it was necessary to choose the dimensions of some of the parts of the divider, which would be constant throughout the development phase and the dimensions of other parts could be optimized with respect to these parts. The most important aspect of the *CCVD* is its characteristic impedance. A schematic of an infinitesimal segment of a transmission line for analysis is presented in the Fig.17, where ***R, L, G, C*** represent per unit length values of the resistance, inductance, conductance and capacitance respectively. The main transmission line can be seen as the series combination of infinite numbers of these segments.

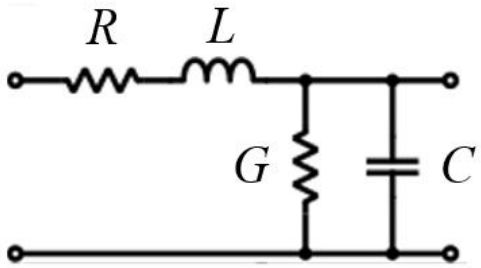

Fig. 17. Model of an infinitesimal segment of a coaxial transmission line

Through the Fig.17, the characteristic impedance Z_0 of the transmission line can be calculated by the equation:

$$Z_0 = \sqrt{\frac{R + j\omega L}{G + j\omega C}} \tag{19}$$

which can be developed to:

$$Z_0 = \sqrt{\frac{L}{C}} \sqrt{\frac{1 - j\left(\frac{R}{\omega L}\right)}{1 - j\left(\frac{G}{\omega C}\right)}} \tag{20}$$

Furthermore, well-functioning transmission lines have very low values of R and G, however for higher values of ω, the values $\left(\frac{R}{\omega L}\right)$ and $\left(\frac{G}{\omega C}\right)$ become negligible and the transmission line can be considered as a lossless line rendering the equation (20) to:

$$Z_0 = \sqrt{\frac{L}{C}} \tag{21}$$

With the line parameters illustrated in the Fig.18 the values of the L and C can be calculated through [91]:

*Fig. 18. Section of coaxial transmission line showing the diameter of the inner conductor **a** and the shielding diameter **c***

$$L = \frac{\mu_0 \mu_1}{2\pi} ln \frac{c}{a} \tag{22}$$

$$C = \frac{2\pi \varepsilon_0 \varepsilon_1}{ln \frac{c}{a}} \tag{23}$$

where:

μ_0: permeability of free space ($\mu_0 = 1.25663706212 \times 10^{-6}$ H/m)

μ_1: relative permeability of the dielectric of the main transmission line

ε_0: permittivity of free space ($\varepsilon_0 = 8.8541878128 \times 10^{-12}$ F/m)

ε_1: relative permittivity of the dielectric of the main transmission line

Z_0: characteristic impedance of the main transmission line (50Ω)

c : inner diameter of the metallic shielding of the transmission line

a : diameter of the central copper conductor of the transmission line

The divider is to be employed with a 50 Ω system, consequently the characteristic impedance of the divider must be the same to avoid any mismatching and reflections of signals. To determine the dimensions of the main transmission line of characteristic impedance Z_0, i.e. 50 Ω, the following equation was obtained from the equations (21 - 23):

$$Z_0 = \frac{1}{2\pi} \sqrt{\frac{\mu_0 \mu_1}{\varepsilon_0 \varepsilon_1}} \; ln \frac{c}{a} \tag{24}$$

It was decided that the *Polytetrafluoroethylene* (PTFE) would be used as the dielectric material of the main transmission line. The reasons behind this approach is that PTFE has a low value of the dielectric constant ($\boldsymbol{\varepsilon_1} \approx 2.1$), low dielectric losses (so small tan δ) and relatively high value of the dielectric strength (≈ 40 kV/mm) to withstand the high voltage peaks. The value of ***a/2*** is chosen to be 12.7 mm, which is the same value of the radius of the ceramic resistor that is used in 50 **Ω** load of the measurement system described in the next chapter and it also helps to keep constant the value of the radius of the main conductor throughout the length of the measurement system. With the help of these values, the inner radius of the transmission line shielding ***c/2*** is calculated to be 42.55 mm through the equation (25), which would provide a more than sufficient dielectric thickness of 29.85 mm between the center conductor and the metallic shielding (at least 13 mm of PTFE thickness is necessary to withstand 500 kV of peaks) of the transmission line. All of these characteristics of the high voltage arm of the divider is resumed in the Table 4.

$$c = a \cdot e^{\frac{Z_0 \, 2\pi}{\sqrt{k}}} \quad \text{where } k = \frac{\mu_0 \mu_1}{\varepsilon_0 \varepsilon_1} \tag{25}$$

Table 4. Characteristics of the high voltage arm of the CCVD

Component	**Material**	**Parameter**	**Dimensions (mm)**
Central conductor	Copper	Radius	12.7
		Length	60
Dielectric ε_1	PTFE	Inner radius	12.7
		Outer radius	42.55
Shielding	Aluminum	Inner radius	42.55
		Outer radius	60

2.2.2. Low voltage arm

For the voltage dividers based on the transmission line principle, the conception of the low voltage arm capacitor formed by the capacitance per unit length C_2 is the most critical part. Its conception determines not only the division ratio of the divider but also its frequency response and the long-term stability of the *CCVD*. Several precautions must be taken during the conception and realization of the metallic electrodes as well as the dielectric present between them. Different elements of the low voltage arm of the divider have been developed in this thesis work and are presented in the following sections. A schematic model of the low voltage arm of the *CCVD*, derived from the Fig.16 is presented in the Fig.19.

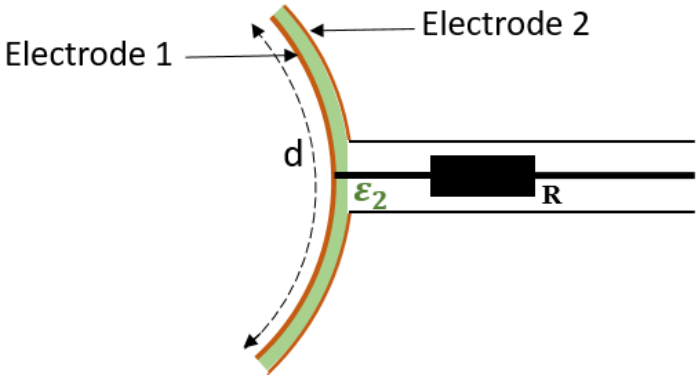

Fig. 19. Geometry of the low voltage arm of the CCVD with the matching resistor R

2.2.2.1. Choice of the dielectric ε_2

An important component of the low voltage arm capacitor is the dielectric material used between the two capacitor electrodes, represented by ε_2 in the Fig.19. It should possess following characteristics before it could be used in the realization of this capacitor.

I. As it is mentioned before that the voltage peaks as high as 500 kV are aimed in this thesis work, the division ratio of the voltage divider developed must be consequently as high as possible, which would permit the pulses with these levels of voltage peaks to be able to be read through calibrated oscilloscope. The dielectric used plays a very important part in

the determination of the division ratio. A very thin layer of the dielectric is needed for high division ratios. Hence, it is extremely necessary that the dielectric used must possess a *very high dielectric strength* so that the high division ratios can be obtained with thin layers without dielectric breakdown.

II. The material used should possess low values of the dielectric losses to avoid supplementary distortions to the output signals due to loss of power in the dielectric in the form of heat. Generally, materials with low permittivity possess low values of dielectric losses.

III. It should have very good adherence properties to the electrodes on which it is placed. This is to ensure the long-term stability of the divider.

IV. A homogeneous thickness of the dielectric material is also necessary as the division ratio of the *CCVD* depends upon the capacitance per unit length of the capacitors constituting the divider. A difference in the thickness of the dielectric deposited will result in different values of the capacitances per unit length and as consequence; the divider will not possess a flat frequency response, which would further apply supplementary distortions on the waveform measured.

Different dielectric materials were studied such as *Kapton, PA11, PTFE* and *SiO_2*, and some of their important electrical properties are listed in the Table 5. All of these materials were chosen for their low permittivity and low losses.

Table 5. Properties of the dielectrics

Material	Dielectric Const.	Dielectric loss	Dielectric strength
	@ 1 MHz	tan δ	kV/mm
Kapton	3	0.0018	22
PTFE	2.2	0.0003	50
PA11	3.5	0.06	30
SiO_2	3.7	0.001	560

Finally, SiO_2 was chosen as the dielectric of the low voltage arm of the CCVD for its high dielectric strength, low permittivity and dielectric losses, good adherence properties to the metallic substrate and its ability to be deposited as a homogeneous thin

film, of few micrometers, through a special deposition technique used in semiconductor technology in clean rooms.

2.2.2.2. Geometry of the Electrode1

An adequate shape and size of the ***Electrode1*** of the divider is very decisive in the performance of the *CCVD*. Its width, ***d***, and shape must be adequate to place a homogeneous thickness of a dielectric material on its outer surface, which is essential in the determination of the capacitance per unit length value of the low voltage arm of the capacitor formed between the ***Electrode1*** and the ***Electrode2***. Consequently, the shape of this element dictates the shape and the size of the low voltage arm capacitor.

The charging of the low voltage arm capacitor takes place in the travelling wave mode, and the *CCVD* operates in the receiving antenna mode of strip-type or umbrella-type [72], [89], [92]. The geometrical shape of the umbrella can be, in principle, arbitrary, but its characteristic dimension (e.g., the radius of a round umbrella) must satisfy the condition of quasi-steadiness. According to this condition, the time of the wave path along the characteristic dimension (***d/2***) of the ***Electrode1*** must be significantly lower than the duration, ***T***, of the measured pulse. For example, for an umbrella electrode [92]:

$$\frac{\mathrm{d}}{2} \ll \frac{\mathrm{T.c}}{\sqrt{\varepsilon_2}} \tag{26}$$

where ***d*** is the umbrella length along the circumference of the transmission line, see Fig.19, ***c*** is the speed of light in vacuum, and $\boldsymbol{\varepsilon_2}$ is the relative permittivity of the dielectric used in the low voltage arm capacitor of the divider. For example, to measure a pulse of a duration ***T***= 0.5 ns and taking a low voltage arm dielectric of a relative permittivity $\boldsymbol{\varepsilon_2} = 3$, the value of ***d*** has to be largely less than 170 mm. Therefore, the duration of the pulse to be measured determines the dimensions of the divider. Furthermore, due to this geometry of the divider the inherent inductance of the ***Electrode1*** is very low, which makes it ideal for fast rise times [47]. Another important element of the divider is the matching resistor ***R*** and fabricated low voltage arm capacitor should facilitate the integration of this resistor to the measurement circuit.

However, as much as it is necessary for the dimensions and shape of the ***Electrode1*** of the *CCVD* to result in a flat frequency response, it is also necessary that the developed electrode must facilitate the deposition of the dielectric material on its

surface for the purposes of a homogeneous deposition of the dielectric and the long-term stability. Different dielectric materials with low permittivity, as presented in the Table 5, were tested for the deposition on curved metallic surfaces with different deposition techniques, such as *PECVD*, *Epitaxy*, *High temperature fusion*, *pulverization*, etc. Nevertheless, all the deposition techniques resulted in inhomogeneous deposition thicknesses of the dielectric material on a curved surface. Therefore, the umbrella geometry of the *Electrode1* was modified to facilitate this process. The best and controlled deposition results were obtained on flat surfaces; consequently, the geometry of the electrode was modified to have two distinct surfaces. A curved surface towards the cylindrical main line PTFE dielectric of the main transmission line and a flat surface for the dielectric deposition. This new Flat and Curved geometry of the *Electrode1*, named as ***FC electrode***, is presented in the Fig.20.

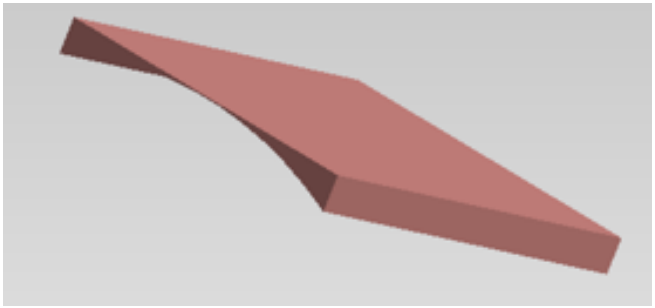

Fig. 20. FC electrode

2.3. Electromagnetic modelling of the CCVD

To study in detail the phenomena and the factors affecting the frequency response and the division ratio of the *CCVD*, electromagnetic modelling was performed using the software *CST Microwave Studio*®. In the beginning, both Time and Frequency domain solvers were considered to analyze the differences between their results for the same modelled geometries of the *CCVD*. The difference between these two solvers is that the time domain solver is based on the Finite Integration Technique (FIT) describing Maxwell's equations on a time-grid space whereas the frequency domain solver is based on the Finite Element Method (FEM). Furthermore, the time domain method uses a hexahedral or a hexahedral transmission-line matrix (TLM) meshing technique for the simulation and is more suitable for calculations over a wide frequency range because only one simulation is required and the frequency response is obtained through Fast Fourier Transform (FFT). Therefore, it is more suitable for simulations of electrically large structures but the calculation time can be very long for large number of mesh cells, as is the case if there are small components present in the modelled structure. On the other hand, the frequency domain solver uses either hexahedral or tetrahedral meshing techniques and discrete simulations are performed at discrete frequencies to cover the entire operating bandwidth. Thus, adaptive refinement of the mesh at every frequency can be performed to obtain the results. Therefore, the frequency domain solver is more suited for the simulations of narrowband and electrically small structures. Both of these solvers possess an automatic meshing tool which generates an initial mesh according to a minimal user input (e.g., number of steps per wavelength), taking into account geometry, material properties, and sharp corners and edges and refine the mesh through an automatic adaptive meshing, until convergence is reached [93], [94].

The simulations of the *CCVD* were basically performed to analyze its Scattering (S) parameters. These parameters are related to the power flow in a transmission line as they relate forward and backward travelling waves between the ports in a transmission line. The *CCVD* can be considered as a two-port network with transmission lines of lengths ℓ_1 and ℓ_2 at each port, as presented in the Fig.21, and the travelling voltage waves at the ports are represented by $V_1^+, V_1^-, V_2^+, V_2^-$. The *Port 1* and *Port 2* represent the high voltage input and the low voltage output of the *CCVD* respectively.

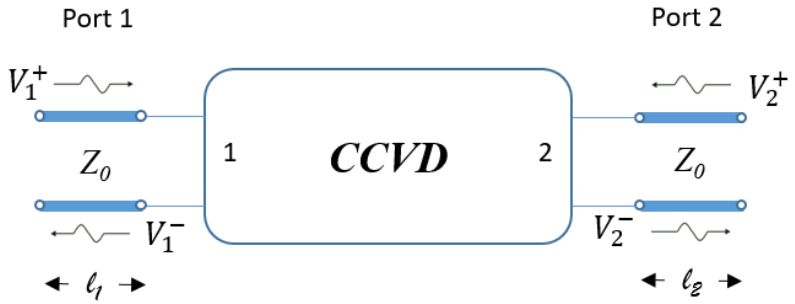

Fig. 21. CCVD as a two-port network with transmission lines at the ports

The two-port S parameters are defined in terms of travelling voltage waves on transmission lines with a real characteristic impedance Z_0 attached to each of the ports of the network, following this configuration these travelling waves towards the outside of the network can be written as [95]:

$$V_1^- = S_{11}V_1^+ + S_{12}V_2^+ \tag{27}$$

$$V_2^- = S_{21}V_1^+ + S_{22}V_2^+ \tag{28}$$

where S_{ij} are the individual S parameters that are determined by measuring the forward and backward travelling waves with loads $Z_L = Z_0$ at the ports. Considering the output of the *CCVD* perfectly matched by the oscilloscope input i.e. this one does not reflects power back which results in the travelling wave $V_2^+ = 0$, and from the equations (27) and (28) the different S parameters can be written as:

$$S_{11} = \frac{V_1^-}{V_1^+}\Big|_{V_2^+=0} \quad ; \quad S_{21} = \frac{V_2^-}{V_1^+}\Big|_{V_2^+=0} \tag{29}$$

It can be noticed from the equation (29) that the S_{11} represents the ratio of the outwards and inwards travelling voltage waves at the port 1, at the input of the *CCVD*, and it is important to have this ratio as small as possible to minimize the reflection which could deform the inward travelling voltage wave (the pulse to be measured) and consequently the measured wave at the output of the *CCVD*. The S_{11} is also called the reflection coefficient. Furthermore, the S_{21} is the ratio between the outward travelling voltage wave at the port 2, at the output of the *CCVD*, and the incident voltage wave at the port 1, at the input of the *CCVD*. This S parameter is also called the transmission coefficient, and for the above mentioned condition ($V_2^+ = V_1^- = 0\,Volt$). In addition, since the voltage wave at the output of the *CCVD* is a function of its ***DR*** and the voltage wave at the input, given by the equation (30):

$$V_2^- = \frac{V_1^+}{DR} \tag{30}$$

Therefore, the relationship between the S_{21} and the ***DR*** can be written as:

$$DR = \frac{V_1^+}{V_2^-} = \frac{1}{S_{21}} \tag{31}$$

S parameters are often expressed in decibels (dB), being voltage ratios $(S_{ij})_{dB} = 20log(S_{ij})$.

The simulations presented in this chapter are principally based on the evaluation and optimization of these S parameters of the *CCVD*. The advantage of these simulations is that the *CCVD* can be modelled to attain the required characteristics with real dimensions and material properties, before the final mechanical realizations. During the first phases of the modelling, as a starting point, a *CCVD* of a division ratio of 1000:1 (60 dB) was studied, which was later optimized to attain higher division ratio of the divider. All materials in the simulations were chosen to be real materials with their respective losses rather than perfect materials to obtain results, as much as possible, close to the reality. The following sub-sections demonstrates the optimizations of the different elements of the *CCVD*.

2.3.1. Modelling of the main transmission line of impedance Z_0

A cross-section of the main transmission line which is also the high voltage arm of the CCVD is shown in the Fig. 22. Its characteristics are the same as presented in the Table 4.

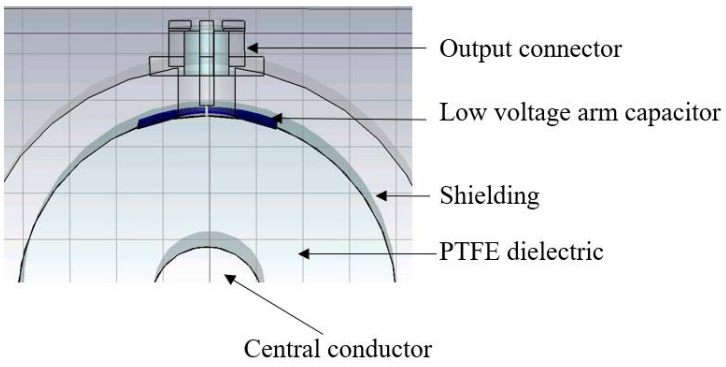

Fig. 22. Cross section of the CCVD showing the main coaxial transmission line of characteristic impedance Z_0

2.3.2. Modelling of the Low voltage arm capacitor

As it is mentioned in the previous section, the shape and size of the *Electrode1* is very critical in the development of the *CCVD*. It is a decisive component for the response of the voltage divider. Different shapes and geometries were studied to obtain a flat transmission coefficient ($\frac{1}{DR}$) as a function of frequency up to a few GHz.

Although, it has been already demonstrated in the section *2.2.2.2*, that the width ***d*** of the umbrella shaped *Electrode1* should be less than 170 mm in order to measure a pulse of rise time 0.5 ns without deformation. Moreover, even a width of 170 mm is way insufficient to cover the whole circumference ($2\pi \cdot 42.55\text{mm}$) of the main transmission line dielectric of radius 42.55 mm. A geometry of the *Electrode1* covering the whole circumference of the main line dielectric, shown in the Fig.23.a), was however simulated to understand the effects it could have on the division ratio and the cut-off frequencies of the divider. This simulation was carried out with the time domain solver using automatic adaptive meshing tool of the CST with three 50 ohm waveguide ports placed at each extremity of the transmission line, as shown in the Fig.23.b), the port1 and port2 are placed at the beginning and the end of the main transmission line whereas the port3 is placed at the output of the Type-N connector with a 50 ohm resistor, the reason for which the transmission coefficient denoted by S_{21} in the equation (29) is represented by S3,1 in the simulations. The Fig.23.c) shows the transmission coefficient (S3,1) as a function of frequency of the *CCVD* where the low voltage arm is constituted of a complete metallic ring (*Electrode1*) placed all over the cylindrical PTFE dielectric of the main transmission line of the divider. A 100 micrometer layer of the dielectric SiO_2 is placed between the *Electrode1* and the metallic shielding. It can be observed that the frequency response is not flat and many oscillations are present due to the propagation effects on the electrode surface, which rends this geometry of the *Electrode1* unsuitable for our use.

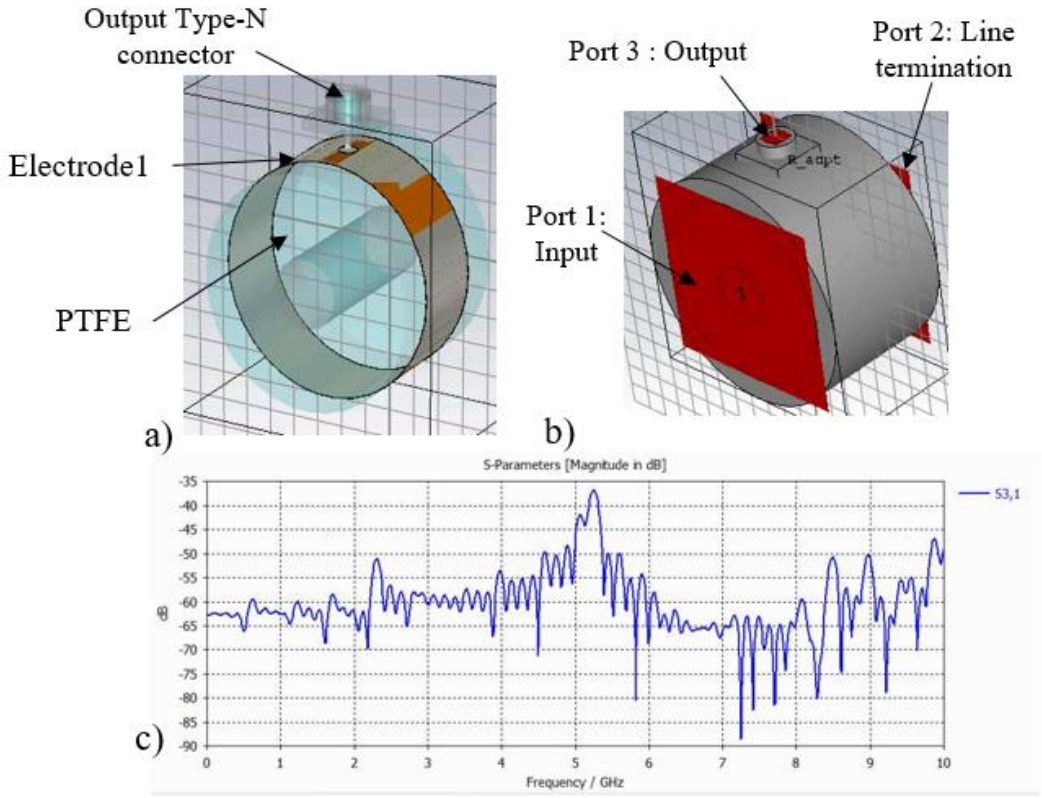

Fig. 23. a) CCVD model with Electrode1 modelled as a complete ring on the main line PTFE dielectric; b) placement of waveguide ports for Time domain simulation; c) transmission coefficient between the input and the output of the CCVD.. Metallic shielding and the main line conductor are hidden for clarity. Brown color spots on the ring are only graphical reflection errors from the software.

These oscillations can be reduced by diminishing the width ***d*** of the Electrode1 from almost 267 mm (the circumference of the PTFE main line dielectric) to an arbitrary 40 mm of width, as shown in the Fig.24.a). The *Electrode1* is modelled, this time, as a small curved rectangular part of the previous ring, represented as a brown rectangular patch. It can be observed form Fig.24.b) that the oscillations are still present but have been largely reduced in numbers and a relatively flat transmission coefficient response is obtained in the concerned bandwidth up to 2 GHz. However, the small oscillations observed in this bandwidth on the transmission coefficient are due to the intrinsic characteristics of the time domain solver which was later rectified by changing the solver to the frequency domain.

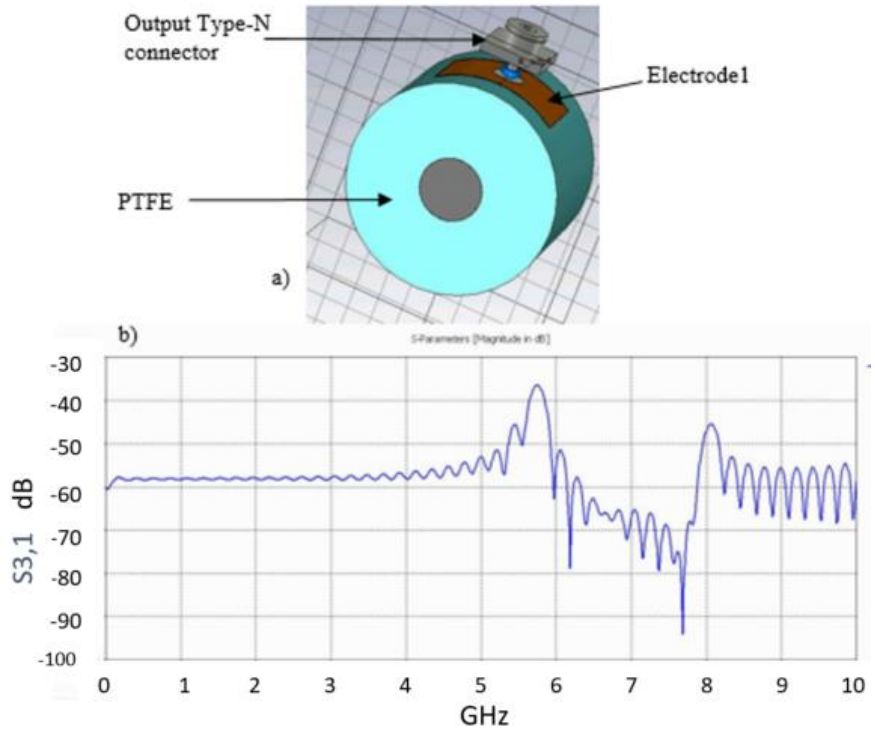

Fig. 24. a) Electrode1 modelled as a curved rectangle; b) transmission coefficient as function of frequency for the modelled CCVD design

Due to the complications related to the practical deposition of a homogeneous thin films on the curved surfaces, the above mentioned umbrella geometry of the *Electrode1* was finally omitted and other preliminary modelling were performed with other shapes of the electrode. However, the most concluding results have been obtained with flat and curved electrode, ***FC electrode***, as presented previously in the Fig. 20. The modelling was further carried out in order to determine the precise dimensions of this electrode. As presented in the Fig.25, a matrix based simulation of the length (***L***) and the width (***d***) of the rectangular electrode were performed up to the frequency of 3 GHz to obtain the best dimensions for flat frequency responses of the divider. From now on, due to the long calculation durations and the oscillations on the transmission coefficient, the solver was changed from the time domain to the frequency domain solver and the other parameters were kept the same as the previous simulations. In this process, each value of the length of the electrode was sweeped with different values of the widths and the same was done for the widths. This was carried out for each ***L*** and ***d*** values ranging from 15 mm to 55 mm and with a step of 10 mm. The flat frequency response obtained up to 3 GHz was observed for the same values of the ***L*** and ***d*** i.e. for the square flat surfaces of the ***FC electrode*** rather than rectangular ones.

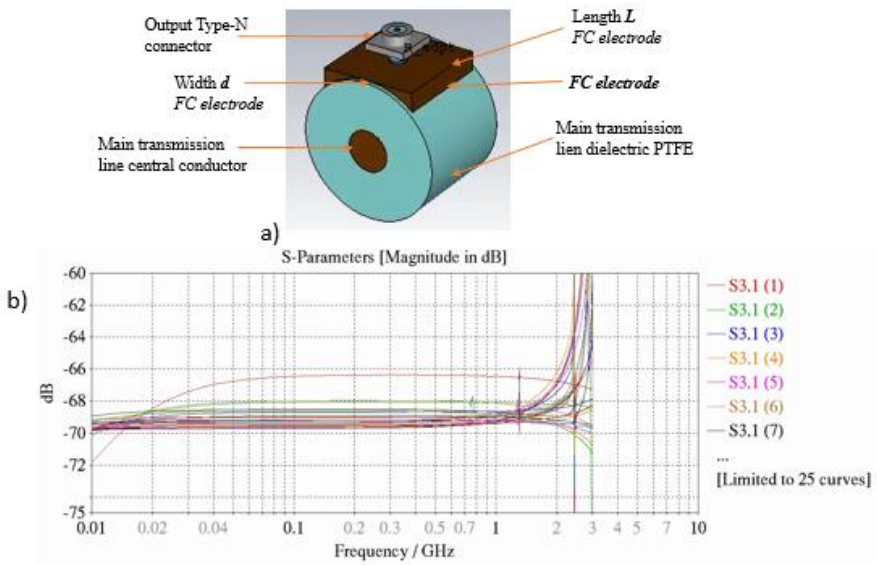

Fig. 25.a) CCVD modelled with a FC electrode, shielding and excitation ports are hidden for clarity purpose of the design, during this simulations the values of the length L and the width d were sweeped with each other; b) transmission coefficient S3,1 of the modelled CCVD in dB.

Consequently, simulations were continued for the values of ***L*** and ***d*** ranging from 26 mm to 34 mm and with a step of 2 mm, to optimize further the best dimensions for the most flat transmission coefficient in the frequency range from few tens of megahertz to few gigahertz for the ***FC electrodes*** and the most satisfactory result was obtained for ***L*** and ***d*** values of 30 mm each. This result is presented in the Fig. 26.

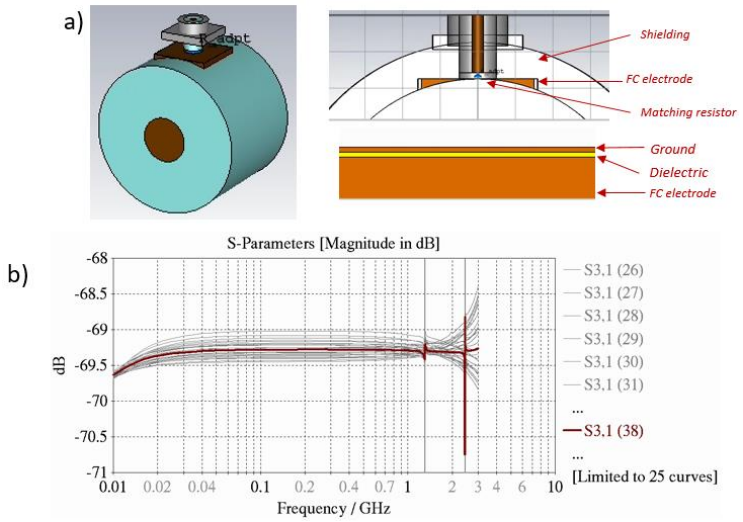

Fig. 26. Square FC electrode; a) geometry of the CCVD with square FC electrode; b) Transmission coefficient of the modelled geometry where the curve S3,1 (38) represent the transmission coefficient of the 30 mm square FC electrode.

Following the simulation presented in the Fig.26, the values of the ***L*** and ***d*** of the ***FC electrode*** was fixed to be 30 mm x 30 mm and the simulations were further carried out, this time to optimize the thickness of the SiO_2 film that could be deposited, taking into account the roughness of the deposition surface of the electrode. Indeed, the presence of peaks on the film deposition surface could puncture the film or could represent spots with a higher intensity of electric field than the rest of the surface, which in return could cause the breakdown of the low voltage arm capacitor of the *CCVD*. However, a small amount of surface roughness is still necessary for a good adherence and the long term stability of the low voltage arm capacitor of the *CCVD*.

The technology used for the deposition of the SiO_2 film can very well deposit films from some hundreds of nanometers to few micrometers, a tradeoff between the surface roughness and the thickness of the deposited film resulted in a film thickness of 5 micrometers, which resulted in the transmission coefficient of *CCVD* to be -85 dB. The final version of the CCVD with these characteristics was simulated and the results are presented in the Fig.27, where a relatively flat transmission coefficient (S3,1) and a linear phase response were found up to the frequencies of at least 2 GHz (***fc***) which confirms the bandwidth of the divider necessary for the distortion free measurements of high voltage pulses in the subnanosecond domain with rise times of $\left(\frac{0.35}{f_c}\right)$ at least few hundreds of picoseconds.

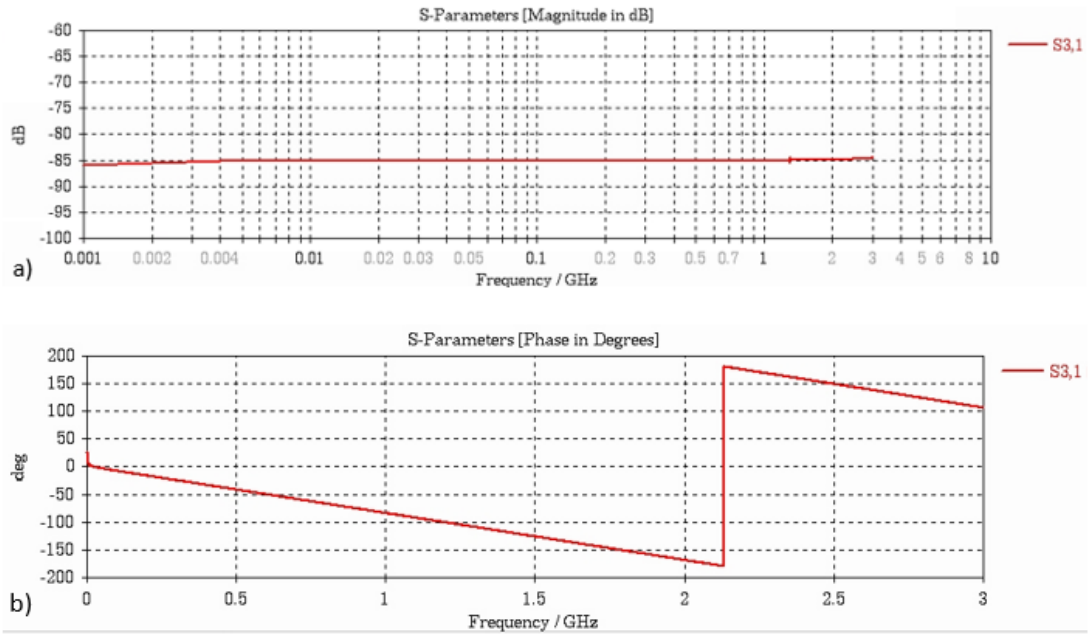

Fig. 27. CCVD with 5 micrometers of SiO2 as the low voltage arm dielectric thickness; a) Transmission coefficient S31; b) Phase of S31

Furthermore, the -85 dB value of the transmission coefficient is equivalent in the linear scale to a division ratio of almost 17000:1, which would allow the use of the *CCVD* to analyze high voltage pulses at least up to 170 kV directly through oscilloscopes. However, to attain the objective of this thesis, a supplementary 20 dB commercial calibrated attenuator at the output of the *CCVD* would be largely sufficient to measure voltage peaks up to 500 kV.

2.4. Realization and testing

Special care was taken during the realization of the *CCVD*, as the frequency response and the attenuation obtained during the modelling process depend highly upon the characteristics of the material used and the precision of the mechanical realizations. Production of the different elements of the CCVD is presented in the following sections.

2.4.1. Construction of the main coaxial transmission line

The main coaxial transmission line of characteristic impedance Z_0 was realized using the elements mentioned in the Table 4, in the paragraph *2.2.1*, to guaranty a 50 **Ω** line impedance. The main line conductor is produced in 99.9% pure copper and the shielding is milled in an aluminum alloy for high electrical conductivity and better resistance to the oxidation and corrosion. The dielectric present between them is made up of *Virgin grade* PTFE for low dielectric constant and high dielectric strength. Furthermore, the PTFE dielectric was characterized in terms of the relative permittivity (ε_1) and the loss tangent ($tan\ \delta$) up to 1 GHz through S-parameters measurements using a vector network analyzer (VNA) by the method described by *Nicolson and Ross* [96]. For these measurements, a cylindrical sample of length ***d***=5mm of the PTFE is placed in a coaxial waveguide of characteristic impedance Z0. The measurement is performed after calibrating the VNA using a "Thru Reflect Line" method and the S-parameters were measured. This waveguide is presented in the Fig.28, where ε_1 and μ_1 represent the relative permittivity and relative permeability of the PTFE sample respectively and *Z* represents the new characteristic impedance of the coaxial waveguide.

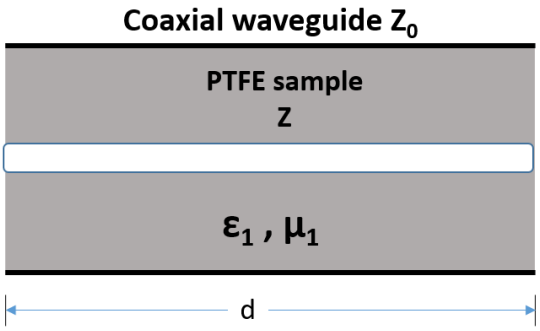

Fig. 28. Coaxial waveguide with a PTFE sample for S parameter measurements

Through the measured S-parameters (S_{11} and S_{21}), the relative permittivity of the PTFE is obtained by the equation (32) [96]:

$$\varepsilon_1 = j\left(\frac{1-R}{1+R}\right)\left(\frac{c_0}{\omega d} \times lnT\right) \tag{32}$$

where:

$$R = \frac{{S_{11}}^2 - {S_{21}}^2 + 1}{2S_{11}} \pm \sqrt{\frac{{S_{11}}^2 - {S_{21}}^2 + 1}{4{S_{11}}^2} + 1} \tag{33}$$

and

$$T = \frac{1 - (S_{21} + S_{11})R}{(S_{21} + S_{11}) - R} \tag{34}$$

The measured values of ε_1 and *tan* δ up to 1 GHz for the PTFE sample is presented in the Fig.29 and their average values were found to be 2.03 ± 0.07 and 0.003 ± 0.006 respectively in the concerned bandwidth from 10 MHz to 1 GHz. The measurement uncertainties are presented with a coverage factor of k=2. The measurement values of ε_1 and *tan* δ confirmed the values used for the PTFE in the simulations of the CCVD within the measurement uncertainty limits.

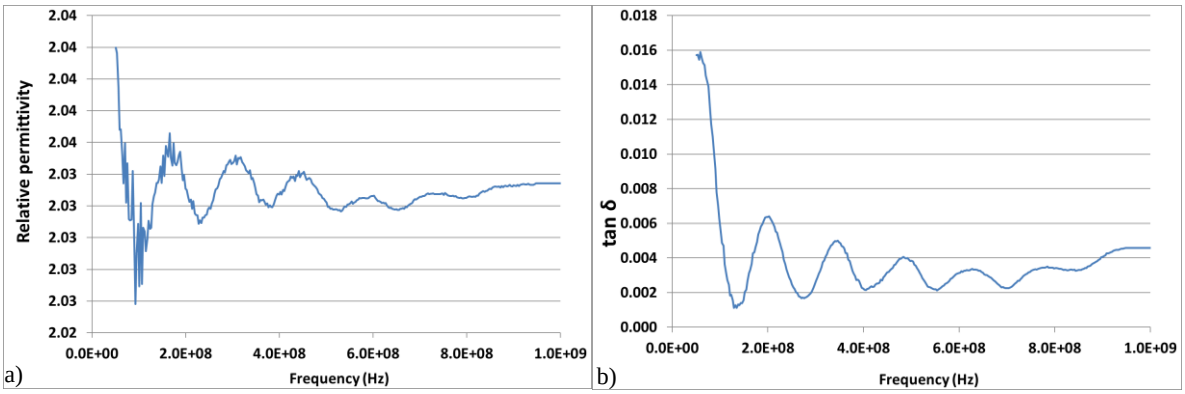

Fig. 29. Measured values of the properties of the main line dielectric PTFE up to 1 GHz; a) relative permittivity ε_1; b) loss tangent tan δ

The mechanical production of the portion of the main transmission line where the *CCVD* is placed is realized with male and female high voltage connectors developed in this thesis work. These connectors and their geometry are presented in the next chapter. The main elements produced for the integration of the *CCVD* to the main transmission line are presented in the Fig.30.

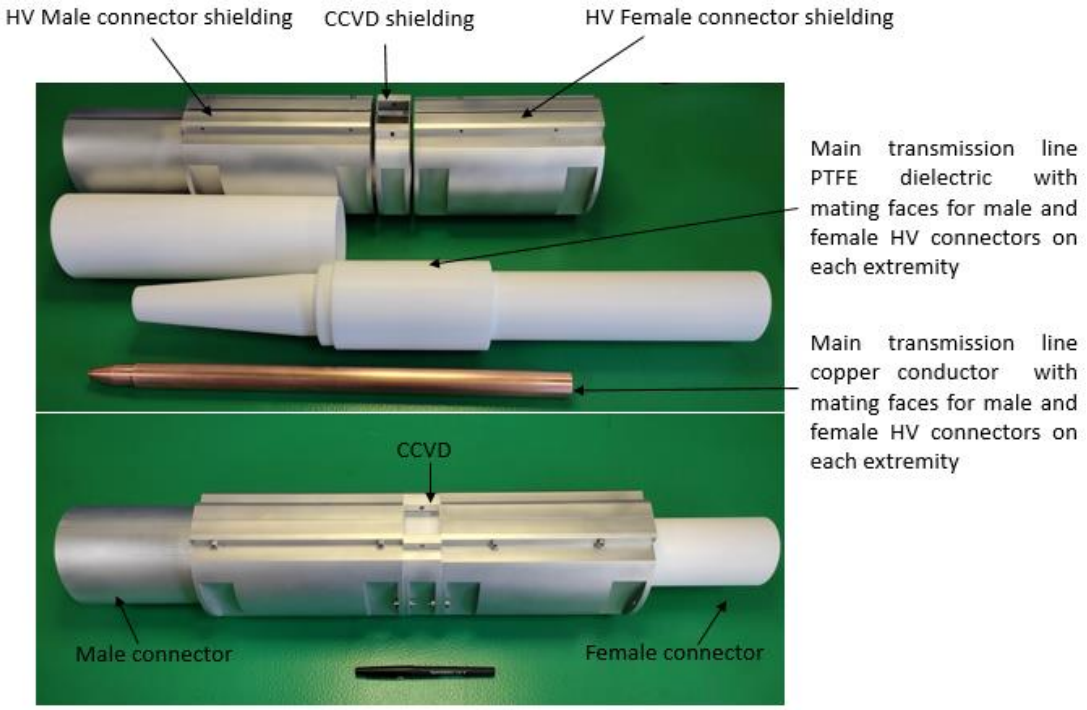

Fig. 30. Different mounting elements constituting the CCVD

2.4.2. Fabrication of the low voltage arm

2.4.2.1 Conception of FC electrode

As it is mentioned in the sections *2.2.2.2* and further in *2.3.2*, the respect of the geometry and the dimensions of the *FC electrode* are very necessary for the realization and performance of the low voltage arm capacitor, which itself is the most deciding part in the performance of the *CCVD*. For the fabrication, the mechanical files were extracted from the simulated geometry of the *CCVD* from the CST software and the *FC electrode* was fabricated through an automated Electrical Discharge Machining (EDM) procedure, in order to respect the exact dimensions of this electrode. After the fabrication, these electrodes were polished to reduce the surface roughness below 1 micrometer for a good adherence of the deposited SiO2 film and to avoid the breakdown of the low voltage arm capacitor of the *CCVD*.

2.4.2.2. Deposition of the dielectric and first tests performed

The dielectric SiO_2 chosen for the low voltage arm capacitor, for the reasons mentioned in the paragraph *2.2.2.1*, is deposited by reactive *Magnetron Sputtering* techniques using a double ring magnetron. In this type of magnetron two concentric discharges allow achieving good thickness uniformity across up to 200mm substrate diameter. Sputtering was done from doped Si targets using a mixture of oxygen and argon gas. In addition, pulse powering at 50 kHz was applied to attain a deposition rate of 3 nm/sec. The advantage of this technique lies in the fact that the controlled regular film thicknesses can be deposited on the substrates with dielectric breakdown strengths as high as 5.6 MV/cm, which gave margins to decrease the film thickness from initially 100 micrometers to 5 micrometers and increased the capacitance value of the low voltage arm of the *CCVD*.

For the preliminary tests of the dielectric strength, a film deposition of 10 µm of the SiO_2 film was performed on the flat surface of a *FC electrode*. The deposited film thickness was measured through a reference substrate on which the deposition was performed in the same chamber and at the same time as of the electrode. The film thickness on the reference substrate it was measured to be 11 µm ± 4 µm. Further to deposition of this sample, a metallization of the surface of the dielectric was conducted in order to form the *Electrode2* for the final production of the low voltage arm capacitor.

Posterior to this process, the realized capacitor was separated into two zones and each zone was tested for isolation properties as presented in the Fig.31. Indeed, for the measurements of 500 kV pulses, the potential difference at the low voltage arm capacitor would be around 100 V, which is calculated from the equation (16) with a ***DR*** of 10000:1, corresponding to the *CCVD* with a 10µm of SiO_2 film as the low voltage arm dielectric. Therefore, the voltage withstand capability was fixed to minimum value of 100 V. These isolation testing was performed by applying an increasing DC voltage to the developed capacitor in steps of 5 volts and the leakage current was measured simultaneously. The very first test was performed to attain the required target isolation of 100 volts on both the zones and then they were further tested to evaluate their breakdown voltage values. It was observed that both the parts attained the breakdown voltage levels up to around 450 volts. This procedure is presented in the Fig.31.

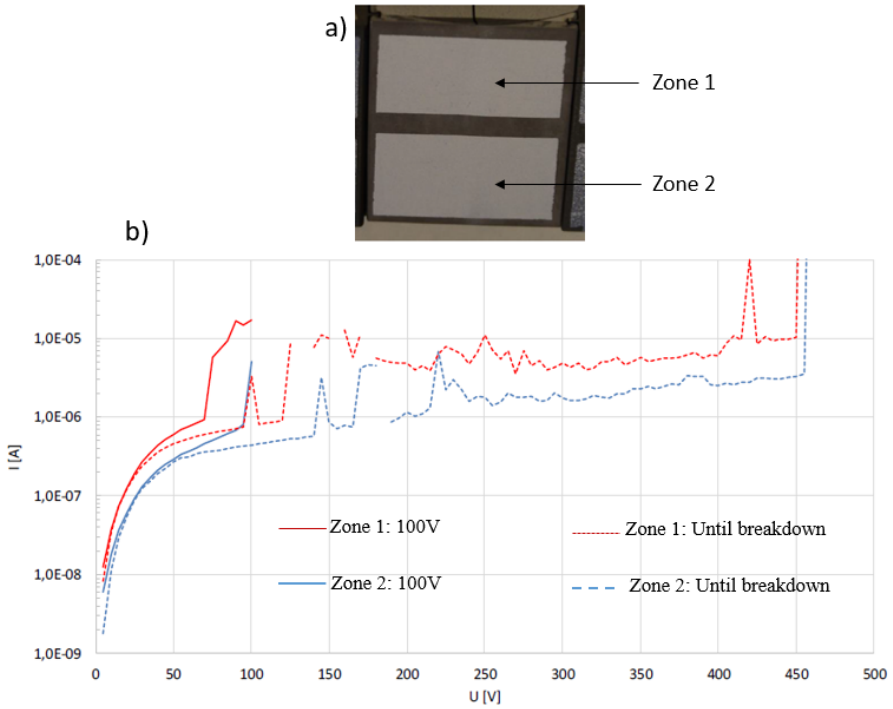

Fig. 31. Isolation testing of the developed low voltage arm capacitor of the CCVD; a) realized sample separated into two zones; b) measurement of leakage currents for both zones. Continuous lines represent the results obtained for target voltage levels of 100 V testing and the dotted lines represent the testing procedure up to the breakdown voltage of both zones. Discontinuities present in the curves are due to the change of measuring range of the measurement instrument during which the measurements were not possible.

Two batches of the low voltage arm capacitors were later fabricated, each with different film deposition thicknesses, one batch with 5 µm SiO_2 film thickness and the

other batch with 10 µm of thickness. All the capacitors were tested for the isolation voltage levels up to at least 100 V. A 50 Ω matching resistor was mounted on each capacitor and they were further tested through a *LCR-meter* to measure the capacitance values for AC voltage of 1 V at a frequency of 800 kHz; these applied levels are the maximum capabilities of the *LCR-meter* used on the tested capacitor. This measurement setup is presented in the Fig.32. Capacitors with 5 µm ± 1 µm of film thickness showed capacitance values of 5.1 nF ± 0.3 nF and those with 10 µm ± 1 µm of the film thickness showed values of 2.4 nF ± 0.3 nF, and the calculated capacitance values through the equation (18) were 4.9 nF and 2.2 nF respectively.

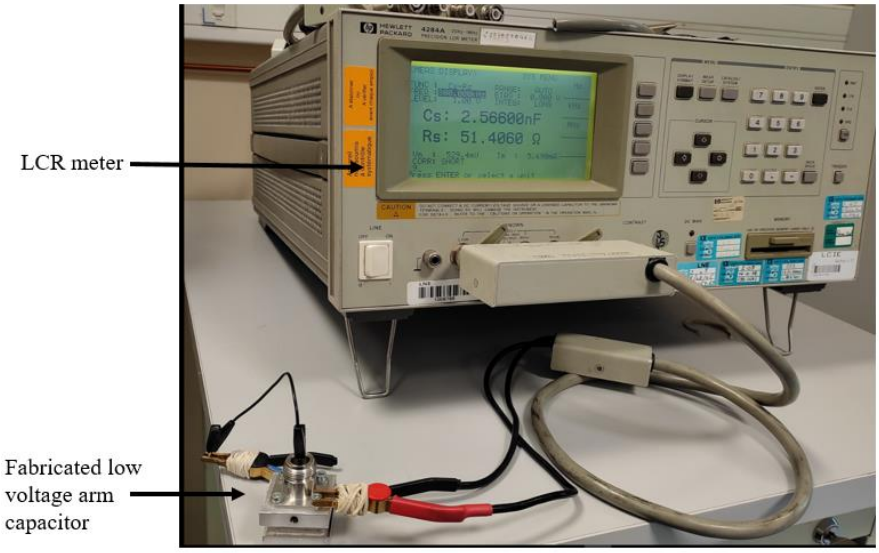

Fig. 32. Measurement setup for the capacitance value of the low voltage arm capacitor at 1 V and 800 kHz. The low voltage arm capacitor is fabricated with an integrated 50 Ω matching resistor

The calculated and the measured values of the low voltage arm capacitance of the CCVD are in very good agreement with each other, within the measurement uncertainty limits. The fabricated low voltage arm capacitor is then integrated in the cavity intended for the CCVD presented in the Fig.30, thus, completing the realization of the CCVD.

2.5. Conclusion

In this chapter, a calculable capacitive voltage divider *CCVD* based on the transmission line principle is developed which is destined to measure high voltage pulses of voltage amplitudes up to 500 kV in the nanosecond and subnanosecond domain. A thorough theoretical analysis for the conception of this divider is presented and the factors affecting the division ratio and the frequency response is discussed. A new geometry of the intermediate electrode, *FC electrode*, is also presented which is one of the most decisive element of the *CCVD*. The desired performances in terms of a high division ratio and a flat frequency response up to at least 2 GHz of the *CCVD* is confirmed with the CST simulations in which real geometries and real properties of the intended materials for the fabrication are used. A thin film of 5 µm of SiO_2, constituting the dielectric of the low voltage arm capacitor of the divider, is successfully deposited and tested to withstand DC voltage at least up to 100 V. Finally, the measured values of the fabricated low voltage arm capacitor is found to be in very good agreement with the calculated values.

Calculations demonstrate that the *CCVD* possess a flat transmission coefficient and linear phase responses as a function of frequency up to at least 2 GHz, which are the necessary characteristics for the analysis of different parameters of the concerned high voltage pulses, without deformation, through a calibrated oscilloscope. These characteristics of the *CCVD* will be confirmed experimentally in the chapter 4 through different measurement methods, after the conception of other important elements of the HPPNS measurement system, such as, a 50 Ω load and high voltage male and female connectors which are presented in the next chapter.

CHAPTER

3

Development and designing process of other components of the measurement system, such as, a 50 Ω coaxial termination load, high voltage male and female connectors and 50 Ω characteristic impedance transition cones, are described in this chapter. A detailed analysis for the development of the termination load is presented in order to maintain the impedance value of 50 Ω for accurate and precise measurements of the high voltage waveforms with negligible amount of wave reflections. Furthermore, to facilitate the connection of different components together and also the connection of the complete measurement system to high voltage waveform generators, male and female connectors capable of withstanding voltage peaks up to 500 kV are also presented. Finally, modelled and developed transition cones with Type-N output connectors for high frequency low power measurements are described.

Chapter 3: Development of high voltage 50 Ω load and connectors

In a measurement system destined to measure high voltage fast transient pulses, after a precision voltage divider *CCVD* described in the previous chapter, an important component is a load device. It serves two major and vital purposes from the point of view of the efficient functioning of the measurement system, the first being the matched termination for the transmission line with its characteristic impedance and the second one consists of the dissipation of the energy present in the incident pulse. Several measurements systems based on a voltage divider and a matched load have been published [22], [97]–[101]. However, the termination load device used in these setups does not seem to have a broadband frequency performance enough to measure pulses

with rise times in the range of few hundreds of picoseconds with amplitudes levels up to 500 kV.

Various types of resistors are used to form the load depending upon the concerned frequency domain, the voltage amplitude levels and the required matching accuracy. For example, the wire wound resistors are only efficient in the frequency domain up to only few tens of megahertz because of their residual inductance and capacitance. Moreover, for higher frequencies, the skin effect also becomes more and more consequent, rendering these resistors, due to all of these effects, highly frequency dependent. As far as only the skin effect is concerned, it could be overcome by using ceramic resistors with a thin coating of resistive material. To minimize the skin effect, the thickness of the resistive film can be kept low so that it becomes at most comparable to the skin depth. However, the residual reactance alter their performance and limit their use only up to few megahertz. For higher frequencies, a coaxial structure of the load is the best solution [102], [103]. This structure mainly serves two purposes; it eliminates not only the parasitic capacitance which is formed by the electric field extending radially along the length of the resistor in the absence of a coaxial structure, but also reduces electromagnetic interferences. These aspects concerning the load become more crucial when high voltage pulses of amplitude levels up to 500 kV in the domain of sub-nanosecond are concerned. Consequently, for the high voltage ultrawideband pulse termination load, a wide frequency bandwidth and high insulation properties should be achieved at the same time.

In this thesis work a 50 Ω load based on a special coaxial structure with a cylindrical resistor is developed, which shows a very good matching performances up to several gigahertz. This coaxial load is discussed in the following subsections.

3.1. Theoretical analysis of a reflection free load

In the domains where high power as well as high frequency is concerned, such is the case in this thesis work, the transmission line terminations should be built in such a way that all the incoming energy from the incident pulse is absorbed as much as possible, which would result in a minimum reflection of the incident pulse. For this to happen, as mentioned before, the transmission line should end in a matched load of impedance equal to the line characteristic impedance. A situation where the load is not matched to the characteristic impedance of the transmission line, could lead to the misunderstanding of the attenuated pulse obtained through the measurement system because of the reflections caused by the mismatching of impedances. Reflected pulses could be

superposed to the measured pulse and in some cases, it becomes difficult to discriminate from the real pulse and the reflected ones. The reflections are quantified by scattering reflection coefficient (S_{11}) and can also be calculated in terms of impedances, by a well-known, reflection coefficient equation, shown in the equation (35) for a uniform coaxial transmission line with characteristic impedance Z_0, terminated by a load of impedance Z_L:

$$S_{11} = \frac{Z_L - Z_0}{Z_L + Z_0} \tag{35}$$

It can be easily concluded from the equation (35) that for the case where the transmission line terminates by the impedance equal to its characteristic impedance, i.e. $Z_L = Z_0$, the refection coefficient value will be zero and the incident pulse can be measured accurately.

Furthermore, to obtain a reflection free performance of the load, a rule of thumb is, the characteristic impedance of the coaxial line enclosing the resistor at any cross section must be equal to the load resistance beyond that cross section. For example, as demonstrated by Harris [104], for a cylindrical film resistor of resistance ***R*** divided into four equal sections, with a short piece of lossless coaxial line interposed between each pair of sections, represented in the Fig.33, at the cross section ***A*** the resistance seen to the right is ***R*** and the characteristic impedance of the coaxial line leading-in to ***A*** is made equal to ***R***.

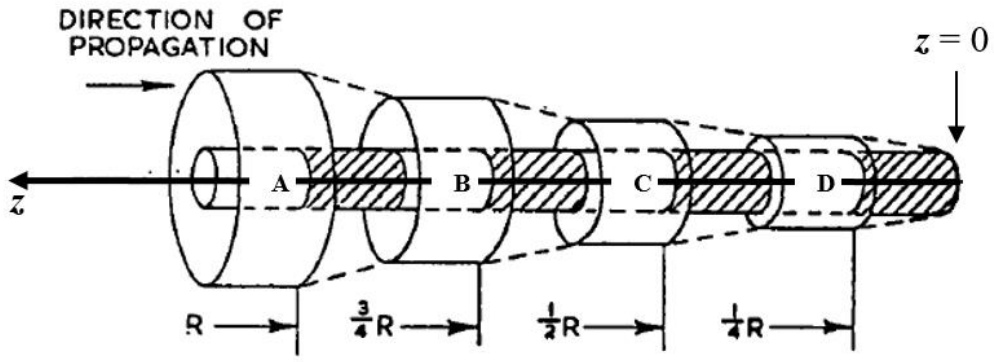

Fig. 33. Cylindrical film resistor divided into four equal parts, with interposed sections of lossless coaxial line[104]

In the same way, at the cross section ***B*** the resistance seen to the right is $\frac{3}{4}\boldsymbol{R}$ and the characteristic impedance of the coaxial line leading into ***B*** is made equal to $\frac{3}{4}\boldsymbol{R}$. Similarly at the cross sections ***C*** and ***D***, the characteristic impedances of the respective leading-in coaxial line are made equal to $\frac{1}{2}\boldsymbol{R}$ and $\frac{1}{4}\boldsymbol{R}$. If the lengths of these intersection lossless lines be made infinitesimal, the profile of the outer shielding conductor is then determined at four cross sections ***A***, ***B***, ***C*** and ***D***. Furthermore, by increasing the number of sections into which the resistor is divided, a continuous profile of the outer shielding conductor can be determined.

Another important property of the load is to guarantee a sufficient high voltage insulation. Indeed, the inevitable presence of the thin films or pockets of air at the resistor-dielectric interface and even in the tubular cavity of the resistor could reduce drastically the dielectric strength of the whole load and could eventually cause flashovers between the metallic contacts of the resistor. For this, relatively long resistors are used as the resistive element constituting the coaxial load. Due to their size, these resistors at higher frequencies, in the case of rapid pulses, lose their discrete properties and their lengths are no longer negligible as compared to the wavelength of the travelling pulses. Considering R_0 as the total resistance and $R(z)$ being the remaining ohmic resistance at a distance z from the short-circuited end (represented by z=0 in the Fig.33) of a resistor of total length l_r, then $R(z)$ can be written as:

$$R(z) = z\,\frac{R_0}{l_r} \tag{36}$$

Therefore, for reflection free transmission as stated before, the value of $R(z)$ must be equal to the characteristic impedance of the coaxial line at the point z, which is given by the equation (24) in the previous chapter. This leads from the equations (24) and (36) to the equality:

$$z\,\frac{R_0}{l_r} = \frac{1}{2\pi}\sqrt{\frac{\mu_0\mu_1}{\varepsilon_0\varepsilon_1}}\ln\frac{c}{a} \tag{37}$$

where,

μ_0: permeability of free space ($\mu_0 = 1.25663706212\times10^{-6}$ H/m)

μ_1: relative permeability of the dielectric of the main transmission line

ε_0: permittivity of free space ($\varepsilon_0 = 8.8541878128\times10^{-12}$ F/m)

ε_1: relative permittivity of the dielectric of the main transmission line

c : inner radius of the metallic shielding of the transmission line

a : is the outer radius of the cylindrical tubular resistor.

From equation (37), the required profile of the inner radius $\boldsymbol{c}$ of the metallic shielding can be calculated as:

$$c = a \,.\, e^{\frac{2\pi z R_0}{Z_w L}} \tag{38}$$

where $Z_w = \sqrt{\frac{\mu_0 \mu_1}{\varepsilon_0 \varepsilon_1}}$

The equation (38) results in an exponential profile for the shielding, shown in the Fig.34.

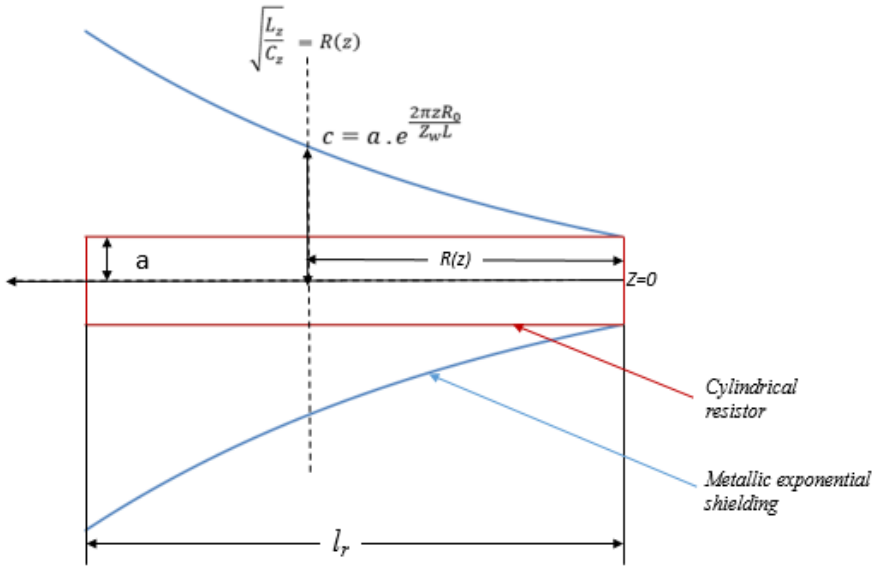

Fig. 34. Exponentially tapered profile of the inner radius of the shielding as defined by the equation (38). The vertical hatched line shows an example of the reflection free condition, where the characteristic impedance of the line is equal to the remaining ohmic resistance R(z) at this longitudinal cross section.

There are further improvements in the shielding conductor profile, which has been published in the literature [105], [106] named tractorial terminations based on a tractrix profile, which is a steeper form of the exponential profile. However, for the resistive loads, with a long resistive element for better insulation from flashovers, the difference in the results announced are not that overwhelming. In addition, if the exponential profile for the shielding conductor is carefully realized mechanically, reflection coefficients (S_{11}) as low as -30 dB can be achieved. Having this as objective, a resistive 50 Ω load is realized in this thesis and the realization steps are described in the following sections.

3.2. Choice of the 50 Ω resistor

For the conception of the 50 Ω termination load, the choice of an appropriate resistor constituting the main conductor of the coaxial load is critical. It should possess following properties:

I. A low-inductive resistor with a DC-resistance value of 50 Ω.
II. Sufficient separation between the metallic contacts of the resistor to avoid flashovers, as demonstrated in the Fig.35. These flashovers could be transmitted to the measuring instruments present in the measurement circuit and resulting in their breakdown.

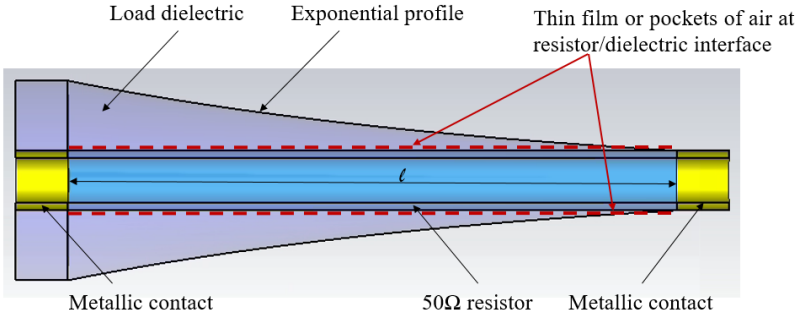

Fig. 35. Cross section of the exponential load with probable presence of air between the resistor and dielectric interface

III. Bulk resistor for better energy dissipation. The load, apart from its principal role of the matched termination of the transmission line, is also destined for the dissipation of the energy present in the incident pulse. Bulk resistors facilitates this process.

IV. High specific heat of the resistive material used to avoid excess heating of the load. Materials with low specific heat constituting the resistor could rise rapidly in temperature and cause extra heating of the load. This heating could therefore change the value of the resistor and the 50 Ω value of the load resistor will not be assured.

Different resistors in search of above-mentioned properties were tested and finally a tubular low-inductance bulk ceramic resistor with embedded metallic conducting particles was chosen. Unlike a film resistor, which is typically comprised of a "thin" or "thick" conductive film deposited or printed onto a non-conductive, insulating flat or tubular, usually ceramic substrate, the chosen ceramic composition resistors consists of a matrix of conductive metallic particles, that are mixed with ceramic materials, formed into a desired shape and then fired at very high temperatures. Furthermore, the bulk construction advantageously produces an inherently low-inductive resistor and it allows energy and power to be uniformly distributed throughout the entire ceramic body which helps to withstand high operating temperatures with, at the same time, high power dissipation. A bulk ceramic resistor is presented in the Fig.36.

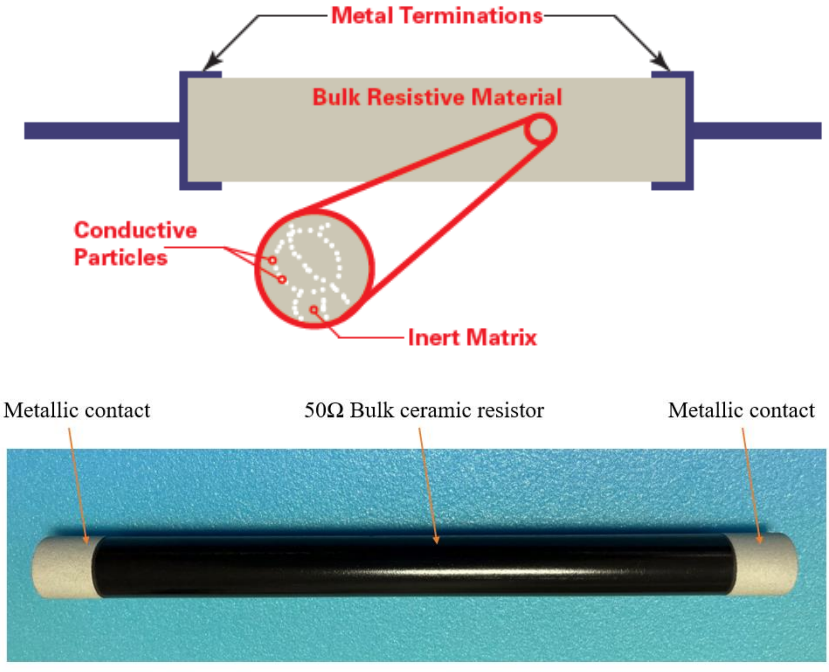

Fig. 36. a) Fabrication of bulk ceramic resistor with metallic conducting particle; [image courtesy OHMITE]; b) 50 Ω bulk ceramic resistor

A 30 cm long 50 Ω (50 Ω ± 10%) nominal value resistor based on this manufacturing process is chosen and presented in the Fig.36.b. The separation between the metallic terminations is 26 cm, which is more than sufficient to avoid flashovers between them due to the presence of air. Indeed, to avoid flashovers in the air, which has generally a dielectric breakdown strength of around 30 kV/cm, a minimum distance of at least 17 cm is needed for pluses of peak voltages of 500 kV. Moreover, the diameter of the resistor was chosen to be the same as the inner conductor of the main coaxial transmission line, which helps avoiding the diameter adjustments to guaranty the 50 Ω value of the line characteristic impedance.

A ceramic bulk resistor from the same family of DC resistance value of 51.5 Ω was tested with applications of different pulses to evaluate the deviation of its resistance value from the DC value, through the measurement setup presented in the Fig.37.a). Pulses of voltage amplitudes varying from 3 kV to 12 kV with a rise time of 1.2 µs and a duration of 50 µs were generated from the pulse generator and were applied to the ceramic resistor. The current pulse converted to a voltage pulse by the current sensor and the voltage pulse at the extremities of the resistor were measured simultaneously on an oscilloscope. The output of the current sensor was further converted to obtain the peak current value I_{peak} and through the voltage peak value measured by the voltage sensor V_{peak}, the value of the resistance (V_{peak}/ I_{peak}) was calculated. These resistance values are presented in the Fig.37.b), and it can be noticed that the measured values of the resistance are in agreement with the DC value within the absolute measurement uncertainty of 1 Ω, with a coverage factor of 2. In addition, to evaluate the heating effect of the resistor, 1000 continuous pulses at an interval of 1s with pulses of voltage amplitude of 12 kV of rise time 1.2 µs and a duration of 50 µs were applied to the ceramic resistor and the resistance values were calculated in the same way as mentioned in the previous paragraph. These results are presented in the Fig.37.c), and demonstrate that the measured values are still in good agreement with the DC value of the resistance, within the same measurement uncertainty value as mentioned before for the same measurement setup.

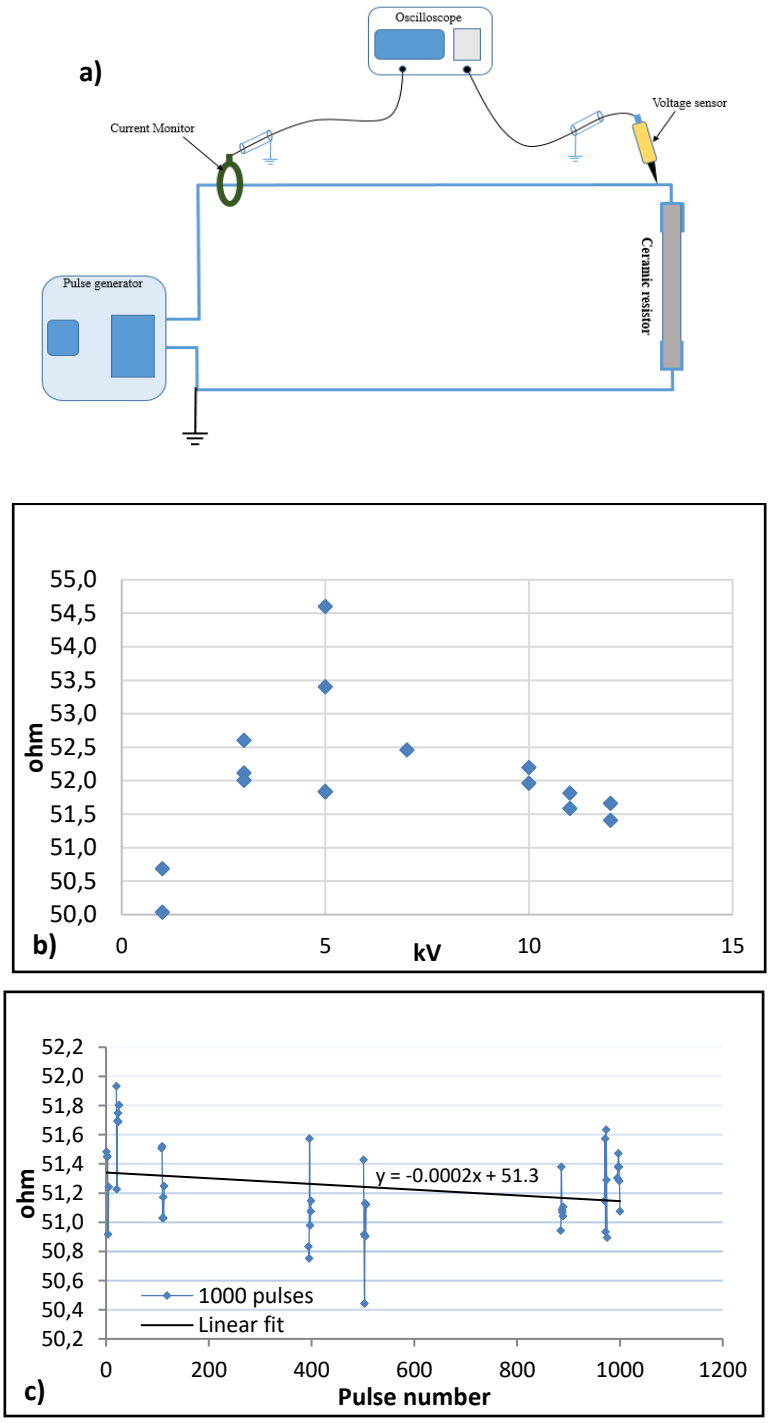

Fig. 37. a) Measurement setup for the testing of 51.5 Ω resistor; b) resistance value measured by the applications of 1.2μs/50μs pulses of 3 kV to 12 kV levels of voltage amplitudes; c) resistance values measured at different time intervals during the application of 1000 pulses

Furthermore, the temperature rise of the same resistor during the application of a pulse was also calculated to evaluate the deviation of the resistance value with respect to the temperature coefficient of the resistor. The temperature coefficient announced by the constructor is between +0.2 %/°C and -0.08 %/°C. The local rise in temperature ΔT of the resistor was calculated with the help of the equation (39).

$$\Delta T = \frac{E}{m.C_P} \tag{39}$$

Where:

$\boldsymbol{E}$ = total energy dissipated in the resistor

$\boldsymbol{m}$ = mass of the resistor

$\boldsymbol{C_P}$ = specific heat of the resistor

From the dimensions and the density (ρ) of the resistor, the mass $\boldsymbol{m}$ was calculated to be 163.3 g and the specific heat announced by the constructor is 0.25 cal/(g.°C) which can be written as 1.046 J/(g.°C) and the energy dissipated in the resistor at a given time $\boldsymbol{t}$ is calculated by the following formula:

$$E = \int_0^t \frac{U(t)^2}{R}\, dt \tag{40}$$

where R is the load resistance value of 50 Ω and $U(t)$ represents the waveform of the input pulse. As an example, a double exponential pulse is considered which is defined by the following equation:

$$U(t) = A.U(e^{-\alpha t} - e^{-\beta t}) \tag{41}$$

Using the equation (40), a 500 kV pulse was modelled with a rise time of around 5 ns and full-width at half maximum (FWHM) value of almost 100 ns, that is also called the pulse duration. These characteristics of this pulse are the upper limits of the incident pulse in terms of peak voltages and temporal parameters, which is intended to be measured in this project. The parameters used to model this pulse are A = 1.0372, U = 500 kV, $\alpha = 5\ \mu s^{-1}$ and $\beta = 1000\ \mu s^{-1}$ and the pulse waveform obtained through (41) is presented in the Fig.38.

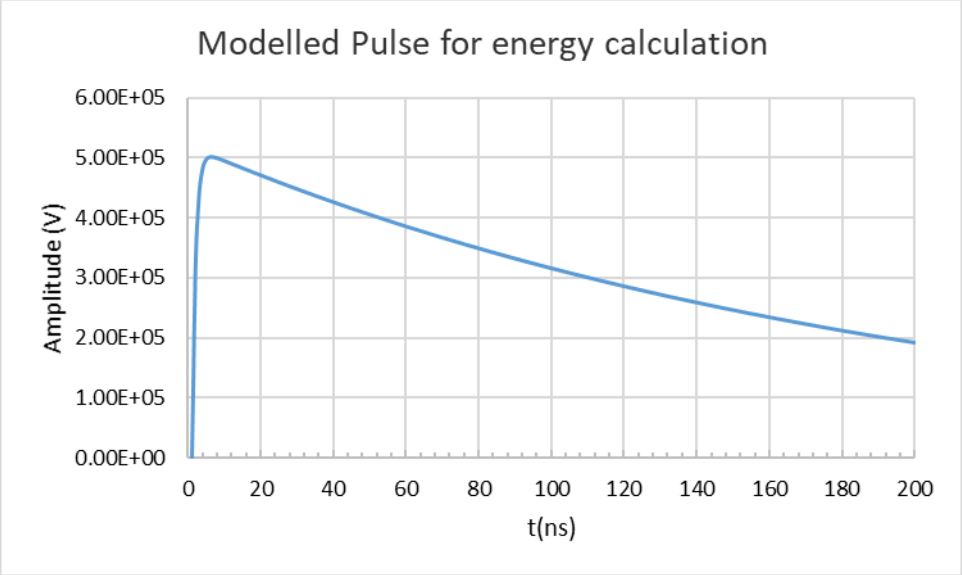

Fig. 38. Modelled 500 kV double exponential nanosecond pulse for energy calculations

From the equations (40) and (41), the total pulse energy at a given time ***t*** is calculated by the following equation:

$$E = \frac{A^2(U.10^3)^2}{R}\left[\left(\frac{-1}{2\alpha}\right).\left(e^{-2\alpha t}-1\right)+\left(\frac{-1}{2\beta}\right).\left(e^{-2\beta t}-1\right)+\left(\frac{2}{\alpha+\beta}\right).\left(e^{-(\alpha+\beta)t}-1\right)\right] \quad (42)$$

Using the above equation, the value of the total energy *E* for the pulse presented in the Fig.38 for FWHM of ***t***=100 ns is around 330 J, which represents a 2°C rise in the resistor temperature calculated through the equation (39). This rise in temperature, for a 50 Ω resistor, represents a variation from 0.2 Ω to -0.08 Ω using the temperature coefficient values announced by the constructor. These relatively small variations in the value of the resistor considered can be neglected and similar resistors from the same constructor, based on the same technology and family, of 50 Ω values can be very well used in the conception of the 50 Ω load of the HPPNS system. The designing process of this load is described in the following section.

3.3. Electromagnetic modelling of the 50 Ω load

The *CST Microwave Studio*® was used to perform electromagnetic modelling and the optimization of the 50 Ω load based on the exponential profile of the shielding conductor given by the equation (38). During the first phases of the conception, both normal cylindrical and exponential coaxial profiles for the same resistor were modelled to evaluate the differences between their responses. A 50 Ω tubular ceramic resistor of 30 cm of length was modelled as the central conductor with an outer radius of 12.7 mm. This resistor was modelled in a normal cylindrical coaxial line with an inner radius of the shielding aluminum conductor of 42.55 mm, calculated to attain a 50 Ω characteristic impedance all along the resistor length with PTFE as dielectric. Later, the exponential profile was modelled for the shielding conductor. The dielectric present between the resistor and the metallic shielding, for both geometries, was chosen to be the same as the *CCVD*, the PTFE, for once again the same reasons, its low permittivity and low losses.

The geometry and a fast rising pulse response at the waveguide port of the normal cylindrical coaxial 50 Ω load is presented in the Fig.39.a. It can be observed from the Fig.39.b that the waveguide port, placed at the beginning of the load input, measures a great amount of the incident signal which reflected back to it due to mismatching of the impedance.

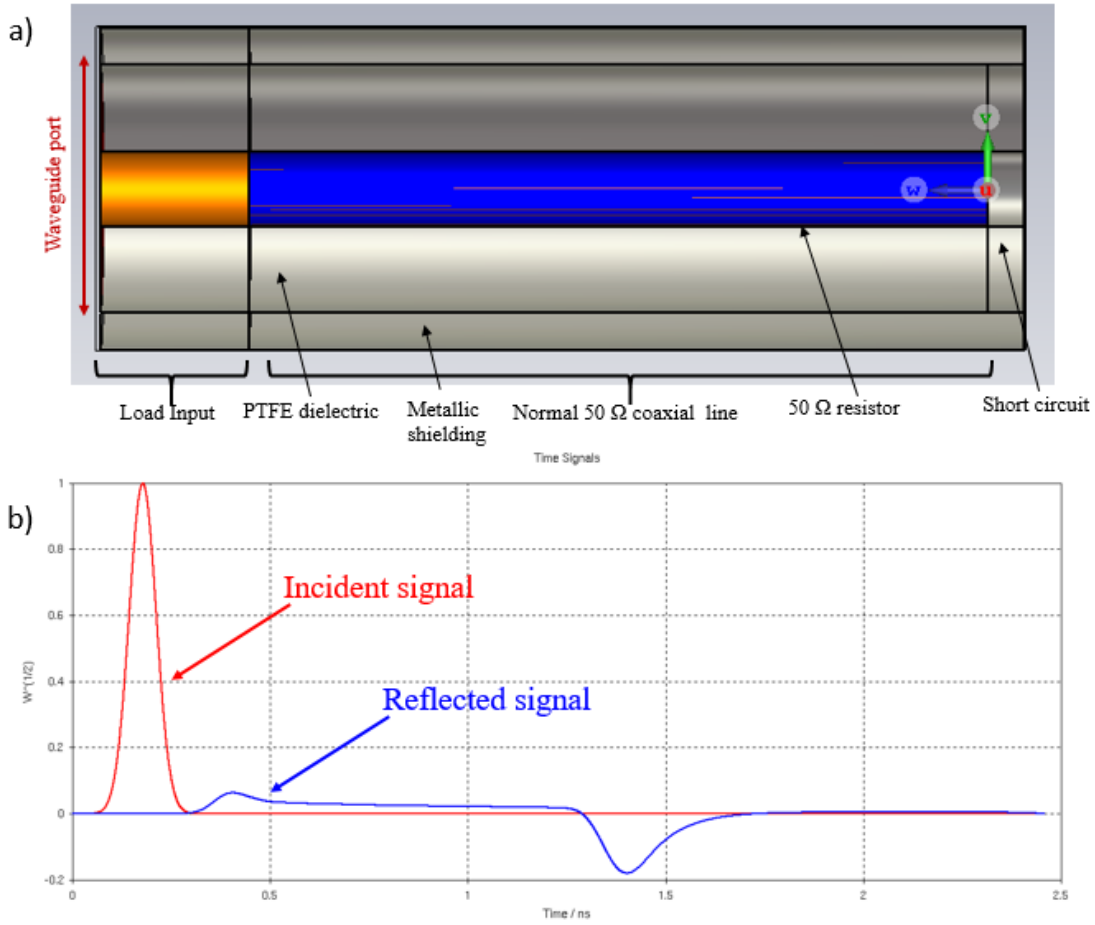

Fig. 39. Normal cylindrical high voltage 50 Ω coaxial load; a) Elements constituting the load; b) Incident and reflected signals of the modelled geometry.

Furthermore, in the Fig.40.a, a maximum reflection coefficient (S11) of -5 dB is obtained for this geometry and the Time-Domain Reflectometry (TDR)[3] analysis, represented in the Fig.40.b, shows variations up to 100 Ω from the nominal 50 Ω value of the resistor.

[3] A TDR measures reflections along a line and locates mismatching of impedances. It evaluates the impedance profile along a TEM or similar structure based on the reflected time signals at a waveguide port and is calculated from the time integrals of the input pulse and the reflected signal as presented in the Fig.39.b:

$Z(t) = Z_0 \frac{\int_0^{+\infty} I(t)dt + \int_0^t O(t)dt}{\int_0^{+\infty} I(t)dt - \int_0^t O(t)dt}$ where *Z(t)* is the TDR impedance, Z_0 is the waveguide port impedance (50Ω), *I(t)* is the input signal and *O(t)* is the reflection signal. https://space.mit.edu/RADIO/CST_online

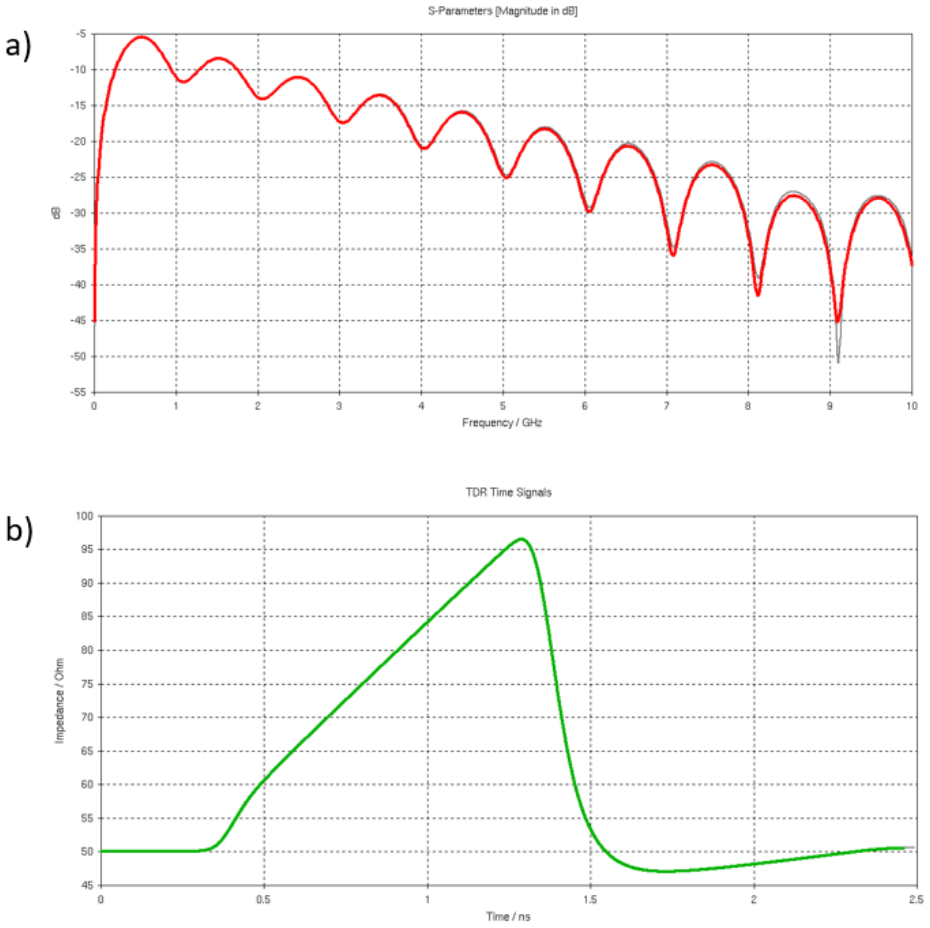

Fig. 40. Normal cylindrical coaxial50 Ω load; a) Reflection coefficient S11; b) TDR impedance

In the light of these results, it is evident that this geometry for the coaxial load is inadequate for the 50 Ω termination of the transmission line. It will result in large amounts of reflections of the incident pulse that will deform the measured signal, hindering the measurement of the real incident pulse.

The next geometry of the 50 Ω load which is modelled is the exponential geometry. The same elements constituting the load as mentioned for the normal load, such as, the same 30 cm long 50 Ω ceramic resistor and the same dielectric and shielding materials, were used with the difference that the outer shape of the dielectric and the inner profile of the shielding conductor is designed using the equation (38). This new geometry is presented in the Fig.41.a and it can be noticed from the Fig.41.b that the amplitudes of the reflected signal is very low as compared to the normal coaxial geometry.

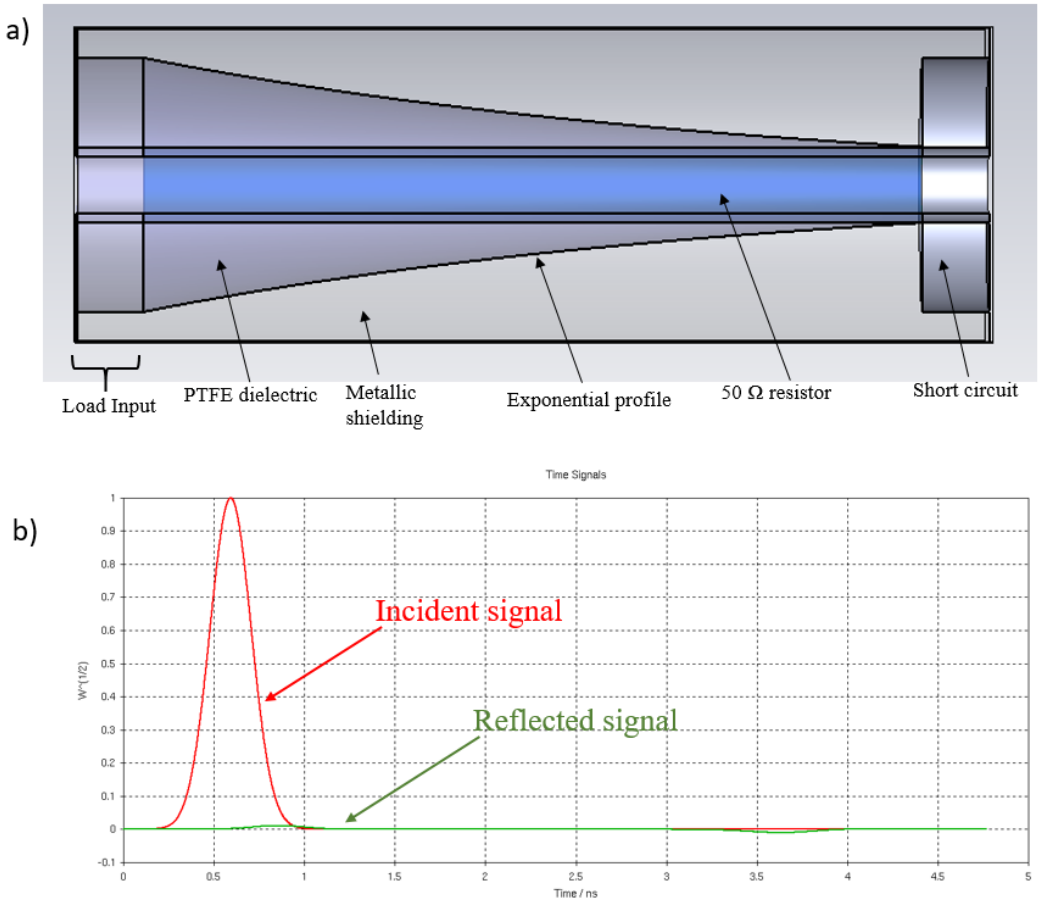

Fig. 41. 50 Ω load with an exponential geometry; a) Different elements constituting the load; b) Incident and reflected signals for the modelled geometry.

From this new geometry, as presented in the Fig.42.a and Fig.42.b, significantly low values of the reflected signals are obtained, resulting in consequently better values of the reflection coefficient (S_{11}) and TDR impedances. The S_{11} of -30 dB and the TDR impedances showing the impedance variations of only around 1 Ω prove that this geometry can be very well used for a matched termination of a 50 Ω transmission line.

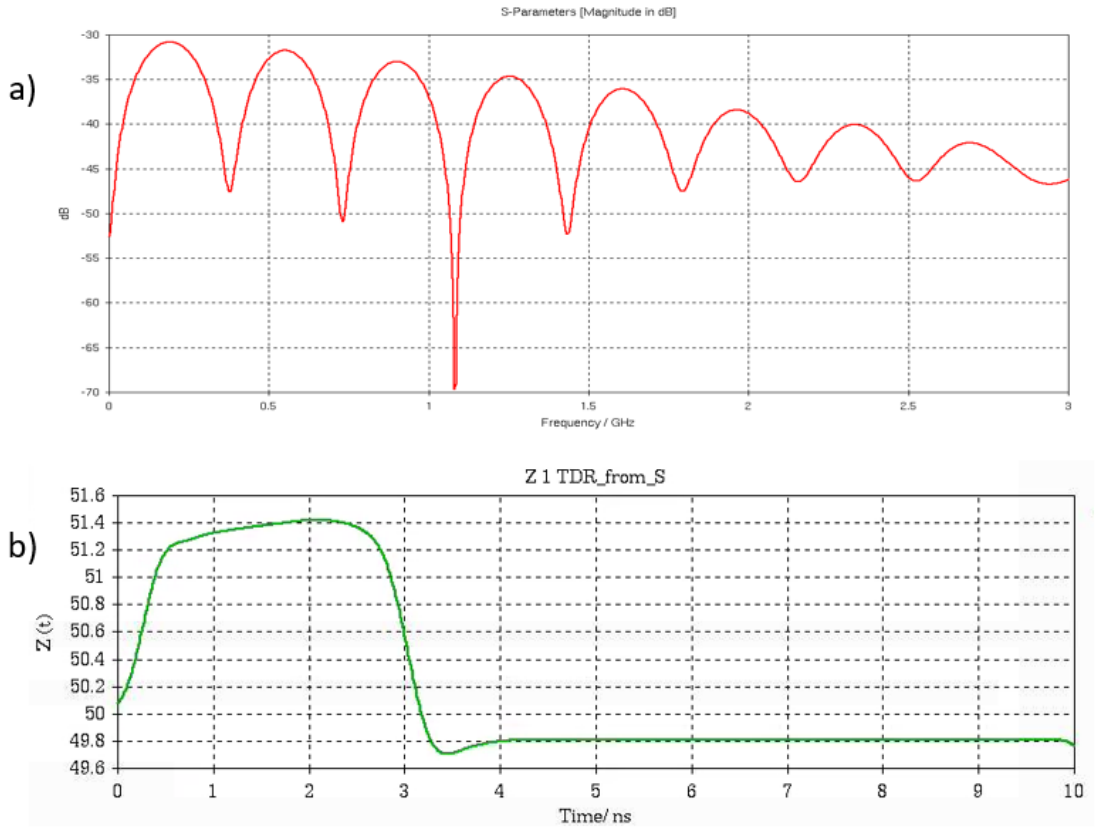

Fig. 42. Exponential 50 Ω load responses; a) S11 parameter (return loss); b) TDR impedance

These above mentioned modelling results for the exponential geometry are largely better than the ones of a normal cylindrical coaxial line. To better visualize the differences and the improvements, the results obtained with both the geometries are presented on the same graph shown in the Fig.43. The modelling results presented prove the better matching capabilities of the 50 Ω load based on the exponential geometry which is a key requirement in the accurate and precise measurements of the pulses through the *CCVD*. The fabrication of the exponential load is presented in the following section.

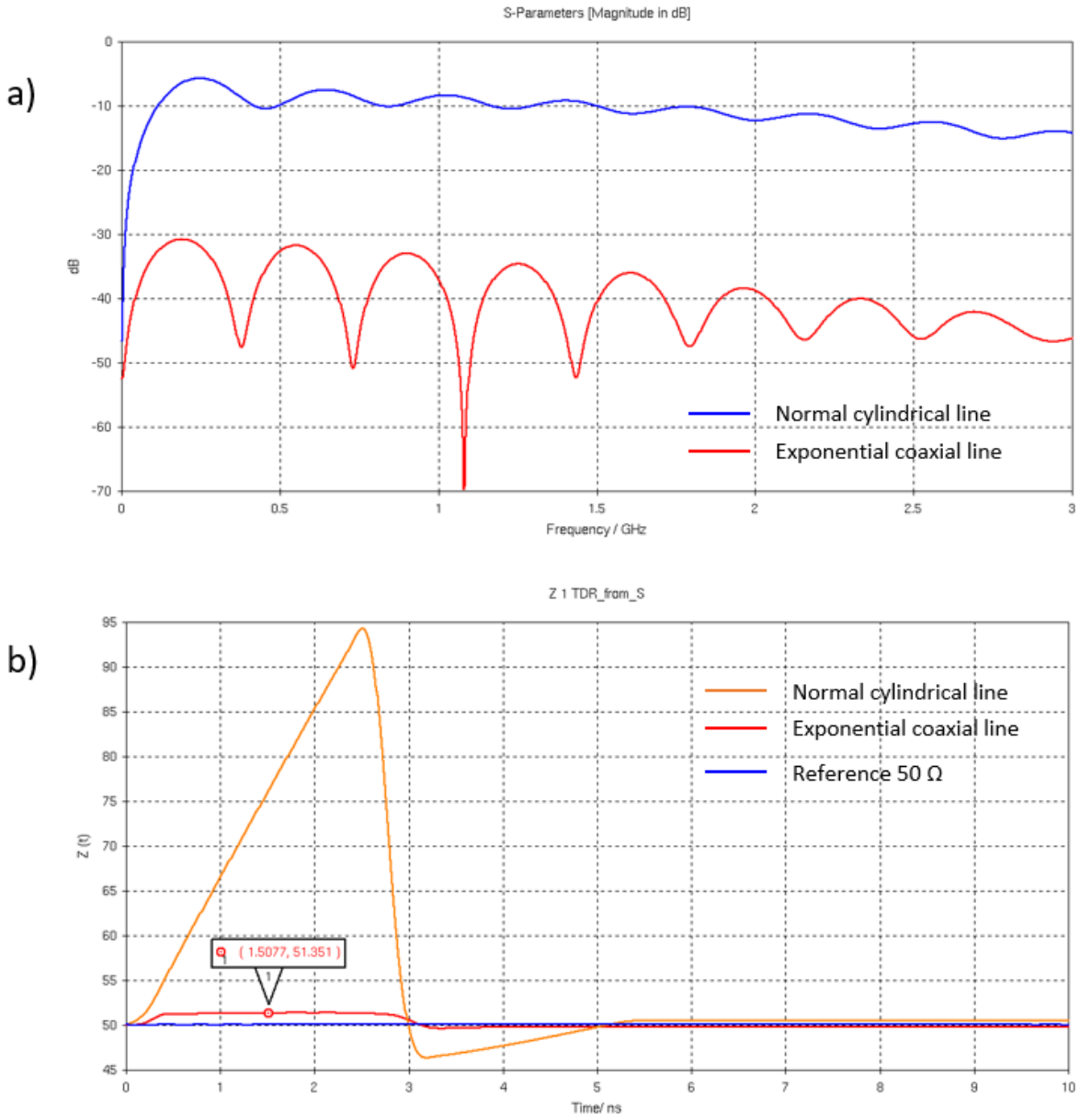

Fig. 43. Comparisons between the two geometry of the load; a) Reflection coefficient (S_{11}) comparison between the normal cylindrical geometry and the exponential geometry of the 50 Ω load; b) TDR response for both the geometries, the blue reference 50 Ω line represents a 50 Ω characteristic impedance coaxial line with no resistor.

3.4. Fabrication of the 50 Ω exponential load

The 50 Ω termination load based on the exponential geometry consists of three major parts, namely, a 50 Ω resistor, a metallic shielding, and a dielectric which is present between these two elements, as presented in the Fig.44.a. The internal diameter profile of the shielding and the outer diameter profile of the dielectric used are defined by the equation (38). The dielectric material is the *Virgin* grade PTFE, which is the same dielectric material used for the realization of the *CCVD*. A 30 cm long 50 Ω ceramic resistor is chosen to be the main line conductors with supplementary connectors and fixations for its integration to the main transmission line. Finally, the shielding is milled in an aluminum alloy block for better heat dissipation. In order to avoid any fabrication error and to ensure the realization of the exact exponential profile as expressed by the equation (38), the mechanical geometry was exported in .STEP files from the modelling structure itself and the mechanical plans were drafted according to them. The manufactured elements constituting the load are presented in the Fig.44.

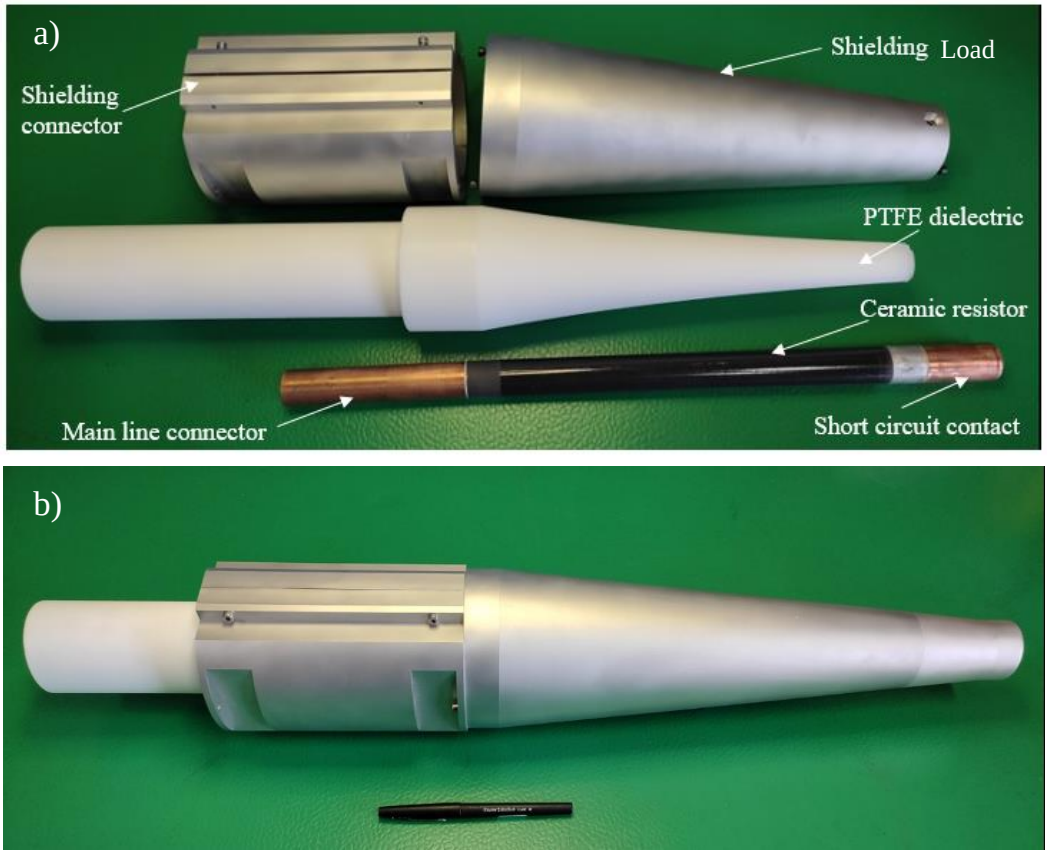

Fig. 44.a) Fabricated elements constituting the 50 Ω exponential load; b) Mounted load

3.5. Development of 50 Ω connectors and transition cones

Other important components constituting the measurement system such as 50 Ω characteristic impedance male and female connectors and the impedance transition cones are developed in this thesis work.

The connectors are necessary to connect different elements of the measurement system together, such as the load to the *CCVD* and even the connection of the complete measurement system to generator for measurements. However, the connectors capable of withstanding voltage peaks as high as 500 kV are unavailable in the market. The geometry of the female and male connectors developed in this work are presented in the Fig.45.a and Fig.45.b respectively. They possess a 50 Ω characteristic impedance, as the main transmission line characteristic impedance, and are capable to provide good insulation to the voltage amplitudes at least up to 500 kV for nanosecond and sub-nanosecond pulses. Sufficient security measures against the flashovers and dielectric breakdown were taken in the designing of different components of the measurement system. Nevertheless, with an inappropriate connector design, the connection portions of the measurement system could cause flashovers and dielectric breakdowns. This is principally due to the connection interface of the connectors, where the inevitable presence of thin layers or small pockets of air reduces the voltage withstanding by the dielectric element. Moreover, the meeting surfaces of the dielectric in the connector could cause the flashovers if they are not designed properly with respect to the dielectric breakdown strength of the air. For the voltage amplitude of 500 kV in air, with dielectric strength of air of 30 kV/cm, a minimum air separation of 17 cm is needed to avoid the flashovers between the conductors of the main line. This distance corresponds to the *Breakdown path* as mentioned in the Fig.45.c. Hence, the breakdown path for the connectors is designed to be 27 cm with 10 cm of margin from the actual length needed. In addition, this mating geometry of the connectors is simulated using the CST software. The waveguide ports were placed at the extremities and the results obtained in terms of the reflection coefficient (S11) and the transmission coefficient (S21) are presented in the Fig.45.d. Extremely low values of around -100 dB were obtained for the reflection coefficient whereas the transmission coefficient values were found to be around 0 dB, proving that the integration of these connectors in the HPPNS measurement system to connect different components together would have a negligible effects on the measured waveform.

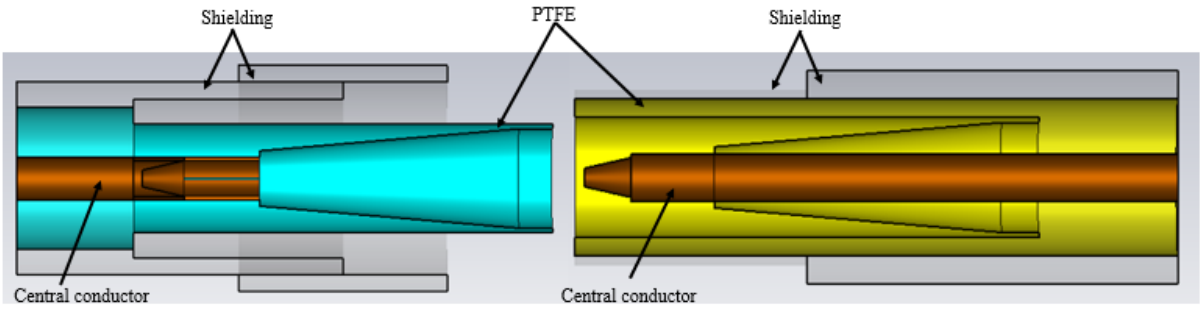

a) Female connector b) Male connector

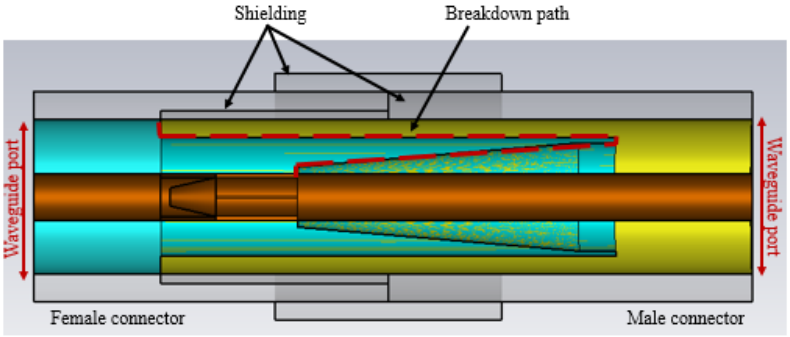

c) Connectors meeting

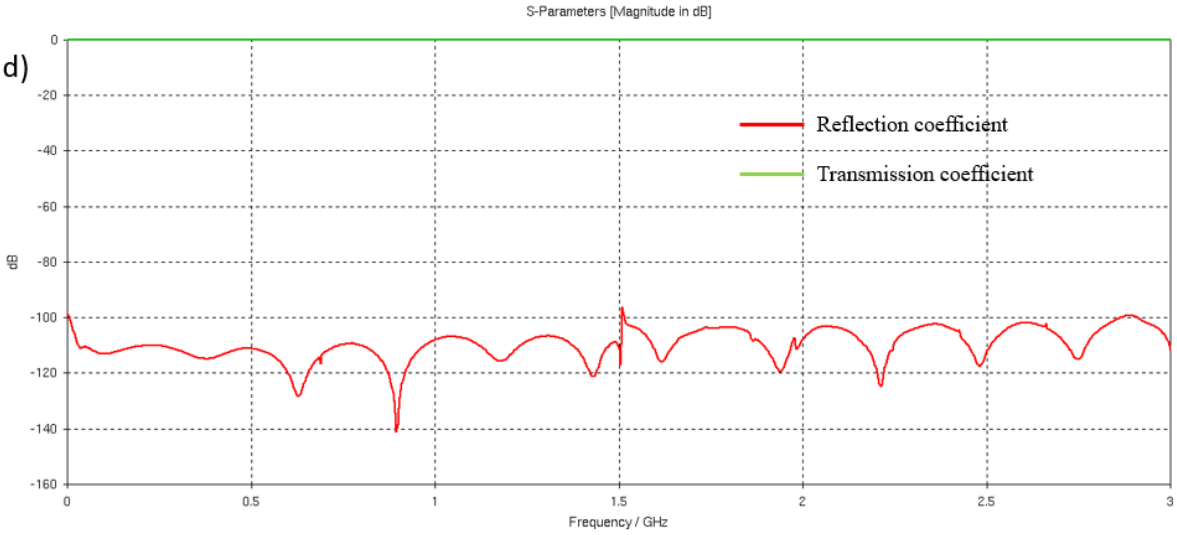

Fig. 45.Modelling of the connectors; a) Female connector; b) Male connector; c) Male and female connectors meeting together, the PTFE dielectric for both the connectors are represented with different colors for visual deference, and the breakdown path represents the meeting surfaces of the dielectrics of both connectors where a thin layer of air could be present; d) Reflection and transmission coefficients of the connector assembly as represented in c).

Furthermore, the developed components of the HPPNS measurement system with the high voltage connectors, such as the CCVD and the 50 Ω termination load, need to be characterized in order to evaluate their responses as a function of frequency in the concerned bandwidth up to at least 2 GHz. These characterizations will be performed in terms of S parameters, at low power levels, through a Vector Network Analyzer (VNA) and another high frequency calibration setup, which possess Type-N connectors at their inputs of dimensions different from the high voltage male and female connectors developed. To connect the components of HPPNS system to these measurement setup, 50 Ω characteristic impedance transitions cones are necessary, allowing to keep a constant characteristic impedance while ensuring a transition between the dimensions of the high voltage connectors and the Type-N connectors. These transition cones possess male or female high voltage connectors at one end, as shown in the Fig. 45, and Type-N connectors at the other end. The transition cones developed are presented in the Fig.46.a and the results of the modelled CST geometry of the mating of high voltage connectors with these transition cones are presented in the Fig.46.b in terms of reflection and transmission coefficients which are found to be around -40 dB and 0 dB respectively. These values of the modelling responses show that these transition cones will have negligible effects on the high frequency low power characterization results of the components of the HPPNS measurement system.

a)

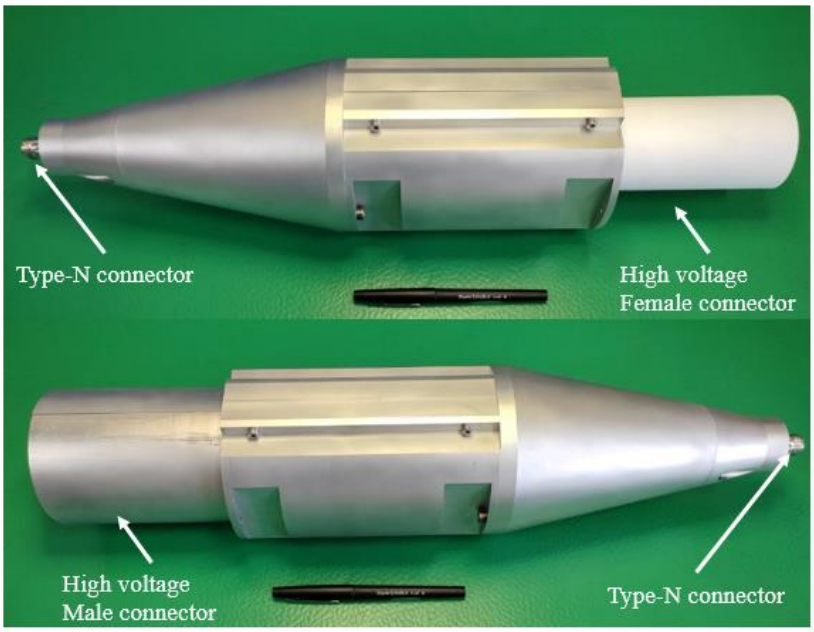

b)

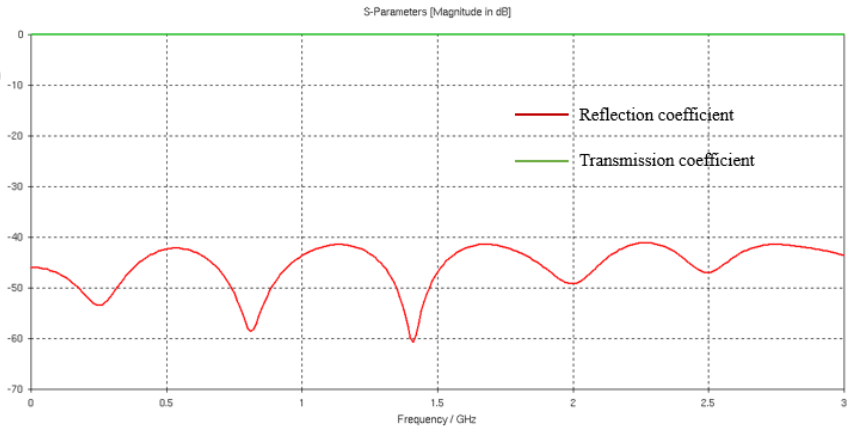

Fig. 46.a) Transition cones with high voltage and Type-N connector; b) Transmission and reflection coefficients of the modelled transition assembly.

3.6. Conclusion

Some necessary components of the HPPNS measurement system, such as, a 50 Ω termination load and high voltage male and female connectors are presented in this chapter. The factors affecting the frequency responses of these components and, more importantly, their voltage withstand capabilities for voltage peaks up to 500 kV are also discussed. The CST simulations in the concerned frequency domain, up to at least 2 GHz, show that the modelled geometry for the 50 Ω termination load possess a maximum reflection coefficient of -30 dB, which is an acceptable value and will have almost negligible effects on the measured pulses at the output of the CCVD. In addition, the reflection and the transmission coefficients simulations results for the high voltage connectors prove that the integration of these connectors in the HPPNS measurement system will not modify the characteristics of this latter. Following these simulations results, mechanical realizations were performed and finished components are shown. Finally, transitions cones, mandatory for the high frequency low power characterizations of these components are also fabricated.

All of these developed components in this chapter complete the HPPNS measurement system and the calibration of each component developed and of the complete measurement system is presented in the next chapter.

CHAPTER

4

This last chapter is about the characterizations and validation of the HPPNS measurement system developed in this thesis. These characterizations were performed through two different methods, namely, VNA characterization and High Frequency traceable characterization methods. The characterizations were necessary in order to analyze the transmission coefficient of the developed system, which can easily be converted to the division ratio, as a function of frequency. A relatively flat 85 dB attenuation was obtained up to the frequencies of at least 2 GHz. The characterization results were also compared with results obtained from the modelling of the measurement system. Furthermore, a Marx generator with pulse forming lines was used for high voltage insulation testing and real time measurements. Pulses with rise times as high as 450 picoseconds were measured through the HPPNS measurement system. All of these results are presented in the following chapter.

Chapter 4: Characterization of the HPPNS measurement system

During the first phases of validation and testing of the HPPNS measurement system, each component of the system developed, such as, the *CCVD*, 50 Ω termination load, high voltage 50 Ω male and female connectors, and the transitions cones, were tested mechanically for their final dimensions and integration into each other. These tests were necessary for the finalization of each component before they could be characterized. After these mounting tests, each of them were calibrated separately, thanks to the connectors developed, in order to measure their frequency responses

through a *Vector Network Analyzer* (VNA). Further to these separate calibrations, these components were mounted together and the frequency response of the whole system was measured, firstly, through the VNA, and secondly through a high frequency SI Traceable attenuation measurement method to confirm the measurements obtained from the VNA. The characterization methods and the results obtained are described in this chapter.

4.1. Characterization of the HPPNS measurement system through VNA

For the characterizations presented in this section and subsections, an *Agilent E5071C (9 kHz to 4.5 GHz)* network analyzer [107] is used. Prior to the measurements carried out through a VNA, an important step is its own calibration. This calibration should be performed before the commencement of the measurements of the device under test (DUT), which in our case are the 2-port networks mostly. There are multiple techniques for the VNA calibration. Several of these techniques, such as, SOLT, QSOLT and SOLR require reflection calibration for one or more of the test ports. SOLT is probably the best-known calibration technique, which consists of a one-port calibration on each test port followed by a known through calibration between the test ports. The most suitable calibration techniques for the VNA calibration to perform the measurements on the components developed in this thesis work is the SOLT technique. It requires short, open, load and through calibration standards in the characteristic system (and DUT) impedance. The standard values, as determined by their mechanical dimensions, are loaded into the VNA prior to calibration. The location where the calibration standards are attached (the VNA port, the end of a cable, or inside a test fixture) is where the measurement begins and ends. This location is known as the reference plane or measurement plane.

Just after its calibration, the VNA is used to perform the S parameters measurements of the components constituting the HPPNS measurement system and later, the complete measurement system was characterized using the same procedure. These separate characterizations of each component are necessary in order to evaluate their footprints on the whole system. The results obtained from these characterizations are compared to results obtained from the modelling of the same components using *CST Microwave studio®*. These results are presented in the following sub-sections.

4.1.1. Characterization of high voltage connectors and transition cones

The high voltage male and female connectors developed in this thesis work are an important element in the HPPNS measurement system. They are not only necessary for connecting different components together but also they are used to connect the whole measurement system to the high voltage pulse generators. These connectors are designed in order to withstand voltage amplitudes up to 500 kV for nanosecond pulses and even higher voltage peaks for sub-nanosecond pulses. Special care was taken during the designing process of these connectors to keep the reflection coefficient as low as possible and the transmission coefficient of around 0 dB for the frequencies at least up to 2 GHz. Moreover, the CCVD, the 50 Ω termination load and transition cones were all designed and fabricated with these connectors. For example, as presented in the Fig.30, the CCVD possesses a female and a male connector at its both main transmission line extremities, in the Fig.44 the 50 Ω termination load is fabricated with a female connector and in the Fig.46 the two transition cones were produced each with a male and a female connector at one end and type-N connectors at the other. These type-N connectors are necessary for high frequency low power calibrations of these different components because they permit their connections to VNA and other calibration setups through transition cones for the measurements of the frequency responses (S parameters) of these components. However, it is necessary to measure the frequency response of these transition cones to evaluate their own footprint. The VNA measurement setup of these transition cones with high voltage connectors are shown in the Fig.47 with the two type-N ports connected to the two ports of the VNA. A comparison between the S parameters obtained through these measurements and the electromagnetic modelling up to 3 GHz is presented in the Fig.48.

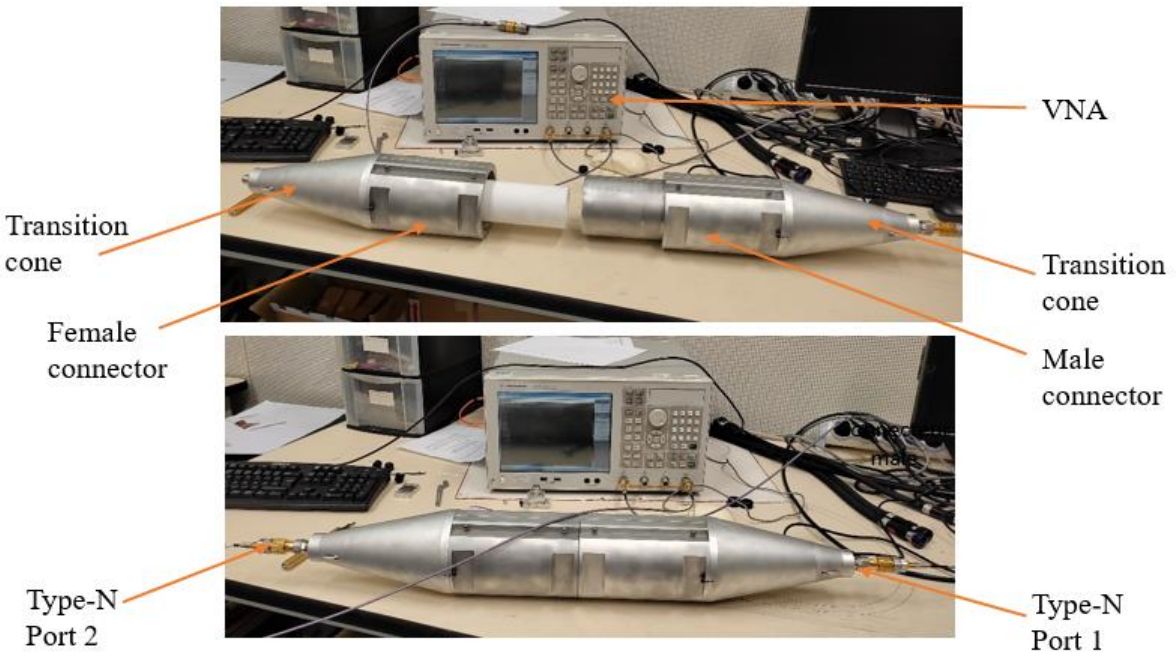

Fig. 47. S parameters measurement setup for transition cones and high voltage connectors

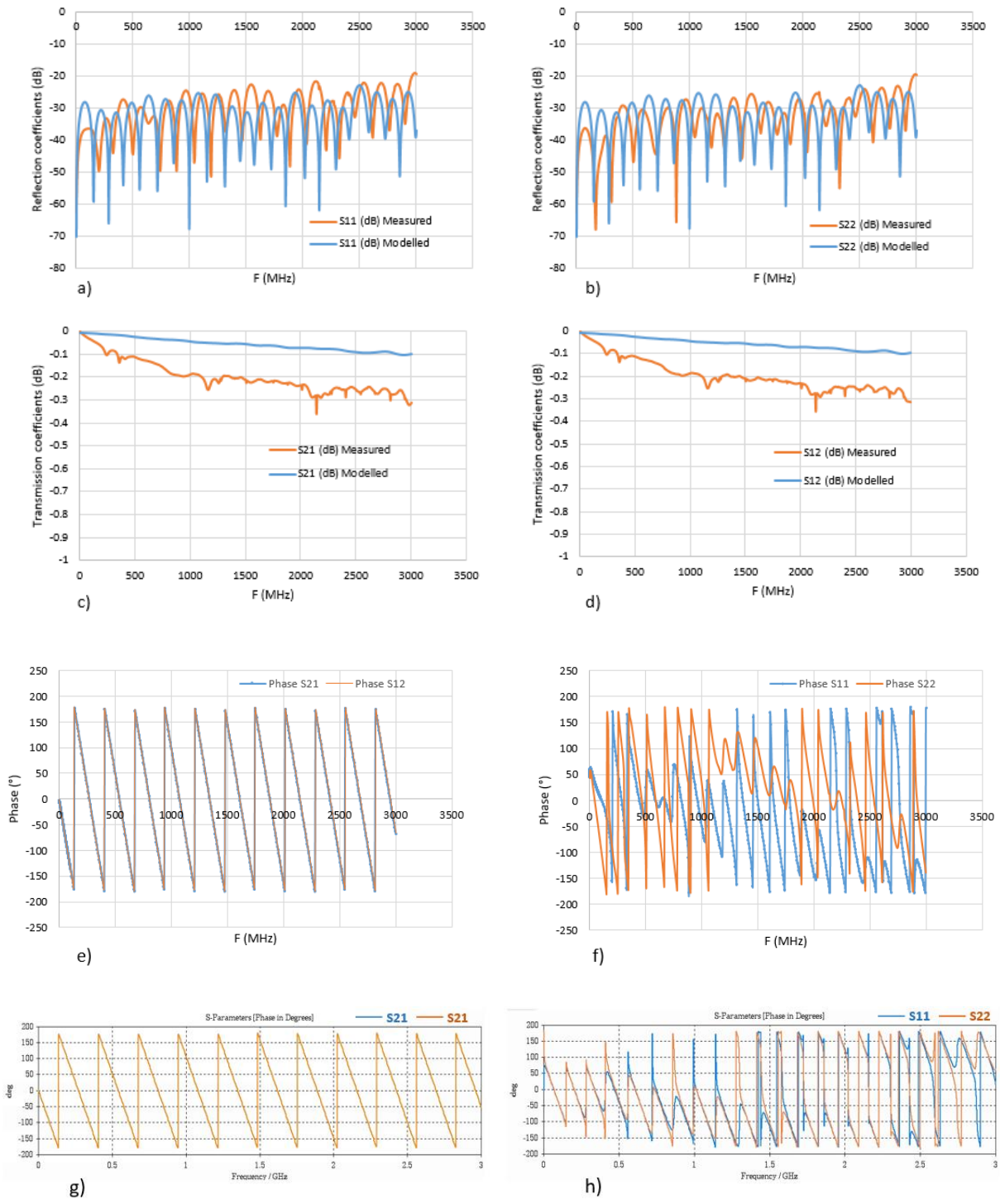

Fig. 48. Comparisons of S parameters and phase responses of the assembly of the transition cones, as presented in the Fig.47, with high voltage connectors up to 3 GHz , a) and b) reflection coefficients, c) and d) transmission coefficients, e) and f) measured phase responses associated with these S parameters; and g) and h) S parameters phase responses of the simulated geometry

It can be observed from the Fig.48 that the reflection coefficients (S_{11} and S_{22}) are almost similar for the modelled and the fabricated transition cones with high voltage connectors. However, a small difference can be noticed in the comparisons between the measured and modelled transmission coefficients (S_{12} and S_{21}). This is principally due to the mechanical imperfections in the realization of the conical cavity, for the central conductor, of the PTFE dielectric used in the transitions. During the fabrication process, it was noticed that the 170 mm long conical cavity at the center of the PTFE cone, shown in the Fig.49, presented some anomalies due to the passage of the drilling instrument and was not smooth. Indeed, it is quite difficult to dig out a perfect conical cavity for such long lengths and taking into account the acceptable values of the measured transmission coefficient up to 2 GHz (-0.23 dB) and due to lack of time, it was decided to move forward with these imperfections.

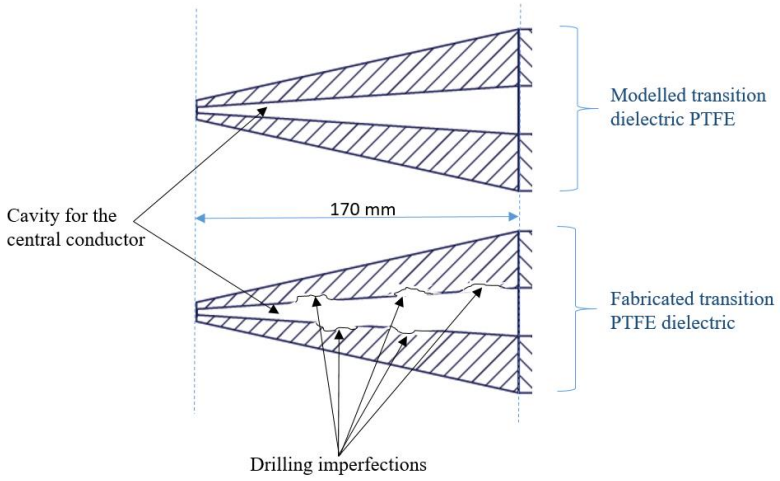

Fig. 49. Difference between simulated and realized PTFE transition dielectric

4.1.2. Characterization of 50 Ω termination load

As it is mentioned in the section *3.1*, guaranteeing the 50 Ω impedance value of the transmission line termination load over the concerned frequency range, at least up to 2 GHz, is very essential for a reflection less measurement of the incident high voltage pulses. Therefore, the reflection coefficient (S_{11}) of the 50 Ω load should be as small as possible, over all the concerned frequency range. However, it is almost impossible to develop a termination load with a zero reflection coefficient value, especially in the high

voltage domain that imposes uncompressible dimensions of the elements used to fabricate this load. Nevertheless, the reflection coefficient value can be minimized through some special geometrical compensations, as it is shown by the electromagnetic modelling of the exponential geometry of the load in the section *3.3*. The modelling showed that the S_{11} value obtained through the exponential geometry is below -30 dB. The reflection coefficient of the fabricated 50 Ω load was measured though the calibrated VNA. The measurement setup is presented in the Fig.50 and the comparison of measured and modelled results of the reflections coefficients and the modulus of the impedance (*Z*) at the input of the load are presented in Fig.51.

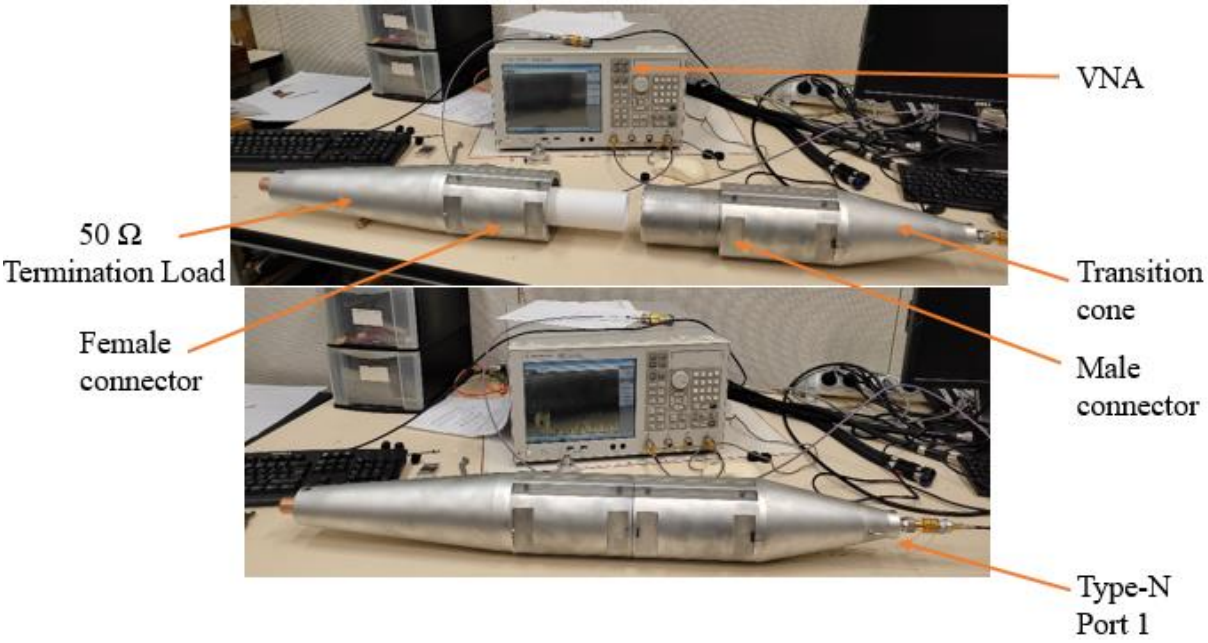

Fig. 50. S parameter measurement setup for the 50 Ω transmission line termination load

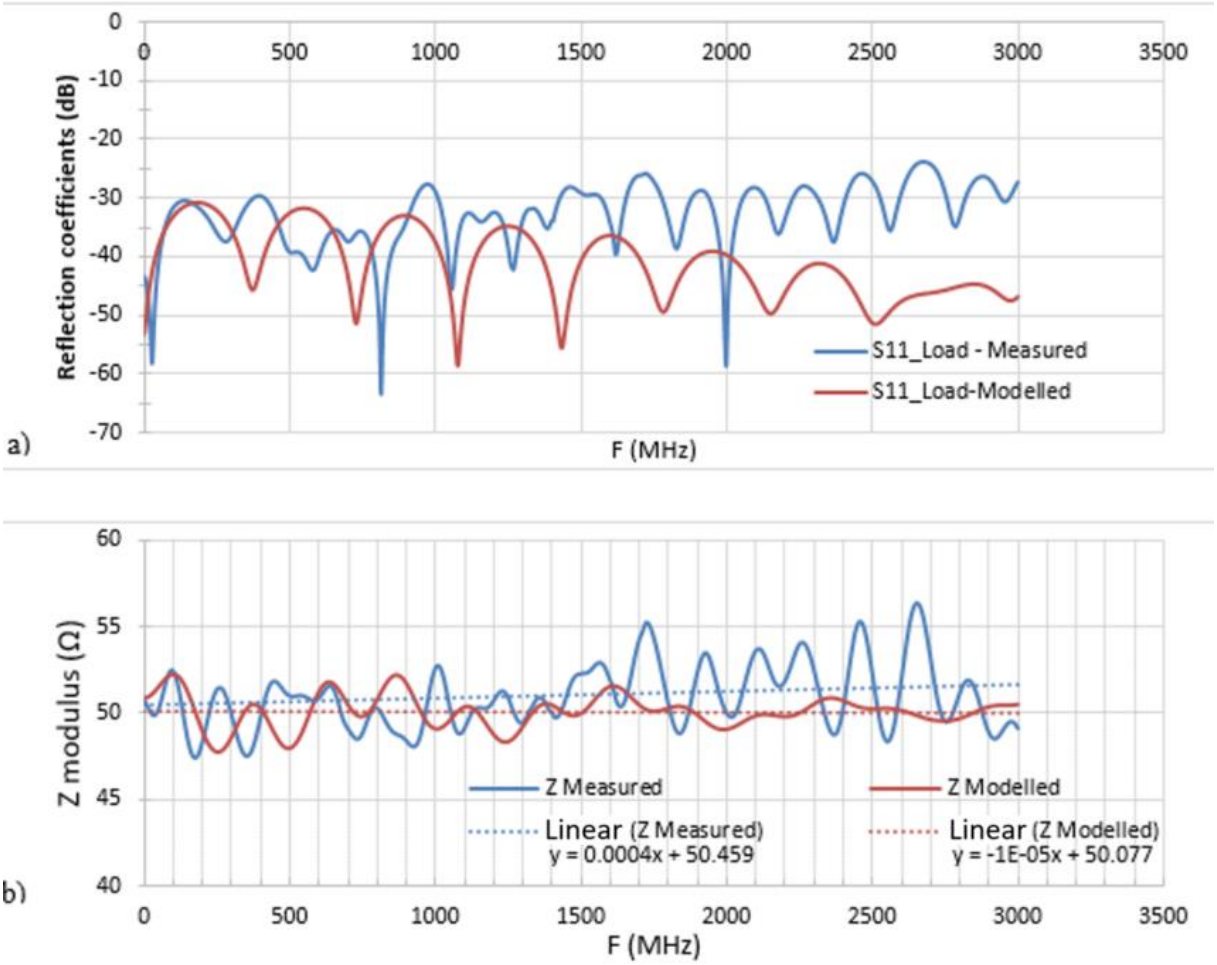

Fig. 51. Measurements of the 50 Ω transmission line termination load compared to the modelled geometry, a) Reflection coefficients, b) Impedance at the input of the load and the linear trend line with corresponding linear fitting equations

The results in the Fig.51 show that the measurements are close to the modelling results, at least up to the concerned high frequency limit of 2 GHz. The small differences observed are principally due to the mechanical tolerances that are necessary for the fittings of the different elements of the load and the high voltage connector. Furthermore, these elements are of dimensions of tens of centimeters, around 50 cm for the PTFE dielectric, for which the control and the corrections of the coaxiality are often difficult to perform. These variations will be taken into account in the final uncertainty budget.

4.1.3. Characterization of the complete HPPNS measurement system

The analysis of the characterization results of the transition cones and the 50 Ω transmission line termination load showed that these components will have almost negligible footprint on the behavior of the whole HPPNS measurement system. Further to that, the complete measurement system was mounted together with the CCVD for the calibration. This is the most important measurement that determines the response and the efficiency of the HPPNS measurement system developed in this thesis. The measurement setup is shown in the Fig.52 and the results obtained in terms of modulus and phases of the S parameters are presented in the Fig.53.

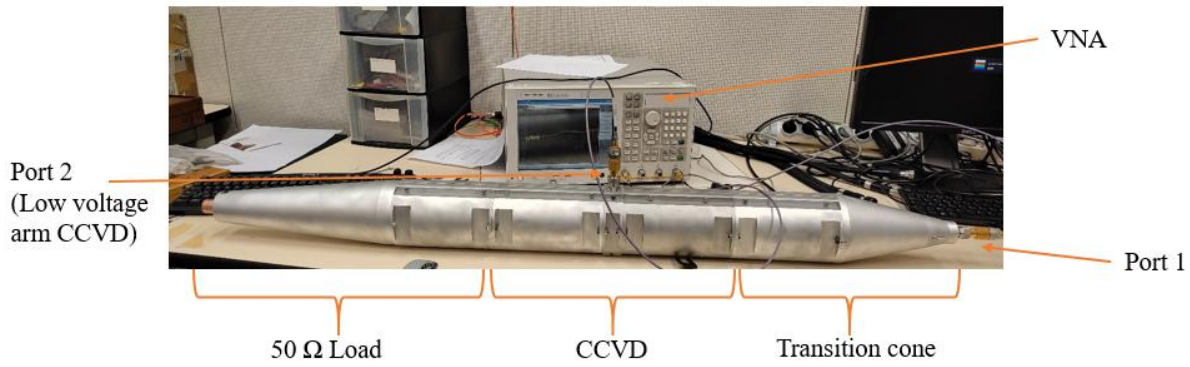

Fig. 52. VNA calibration setup of the HPPNS measurement setup

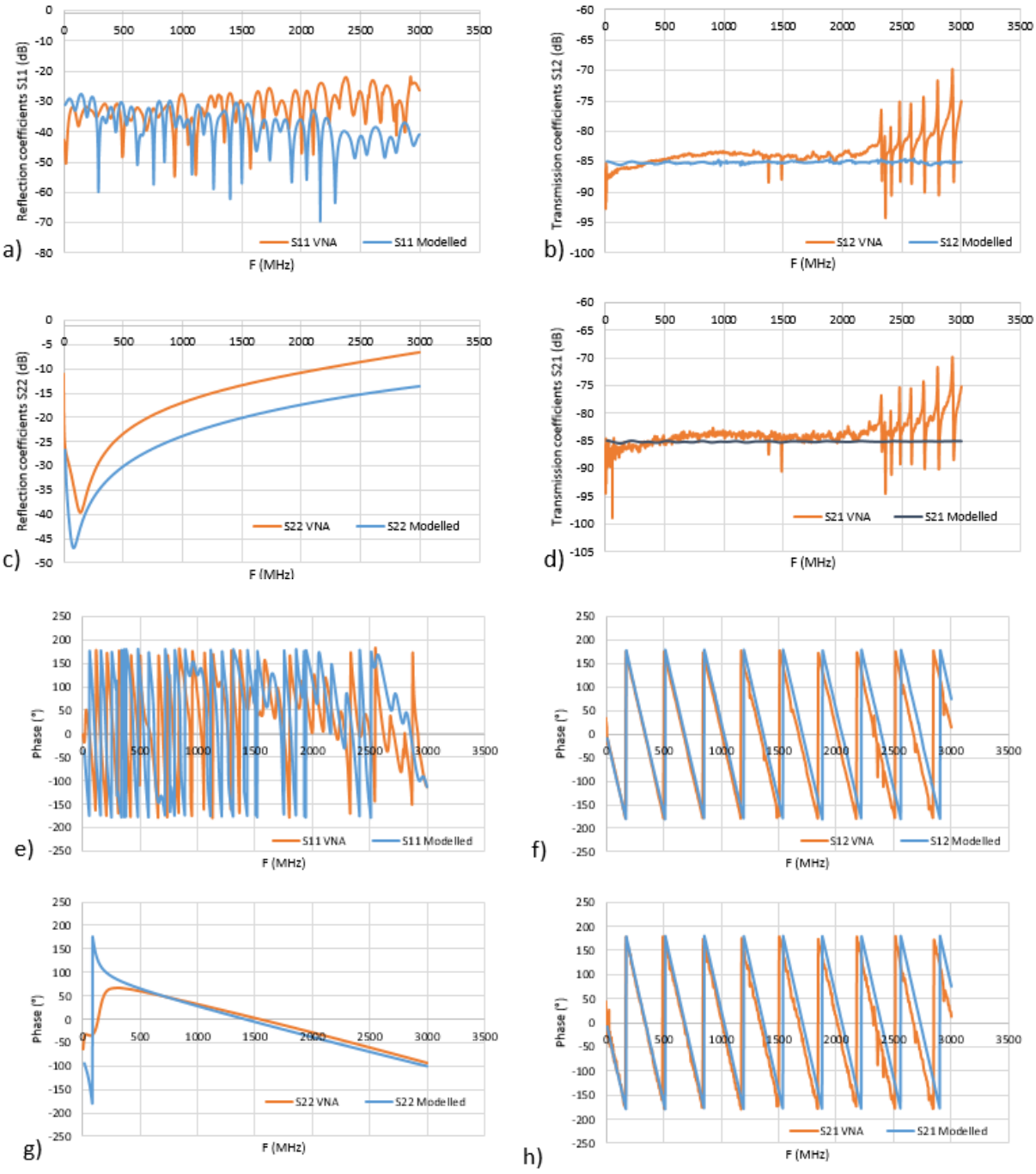

Fig. 53. S parameters modulus and phase comparisons for the measured and modelled geometries of the complete HPPNS system, a) Reflection coefficient at the entry of the measurement system, b) transmission coefficient from the entry to the CCVD output, c) Reflection coefficient at the output of the divider, d) transmission coefficient from the output of the CCVD to the entry, and e), f), g), h) represent their respective phases

The results presented in the Fig.53 demonstrate that the fabricated HPPNS measurement system has almost similar characteristics to the modelled system. The

measured reflection coefficient of the complete system at the high voltage input is found to be less than –27 dB for the frequencies up to 2 GHz and for even higher frequencies it remains relatively low. This low value of the reflection coefficient proves that the developed system is well matched to the 50 Ω impedance. Furthermore, a relatively flat frequency response is measured for the transmission coefficients of -85 dB from few tens of megahertz up to 2 GHz of the HPPNS measurement system, with a standard deviation of 1.5 dB. This represents a division ratio of around 17000:1 of the HPPNS measurement system. In addition, the value of the standard deviation will be taken into account in the division ratio of the HPPNS measurement system, because the values of the division ratio will be chosen as a function of frequency, i.e. each value of frequency, in the concerned bandwidth of the measured signal, will have its own value of the division ratio. This procedure is described more in detail in the section *4.4*.

These results show the efficiency of the developed HPPNS measurement system to realize the measurements of fast pulses with rise times up to at least 200 picoseconds ($\frac{0.35}{2\ GHz}$). The measured transmission coefficient obtained through the calibrated VNA was further confirmed by a different measurement setup, which is traceable to the SI and which is presented in the following section.

4.2. Characterization of the HPPNS measurement system through a high frequency traceable measurements of the attenuation factor

The transmission coefficient of the fabricated HPPNS measurement system, which can easily be converted in to the division ratio, is the inverse of the attenuation which is applied as a function of frequency to the incident high voltage pulse before it could be measured. This attenuation can also be measured through a traceable high frequency attenuation measurement method used in the high frequency calibration laboratory of the LNE. The schematic of this measurement system is presented in the Fig.54.

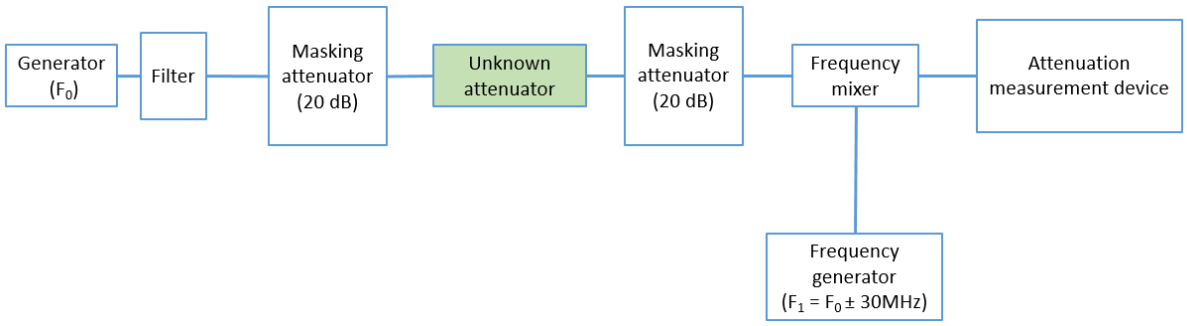

Fig. 54. Schematic of the high frequency SI traceable attenuation measurement system

Principle of the method showed in the Fig.54, a similar method is described by Wu [108], consists of the transposition of a high frequency attenuation to an attenuation at a lower frequency, by substitution. The measurement setup measures the attenuation of an unknown attenuator at the desired frequency of a signal (F_0) in the range from 5 MHz to 26 GHz. This frequency is superposed to a 30 MHz signal and, through a frequency mixer, only the 30 MHz signal is applied to the standard attenuation measurement device. For higher values of attenuations of the unknown attenuator, two masking attenuators of values 20 dB each are used for higher signal to noise ratios and for better impedance matching. The measurement procedure is repeated at each frequency in the desired frequency bandwidth. The results of the characterization of the HPPNS measurement system obtained through this measurement setup are compared to the VNA characterization and the CST modelling, and are presented in the Fig.55. The ***HF1*** and ***HF2*** results presented in the Fig.55 are the characterization results obtained from the same high frequency traceable method at an interval of two months for the consistency of these results. The absolute expanded measurement uncertainty of these measurements is 0.15 dB for all the concerned frequencies. It can be noticed that these

results are in very good agreement with the CST microwave modelling up to the frequencies of 2 GHz.

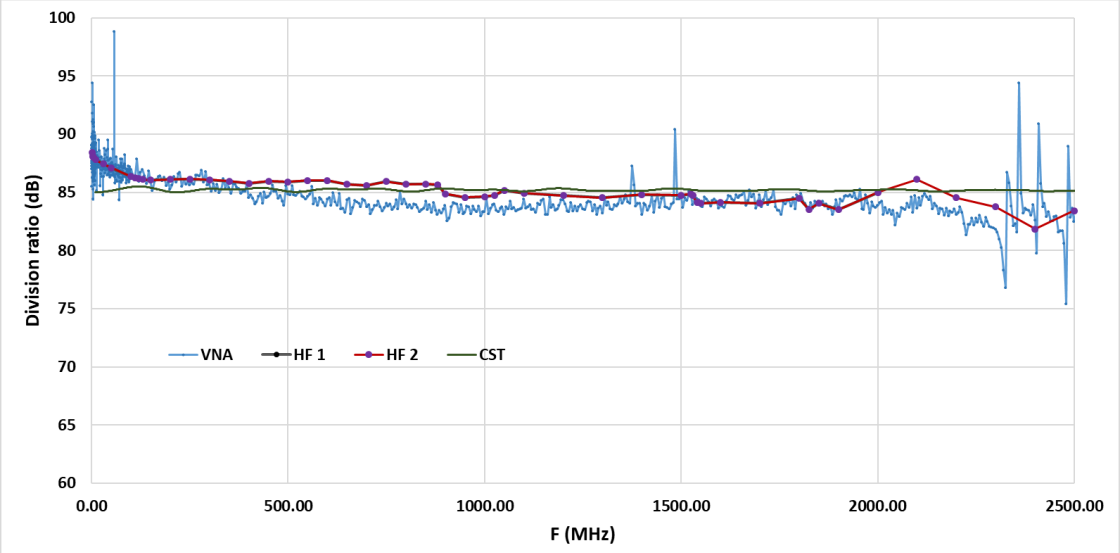

Fig. 55. Comparison of different characterization results obtained for the HPPNS measurement system.

At first, the HPPNS measurement system was characterized through this method only for the frequencies up to 2 GHz (HF 1) and later this characterization was extended to 3 GHz (HF 2) in order to study the behavior of the system for higher frequencies. Some abnormal behaviors can be observed for these higher frequencies, which is still need to be confirmed. However, as far as this thesis is concerned, the results obtained up to 2 GHz are more than satisfactory.

4.3. Measurements of nanosecond and sub-nanosecond high voltage pulses

The frequency domain characterization of the HPPNS measurement system demonstrated that it can be very well used to measure high voltage pulses with rise times as low as 200 picoseconds, which respects the objectives, see Table 1, that were fixed for this thesis. However, all of these characterizations were carried out in the domain of low power and the capability of the HPPNS measurement system to withstand voltage peaks as high as 500 kV remains to be tested.

For the high voltage tests, a collaboration between the *LNE* and the *SIAME Laboratory, Pau France* was initiated. The objective of the campaign was to carry out measurements on high voltage pulses in order to validate the bandwidth, the attenuation and the voltage withstand properties of the developed HPPNS measurement system. A pulse generator capable of delivering 500 kV of peak voltages to a 300 Ω load [109], with different pulse forming lines (PFL) was graciously made available at the *SIAME Laboratory* to perform these measurements and the HPPNS measurement system was transported from *LNE* to their facilities. Different kinds of pulses were generated and measured through the developed system. Some of the measurements of these high voltage pulses through HPPNS measurement system, necessary for the validation of this latter are presented in this section.

The 85 dB of the attenuation obtained from the characterization of the HPPNS measurement system developed in this thesis corresponds to a division ratio of almost 17000:1. For voltage peaks of 500 kV, this division ratio will result to an output voltage of around 30 V, which is still higher than the 10 V nominal input voltages of most of the oscilloscopes used at 50 Ω input impedance. To perform measurements at these levels of voltage peaks, as presented in the Fig.56, a 50 Ω nominal impedance commercial 20 dB attenuator of 7 GHz bandwidth was added to the output of the HPPNS measurement system. Furthermore, two coaxial cables of 5 meters each were used for the output signal acquisition on a large bandwidth oscilloscope.

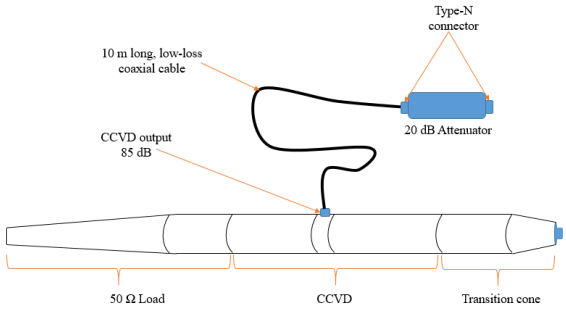

Fig. 56. HPPNS measurement system with a 10 m long low-loss coaxial cable and a 20 dB attenuator

This whole system was re-characterized using the VNA and the high frequency traceable methods, as described in the paragraph *4.1* and *4.2*, respectively. These characterization results are presented in the Fig.57. The absolute expanded measurement uncertainty of the HF measurement is 0.2 dB for all the concerned frequencies.

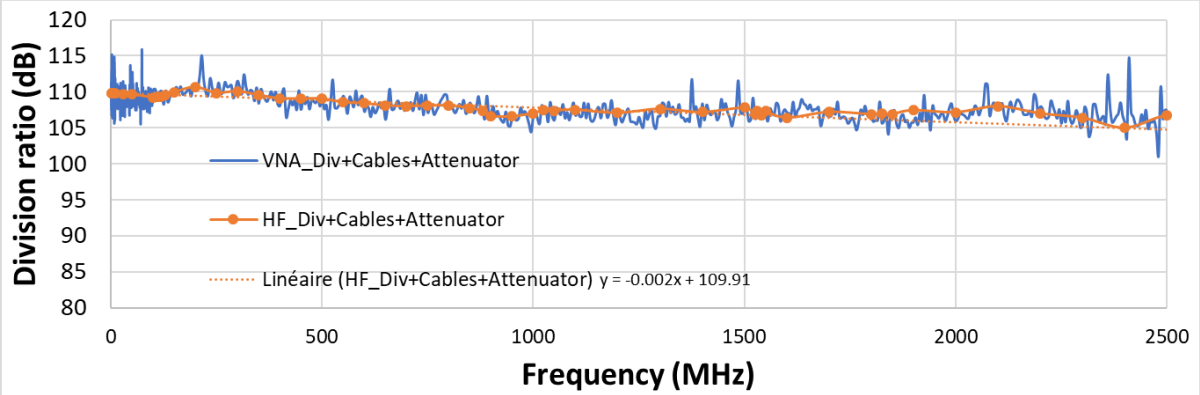

Fig. 57. Characterization of the HPPNS measurement system with connecting cables and 20 dB attenuator up to 2.5 GHz using a calibrated VNA (blue) and High frequency traceable method (orange). A linear tendency line is also presented.

These supplementary 20 dB attenuators and cables augmented the total attenuation of HPPNS measurement system to around 110 dB, which in linear scale corresponds to a division ratio of approximately 316000:1. For a 500 kV pulse peak, this division ration corresponds to an output peak voltage of around 2 V, which is an acceptable and safe input voltage level for oscilloscopes used at a 50 Ω input impedance for the analysis of the waveforms.

For more precision, the division ratio obtained from the HF traceable method for the HPPNS measurement system, was applied at each frequency corresponding to the frequencies present in the frequency spectrum of the measured pulse. This was done

through the *Fast Fourier Transform* (FFT) of the measured pulse recorded at the output of the system. The frequencies in the FFT were matched with the same frequencies present in the characterization curve of the HPPNS measurement system, presented in the Fig.57, and the corresponding amplitudes were multiplied together to obtain the incident pulse generated by the pulse generator through *Inverse Fast Fourier Transform* (FFT^{-1}). The measurement setup at the SIAME Laboratory is presented in the Fig.58 with a PFL attached to the Marx generator. An example of a 200 kV pulse generated directly at the output of the Marx generator (the Marx generator connected directly to the HPPNS measurement system without PFL) is presented in the Fig.59. In addition, the details of other two measurements for the highest values of the voltage peaks, which the generation system was capable to generate on a 50 Ω load, of different waveforms, are presented in the Fig.60 and Fig.61. The reconstruction procedure of the incident pulses with the FFTs, as mentioned above, and the analysis of the reconstructed pulses in terms of voltage and temporal parameters are also depicted in the Fig.59-61. For most of the measured pulses, an offset of several tens of kilovolts can be observed, and for the analysis purposes, this offset at the foot of the rising pulse is considered as the beginning of the pulse and denoted as ***0%*** and the highest point attainted by the pulse is denoted as ***100%***, and the corresponding values of the time and voltages are noted for both of them. The voltage differences between these values are noted as the ***Voltage peak***. Furthermore, as the ***Rise time*** is the amount of time a pulse takes to go from the low to high voltage, the rise time is measured from ***10%*** to ***90%*** of the ***Voltage peak*** of the pulse. Similarly, as the pulse width is the amount of time the pulse takes to go from low to high and back to low again, the pulse width is measured at 50% of the ***Voltage peak*** on the rising and the falling side of the pulse and is denoted by ***Delta 50-50***.

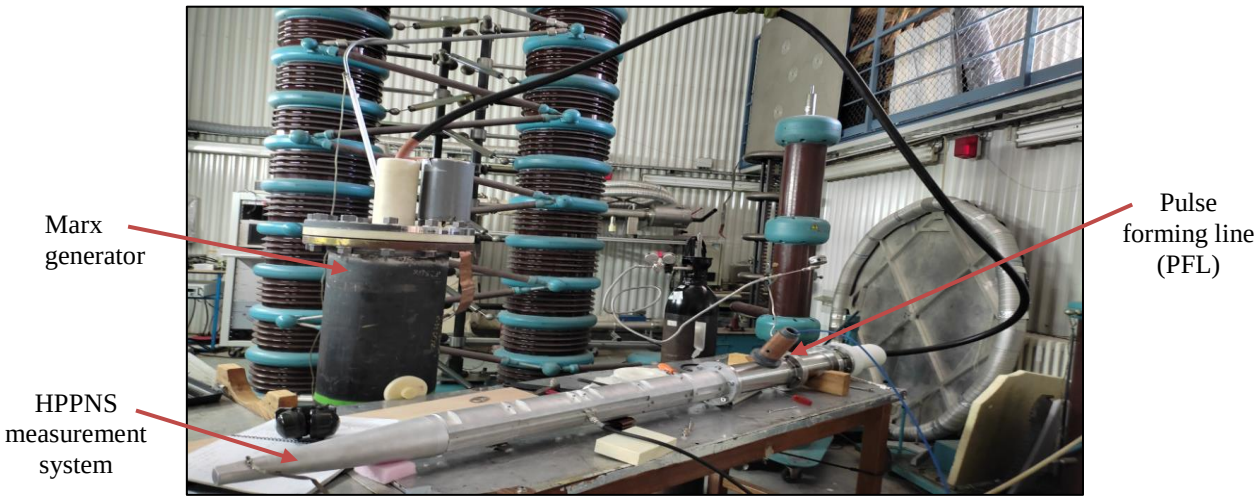

Fig. 58. Measurement setup for high voltage testing of the developed HPPNS measurement at SIAME laboratory

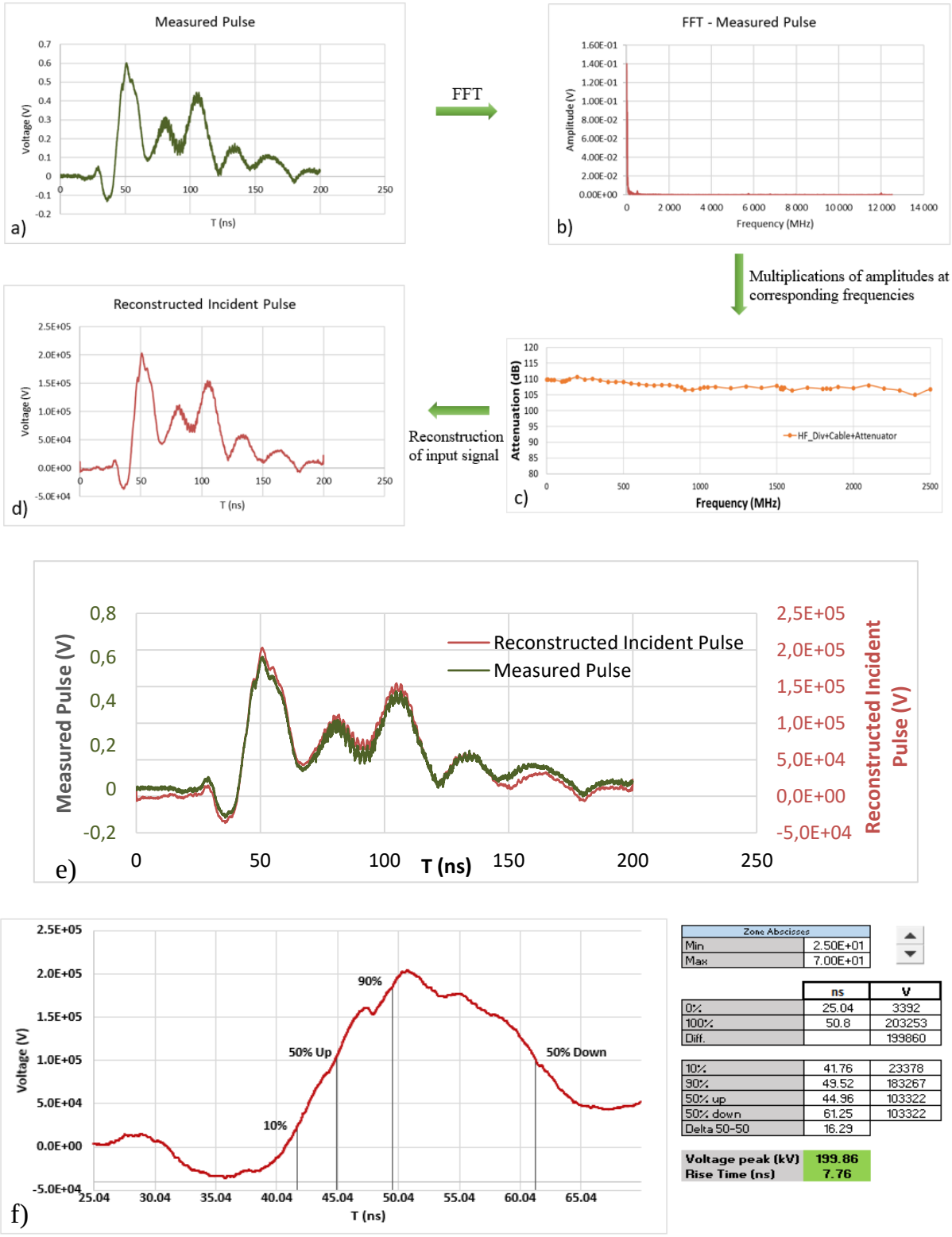

Fig. 59. A 200 kV output pulse of the Marx generator on a 50 Ω load, a) measured pulse at the output of the HPPNS measurement system; b) FFT of the measured pulse, which is multiplied to the corresponding attenuations in c); the reconstructed 200 kV input pulse generated by the Marx generator is presented in d); e) superposition of the measured and reconstructed pulses and f) rise time and voltage peak measurements of the reconstructed incident pulse

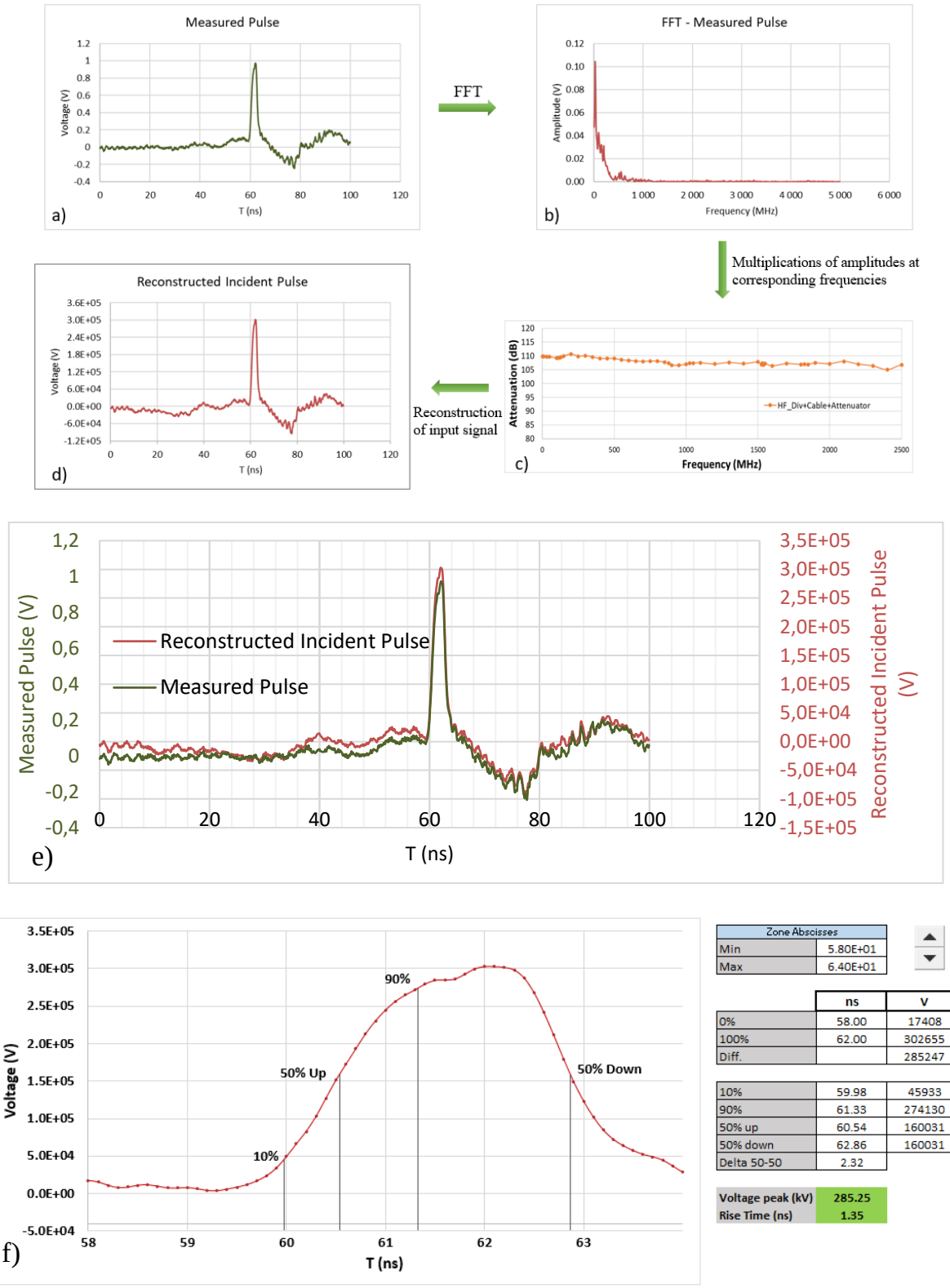

Fig. 60. 300 kV unipolar pulse. a) measured pulse at the output of the HPPNS measurement system; b) FFT of the measured pulse, which is multiplied to the corresponding attenuations in c) and the reconstructed 300 kV input pulse generated by the Marx generator is presented in d); e) superposition of the measured and reconstructed pulses and f) rise time and voltage peak measurements of the reconstructed incident pulse

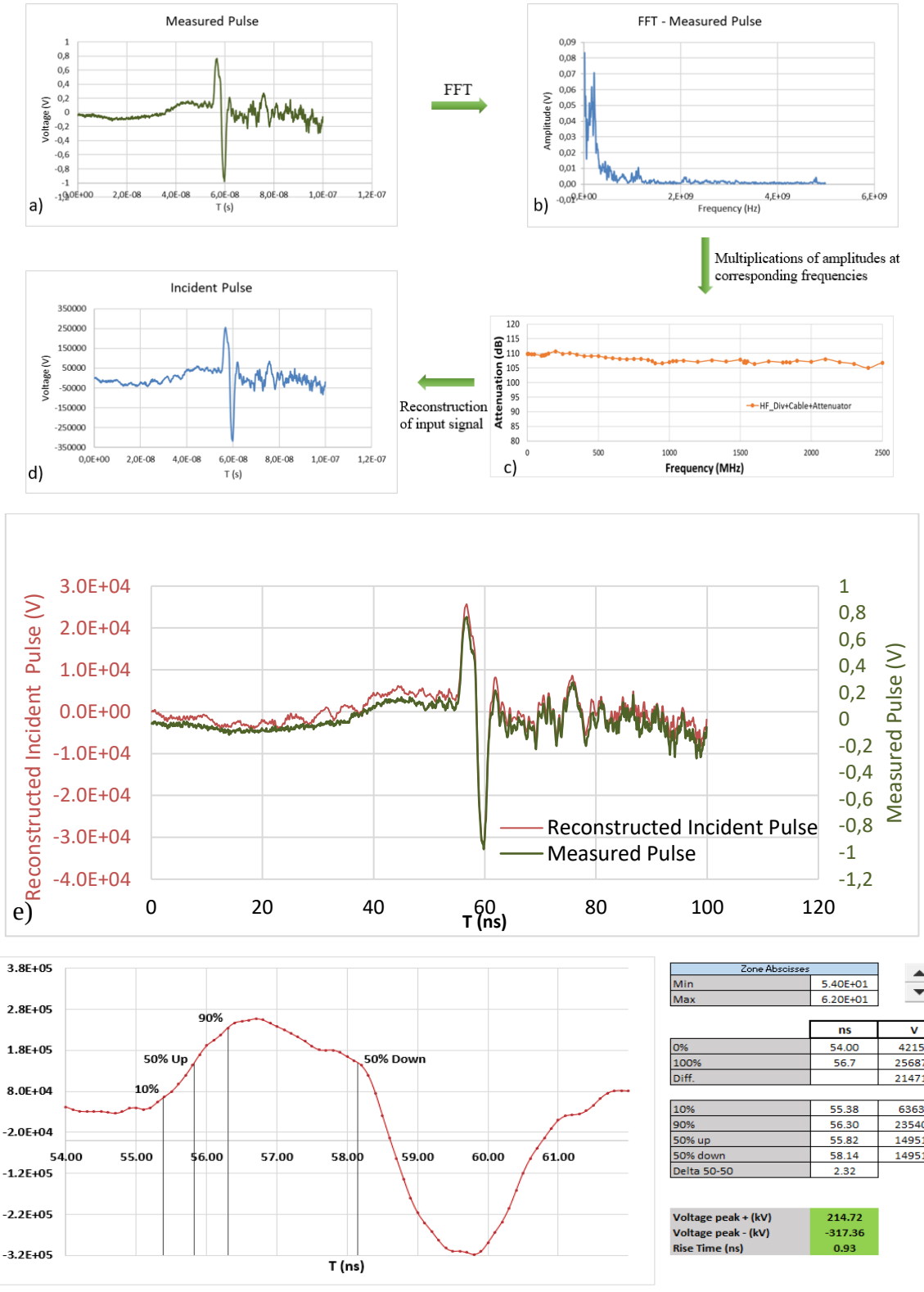

Fig.61. Bipolar pulse; a) measured pulse at the output of the HPPNS measurement system, b) FFT of the measured pulse, which is multiplied to the corresponding attenuations in c) the reconstructed +215/-317 kV input pulse generated by the Marx generator is presented in d) and e) superposition of the measured and reconstructed pulses and f) rise time and voltage peak measurements of the reconstructed incident pulse

The measurements presented in the Fig.59 to Fig.61 were obtained at a sampling rate of 25 GS/second. Moreover, during this measurement campaign, other pulses with rise times as low as 420 picoseconds (ps) were measured and some of them are presented in the Fig.62. In the Fig.62.a), a 298.5 kV pulse is measured with a rise time of 640 ps whereas in b) a voltage peak of 223 kV with a faster rise time of 430 ps. Similarly in c) and d), pulses with voltage peaks of 181 kV and 144 kV are measured with rise times of 420 ps and 430 ps respectively.

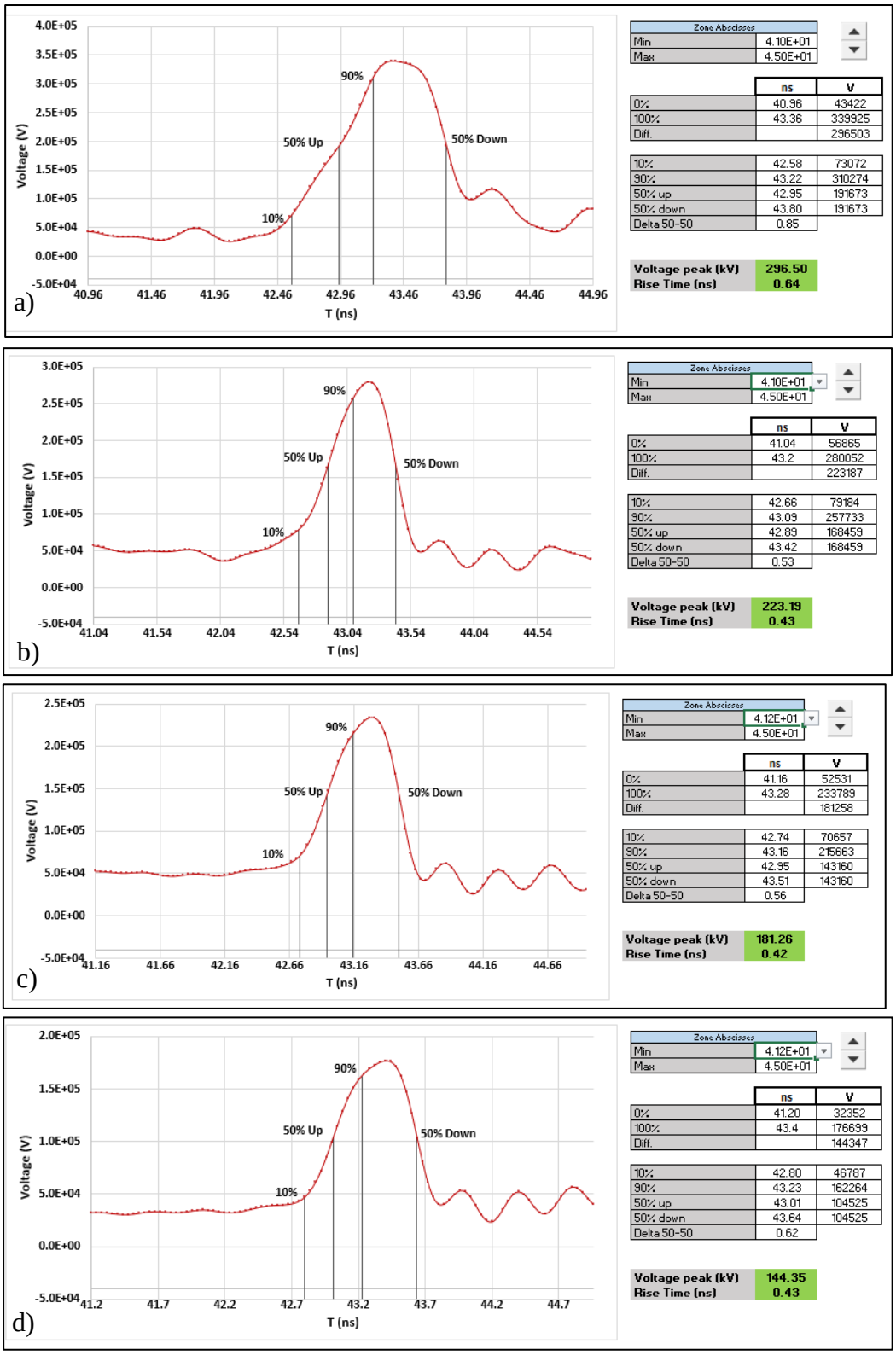

Fig. 62. Measured pulses; a) 299 kV pulse with rise time of 640 ps and full width at half maximum (FWHM) of 850 ps; b) 223 kV pulse with rise time of 430 ps and FWHM of 530 ps; c) 181 kV pulse with rise time of 420 ps and FWHM of 560 ps and d) 144 kV pulse with rise time of 430 ps and FWHM of 6200 ps.

The results presented in the Fig.59 to Fig.62, prove the capability of the HPPNS measurement system to measure voltage peaks as high as 300 kV and rise times as low as 420 ps. These measurements also demonstrate that the HPPNS measurement system is capable of withstanding voltage peaks of at least 300 kV. These measurements were carried out at these levels of voltages because of the limitation of the Marx generator to deliver higher voltage peaks on a 50 Ω load. These measurements confirm that the objectives fixed for the developed HPPNS measurement system, mentioned in the Table 3, is achieved in terms of pulse rise times and durations and partially achieved in terms of voltage amplitudes due to lack of an appropriate generator. However, the final performances of this measurement standard will be confirmed by the uncertainty budget, which is presented in the next section.

4.4. Traceability of the reconstructed pulses

4.4.1. Preliminary uncertainty budget for the voltage peak value

To ensure the traceability to the SI of the pulses measured through the HPPNS measurement system, a preliminary uncertainty budget is drafted. Since the measured pulse V_{mes} through the oscilloscope is a function of the division ratio *DR* of the HPPNS measurement system and the input high voltage pulse V_{in}, the reconstructed incident high voltage pulse is given by the equation:

$$V_{in} = V_{mes} \cdot DR \tag{43}$$

The combined standard uncertainty for the peak value of the reconstructed pulse is obtained from the specifications from the Guide to the expression of uncertainty in measurement [110]. The input variables in the equation (43) V_{mes} and *DR* are uncorrelated. Therefore, the combined standard uncertainty $u_c(V_{in})$ for the voltage peak of the reconstructed pulse can be written as:

$$u_c^2(V_{in}) = \sum_{i=1}^{N} \left(\frac{\partial V_{in}}{\partial x_i}\right)^2 \cdot u^2(x_i) \tag{44}$$

where, $x_i = V_{mes}$ (i=1) and *DR* (i=2).

Each $u(x_i)$ corresponds to the standard uncertainty of the influencing parameter x_i and partial derivatives of the equation (43) $\left(\frac{\partial V_{in}}{\partial x_i}\right)$. These partial derivatives are often called sensitivity coefficients and describe how the output estimate V_{in} varies with changes in the input estimates x_i. Therefore, from the equations (43) and (44) we can write:

$$u_c^2(V_{in}) = (DR)^2 \cdot u^2(V_{mes}) + (V_{mes})^2 \cdot u^2(DR) \tag{45}$$

Furthermore, from equation (43):

$$u_c^2(V_{in}) = \left(\frac{V_{in}}{V_{mes}}\right)^2 \cdot u^2(V_{mes}) + \left(\frac{V_{in}}{DR}\right)^2 \cdot u^2(DR) \tag{46}$$

$$\frac{u_c(V_{in})}{V_{in}} = \sqrt{\left(\frac{u(V_{mes})}{V_{mes}}\right)^2 + \left(\frac{u(DR)}{DR}\right)^2} \tag{47}$$

From the equation (47) the relative combined standard uncertainty of the reconstructed input pulse $u_r(V_{in})$ can be written as:

$$u_r(V_{in}) = \sqrt{(u_r(V_{mes}))^2 + (u_r(DR))^2} \quad (48)$$

where:

$u_r(V_{mes})$ is the relative standard uncertainty for the measured pulse
$u_r(DR)$ is the relative standard uncertainty on the division ratio

Both of these standard uncertainties depend upon the following uncertainty components:

Uncertainty components for the voltage peak value (*U*)

U1: Low voltage calibration uncertainty of the *DR*

U2: Extrapolation of the division ratio to high voltages

U3: Drift between two calibrations

U4: Errors of the digitizer

Therefore, the equation (48) can be rewritten as:

$$u_r(V_{in}) = \sqrt{(U1)^2 + (U2)^2 + (U3)^2 + (U4)^2} \quad (49)$$

4.4.1.1. Low voltage calibration uncertainty of the division ratio (U1)

The absolute expanded calibration uncertainty delivered by the calibration laboratory, for the attenuations of the HPPNS measurement system with a 20 dB supplementary attenuator and 10 meters of cable is **0.2 dB** with k=2,. This measurement uncertainty was obtained by the high frequency traceable method for the attenuation results as a function of frequency, presented in the Fig.55 of the section *4.2*.

The 0.2 dB of the uncertainty of the attenuation factor of the HPPNS measurement system corresponds to a variation of 2.3% of the voltage peak value. Therefore, the standard relative uncertainty of the calibration is:

$$U1 = \frac{2.3}{2}\ \% = 1.2\ \%$$

4.4.1.2. Extrapolation of the division ratio to high voltages (U2)

This uncertainty factor corresponds to the self-heating of the HPPNS measurement system during the application of a 500 kV pulse. As mentioned in the section *3.2*, a 500 kV pulse with a rise time of around 5 ns and full-width at half maximum (FWHM) value of almost 100 ns represents a total energy of $\boldsymbol{E}$ =330 J, which corresponds to 0.4% deviation in the resistance value of the 50 **Ω** ceramic resistor. The effect of this deviation was considered to be negligible on the division ratio. Similarly, taking into account low energy contents of the pulses to be measured, the heating effect on the other materials constituting the HPPNS measurement system, such as, aluminum, copper, PTFE and SiO_2 is equally considered to be negligible.

U2 = 0

4.4.1.3. Drift between two calibrations (U3)

As presented in the Fig.55, the difference between two calibrations at the interval of two months of the HPPNS measurement system is found to be 0.02%. Some more study has to be performed in order to evaluate its long term drift. Therefore, it was decided to calibrate the HPPNS measurement system before every use, which rends this component of uncertainty to be zero.

U3 = 0

4.4.1.4. Errors of the digitizer (U4)

An analysis of the errors based on the information given by the constructor in the datasheet has been performed for the oscilloscope *TEKTRONIX MSO6* of bandwidth of 6 GHz functioning at a sampling frequency of 25 GSamples/second. These errors include relative uncertainty of the voltage (V) measurement, offset effect, temperature effect, the drift, the bandwidth effect, non-linearity of ADC, frequency-sampling effect, resolution error (12-bits, maximum input voltage of 5.5V), the time base effect and the internal noise effect. The relative expanded uncertainty estimated of this component is ±2 % (k=2$\sqrt{3}$). Therefore, the relative standard uncertainty of this component is

$$U4 = \frac{2\%}{\sqrt{3}} = 1.2\ \%$$

These above mentioned components of the uncertainty for the voltage peak value are listed in the Table 6, where the combined standard uncertainty is the quadratic sum of all the uncertainty components with a coverage factor of k=1 and the expanded uncertainty is obtained by multiplying the combined standard uncertainty by a coverage factor of k=2, where the coverage factor is chosen on the basis of the level of confidence [110].

Table 6. Preliminary uncertainty budget for the voltage peak value

Component of uncertainty	Relative standard uncertainty
U1: Low voltage calibration uncertainty of the division ratio	1.2 %
U2: Extrapolation of the division ratio to high voltages	0
U3: Drift between two calibrations	0
U4: Errors of the digitizer	1.2 %
Combined standard relative uncertainty (k=1) $\sqrt{U_1^2 + U_2^2 + U_3^2 + U_4^2}$	**1.7 %**
Expanded relative uncertainty (k=2)	**3.4 %**

4.4.2. Preliminary uncertainty budget for temporal parameters

The main components of the uncertainty for the temporal parameters of the digitizer are is listed below:

T1: Calibration of digitizer in terms of rise times

T2: Time base of the digitizer

T3: Measurement of particular points (10 % and 90 %)

T4: Influence of the uncertainty of the peak value

These uncertainty components are detailed in the following sections.

4.4.2.1. Calibration of digitizer in terms of rise times (T1)

The absolute expanded calibration uncertainty (k=2) given by the calibration lab for the rise time is 40 ps. Therefore, the absolute standard uncertainty of this component is

T1 = 20 ps

4.4.2.2. Time base of the digitizer (T2)

For a digitizer functioning at the sampling rate of $25 \cdot 10^9$samples/second, this random error is estimated to be 40 ps. The absolute standard uncertainty obtained with a rectangular probability distribution law ($k = \sqrt{3}$) is

T2= 23.1 ps

4.4.2.3. Measurement of particular points (10 % and 90 %) (T3)

As for the T1, the absolute expanded uncertainty (k=2) of measurement for the time at 10 % and 90 % of peak value is 40 ps. Therefore, this uncertainty component is

T3= 20 ps

4.4.2.4. Influence of the uncertainty of the peak value (T4)

The uncertainty of the peak value influences the uncertainty of front time, for the fast rising pulses with rise times of few hundreds of ps. These influences were found to be less than 40 ps. The obtained uncertainty includes offset effect, temperature effect, the drift, the bandwidth effect, non-linearity of ADC, frequency-sampling effect, the time base effect and the internal noise effect. Through a rectangular probability distribution law ($k = \sqrt{3}$) absolute standard uncertainty is

T4 = 23.1 ps

These above mentioned components of the uncertainty for the temporal parameters are listed in the Table 7, where the combined standard uncertainty is the quadratic sum of all the uncertainty components with a coverage factor of k=1 and the expanded uncertainty is obtained by multiplying the combined standard uncertainty by a coverage factor of k=2.

Table 7. Preliminary uncertainty budget associated with the digitizer

Component of uncertainty	Absolute standard uncertainty (ps)
T1: Calibration of digitizer in terms of rise times	20
T2: Time base of the digitizer	23.1
T3: Measurement of particular points (10 % and 90 %)	20
T4: Influence of the uncertainty of the peak value	23.1
Combined standard uncertainty (k=1) $\sqrt{T_1^2 + T_2^2 + T_3^2 + T_4^2}$	**43.2**
Expanded uncertainty (k=2)	**86.4**

4.5. Conclusion

In this last chapter of the thesis, the experimental procedures for the characterization of the HPPNS measurement system are presented. Firstly, the characterizations were carried out for the different components, constituting the HPPNS measurement system, through a calibrated VNA and the results obtained were compared to the CST modelling results of each component in terms of S parameters and their respective phases. These results were found to be in good agreement with each other. Later, the complete HPPNS measurement system was characterized by two different methods, namely, VNA characterization and characterization through a traceable high frequency method. The results obtained from these two methods were compared to the CST modelling results and all of these results were found to be in good agreement with each other. These characterizations were carried out at low power levels and confirmed the bandwidth and the division ratio of the developed system. Furthermore, the HPPNS measurement system was characterized with a supplementary 20 dB attenuator and coaxial cables in order to increase the division ratio so that it could be used for high voltage characterizations. Different high voltage waveforms of voltage peaks as high as 300 kV and rise times as low as 420 ps were successfully measured through this system. An uncertainty budget is also presented.

These measurements prove that the HPPNS measurement system developed in this thesis is very well capable of measuring nanosecond and subnanosecond pulses of voltage peaks at least up to 300 kV. Moreover, the target uncertainty for the voltage peaks of 3% to 5%, which was fixed at the beginning of the project, was respected and the preliminary measurement uncertainties attained is of 3.4 % for voltage peaks and 87 ps for the temporal parameters. The Table 8 below resumes the targets, mentioned in the section *1.5*, and attained values in this thesis.

Table 8. Targeted and achieved values of the different pulse parameters in the thesis

Pulse parameters	**Target**		**Achieved**	
	Values	**Uncertainty (k=2)**	**Values**	**Uncertainty (k=2)**
Voltage amplitude (V)	$V \leq 500$ kV	3 % to 5 %	$V \leq 300$ kV	3.4 %
Rise time (t_r)	few hundreds of picoseconds to few nanoseconds	few hundreds of picoseconds (absolute uncertainty)	420 ps ≤ t_r ≤ 7.8 ns	87 ps
Duration (t_d)	$t_d \leq 100$ ns		530 ps ≤ t_d ≤ 16.3 ns	

GENERAL CONCLUSION

To ensure the traceability to the SI of the high pulsed power in the nanosecond and subnanosecond domain (HPPNS), a complete measure system is designed, simulated, characterized and tested. The system is capable of measuring high voltage pulses of amplitudes up to 500 kV with rise times as low as few hundreds of picoseconds. The developed system can be globally divided into four components: The voltage divider, the termination load, the high-voltage connectors and the transition cones.

The voltage divider is the central component of this measurement system as it permits the analysis of HPPNS waveforms through a calibrated oscilloscope by lowering the voltage amplitudes of the HPPNS waveforms to adequate levels which could be measured through an oscilloscope. From the different voltage divider principles presented, a calculable capacitive voltage divider based on the transmission line principle, CCVD, is developed with high-voltage male and female connectors at its main transmission line extremities and a Type-N connector at its low voltage output. These high voltage connectors are also developed in this thesis as the connectors capable of withstanding voltage peaks up to 500 kV are inexistent in the market. The CCVD is carefully designed to possess a high division ratio, a high bandwidth and linear phase responses. All these characteristics are mandatory for the measurements of the HPPNS waveforms without distortions. However, its performances in terms of measuring accurately and precisely the incident HPPNS waveforms depend also on the characteristics of the transmission line termination load since an inadequately matched line termination load could lead to a large amount of reflections and the measured waveform at the output of the CCVD could be misunderstood. A wideband 50 Ω line termination load with an inherent high-voltage female connector is developed and characterized. It has high insulation properties for voltage amplitudes up to 500 kV and a maximum reflection coefficient of -27 dB as a function of frequencies up to 2 GHz.

The characterization of the complete HPPNS measurement system was carried out in two steps. Firstly, the HPPNS measurement system was characterized at low levels of input power by two different methods, namely, VNA characterization and characterization through a SI traceable high frequency attenuation measurement method. The results obtained from these two methods were compared to the CST modelling results and all of these results were found to be in good agreement with each other. These characterizations demonstrated that the developed HPPNS measurement

system possess a high division ratio of around **85 dB** as a function of frequency, a bandwidth of **2 GHz** and **linear** phase responses. In order to attain the objective in terms of the measurements of voltage peaks levels up to 500 kV, a 20 dB, 7 GHz bandwidth commercial attenuator was added at the output of the CCVD and this whole system was re-characterized by both low power methods and the results obtained are as follows: almost **110 dB** of division ratio as function of frequency, a bandwidth of **2 GHz** and **linear** phase response. In the second characterization step, this system was tested at high power levels through a Max generator and pulse forming lines. **Different high voltage waveforms of voltage peaks as high as 300 kV and rise times as low as 420 picoseconds were successfully measured** through this system and an uncertainty budget is drafted. The measurement uncertainties for these high voltage measurements were calculated to be **3.4% for the voltage peaks** and **87 picoseconds** for the temporal parameters, which are completely conform to the objectives that were fixed at the beginning of the thesis project.

These measurements could be carried out only up to 300 kV of voltages amplitudes because of the limitation of the Marx generator to deliver higher voltage peaks on a 50 Ω load. However, the theoretical investigations presented demonstrate that the developed HPPNS measurement system can be very well used for voltage peaks up to 500 kV. This aspect still needs to be confirmed experimentally.

PERSPECTIVES

Future research is suggested in following aspects:

I. Measurements of the waveforms of voltage amplitudes beyond 300 kV in the nanosecond and subnanosecond domain should be performed to prove experimentally the efficiency of the HPPNS measurement system at least up to 500 kV.

II. Improvement of the measurement uncertainties through in-depth investigations of the factors influencing these latter.

III. Adaptation of the developed 50 Ω characteristic impedance HPPNS measurement system to other generation systems with different characteristic impedances.

IV. Study and improvement of the behavior of the developed HPPNS measurement system in terms of bandwidth beyond 2 GHz for the SI traceable measurement of the waveforms with rise times as fast as few tens of picoseconds. Indeed, at present, megavolt levels of voltage pulses has been reached with a simultaneous shortening of the rise time or duration to hundreds and tens of picoseconds [90], [111]–[113].

REFERENCES

[1] W. D. Prather, C. E. Baum, R. J. Torres, F. Sabath, and D. Nitsch, 'Survey of worldwide high-power wideband capabilities', *IEEE Trans. Electromagn. Compat.*, vol. 46, no. 3, pp. 335–344, Aug. 2004, doi: 10.1109/TEMC.2004.831826.

[2] A. Khamlichi, F. Garnacho, J. Hällström, A. P. Elg, and J. Rovira, 'CALIBRATION SETUP FOR TRACEABLE MEASUREMENTS OF VERY FAST TRANSIENTS', 21st International Symposium on High Voltage Engineering, Budapest, Hungary, August 26-30, 2019.

[3] E. Schamiloglu, R. J. Barker, M. Gundersen, and A. A. Neuber, 'Modern Pulsed Power: Charlie Martin and Beyond', *Proc. IEEE*, vol. 92, no. 7, pp. 1014–1020, Jul. 2004, doi: 10.1109/JPROC.2004.829058.

[4] L. Carin, J. Sichina, and J. F. Harvey, 'Microwave underground propagation and detection', *IEEE Trans. Microw. Theory Tech.*, vol. 50, no. 3, pp. 945–952, Mar. 2002, doi: 10.1109/22.989977.

[5] K. Martin and R. Carsten, '3D Reconstruction of Buildings and Vegetation from Synthetic Aperture Radar (SAR) Images', *IAPR Workshop on Machine Vision Application, MVA*, 1998.

[6] S. Vitebskiy, L. Carin, M. A. Ressler, and F. H. Le, 'Ultra-wideband, short-pulse ground-penetrating radar: simulation and measurement', *IEEE Trans. Geosci. Remote Sens.*, vol. 35, no. 3, pp. 762–772, May 1997, doi: 10.1109/36.581999.

[7] J.-A. Nollet, *Recherches sur les causes particulières des phénomènes électriques, Et sur les effets nuisibles ou avantageux qu'on peut en attendre*. Chez H.L. Guerin & L.F. Delatour, 1749.

[8] A. J. H. Sale and W. A. Hamilton, 'Effects of high electric fields on microorganisms: I. Killing of bacteria and yeasts', *Biochim. Biophys. Acta BBA - Gen. Subj.*, vol. 148, no. 3, pp. 781–788, Dec. 1967, doi: 10.1016/0304-4165(67)90052-9.

[9] B. Geboers *et al.*, 'High-Voltage Electrical Pulses in Oncology: Irreversible Electroporation, Electrochemotherapy, Gene Electrotransfer, Electrofusion, and Electroimmunotherapy', *Radiology*, vol. 295, no. 2, pp. 254–272, May 2020, doi: 10.1148/radiol.2020192190.

[10] M. OKINO and H. MOHRI, 'EFFECTS OF A HIGH-VOLTAGE ELECTRICAL IMPULSE AND AN ANTICANCER DRUG ON IN VIVO GROWING TUMORS', *Japanese Journal of Cancer Research GANN*, pp. 1319–1321, 1987.

[11] T. Kotnik and D. Miklavcic, 'Theoretical evaluation of voltage inducement on internal membranes of biological cells exposed to electric fields', *Biophys. J.*, vol. 90, no. 2, pp. 480–491, Jan. 2006, doi: 10.1529/biophysj.105.070771.

[12] 'Revision of Part 15 of the Commission's Rules Regarding Ultra WideBand Transmission Systems', *Federal Communications Commission*, Dec. 27, 2015. https://www.fcc.gov/document/revision-part-15-commissions-rules-regarding-ultra-wideband-7 (accessed Aug. 03, 2022).

[13] A. H. Alghanimi, *Medical Application of Ultra-Wideband Technology*. IntechOpen, 2021. doi: 10.5772/intechopen.93577.

[14] International Commission on Non-Ionizing Radiation Protection (ICNIRP), 'Guidelines for limiting exposure to time-varying electric, magnetic, and electromagnetic fields (up to 300 GHz). International Commission on Non-Ionizing Radiation Protection', *Health Phys.*, vol. 74, no. 4, pp. 494–522, Apr. 1998.
[15] E. M. Staderini, 'UWB radars in medicine', *IEEE Aerosp. Electron. Syst. Mag.*, vol. 17, no. 1, pp. 13–18, Jan. 2002, doi: 10.1109/62.978359.
[16] M. G. Mazarakis and R. B. Spielman, 'A compact, high-voltage e-beam pulser', in *Digest of Technical Papers. 12th IEEE International Pulsed Power Conference. (Cat. No.99CH36358)*, Monterey, CA, USA, 1999, vol. 1, pp. 412–415. doi: 10.1109/PPC.1999.825498.
[17] W. A. Stygar *et al.*, 'Impedance-matched Marx generators', *Phys. Rev. Accel. Beams*, vol. 20, no. 4, p. 040402, Apr. 2017, doi: 10.1103/PhysRevAccelBeams.20.040402.
[18] M. B. Taylor *et al.*, 'Operation of a 500 kV, 4 kA Marx generator at 500 Hz rep-rate', in *2014 IEEE International Power Modulator and High Voltage Conference (IPMHVC)*, Santa Fe, NM, USA, Jun. 2014, pp. 377–379. doi: 10.1109/IPMHVC.2014.7287288.
[19] F. Lassalle *et al.*, 'Development and Test of a 400-kV PFN Marx With Compactness and Rise Time Optimization', *IEEE Trans. Plasma Sci.*, vol. 46, no. 10, pp. 3313–3319, Oct. 2018, doi: 10.1109/TPS.2018.2837344.
[20] J. C. Martin, 'Nanosecond pulse techniques', *Proc. IEEE*, vol. 80, no. 6, pp. 934–945, Jun. 1992, doi: 10.1109/5.149456.
[21] M. M. Kekez, 'Simple sub-50-ps rise-time high voltage generator', *Rev. Sci. Instrum.*, vol. 62, no. 12, Art. no. 12, Dec. 1991, doi: 10.1063/1.1142182.
[22] B. Cadilhon *et al.*, 'High Pulsed Power Sources for Broadband Radiation', *IEEE Trans. Plasma Sci.*, vol. 38, no. 10, pp. 2593–2603, Oct. 2010, doi: 10.1109/TPS.2010.2042732.
[23] A. S. Eljugmani and M. S. Kamarudin, 'DEVELOPMENT OF PORTABLE 1O STAGES MARX GENERATOR', vol. 11, no. 7, p. 7, 2016.
[24] R. Bischoff, R. Charon, J.-P. Duperoux, and B. Martin, 'Study of an Ultra-Compact, Repetitive Marx Generator for High-Power Microwave Applications', *Proceedings of the 2nd Euro-Asian Pulsed Power Conference, Vilnius, Lithuania,September 22–26, 2008*.
[25] B. Martin, P. Raymond, and J. Wey, 'New model for ultracompact coaxial Marx pulse generator simulations', *Rev. Sci. Instrum.*, vol. 77, no. 4, Art. no. 4, Apr. 2006, doi: 10.1063/1.2194087.
[26] E. N. Abdulin, Y. P. Bazhenov, V. N. Kiselyov, and A. V. Morozov, 'High-power Current Pulse Generator for Inductive-Resistive Load Operation', *Poster Sess.*, p. 4.
[27] S. M. Turnbull, S. J. MacGregor, and J. A. Harrower, 'A PFN Marx generator based on high-voltage transmission lines', *Meas. Sci. Technol.*, vol. 11, no. 4, pp. N51–N55, Apr. 2000, doi: 10.1088/0957-0233/11/4/401.

[28] S. V. Tewari *et al.*, 'Development and Analysis of PFN Based Compact Marx Generator Using Finite Integration Technique for an Antenna Load', *IEEE Trans. Plasma Sci.*, vol. 41, no. 10, pp. 2684–2690, Oct. 2013, doi: 10.1109/TPS.2013.2279483.

[29] M. M. Kekez, J. LoVetri, A. S. Podgorski, J. G. Dunn, and G. Gibson, 'A 60 joule, 600kv, 1ns rise-time marx system', in *7th Pulsed Power Conference*, Monterey, CA, 1989, pp. 123–127. doi: 10.1109/PPC.1989.767439.

[30] R. Vezinet *et al.*, 'Development of a compact narrow-band high power microwave system', in *2016 IEEE International Power Modulator and High Voltage Conference (IPMHVC)*, San Francisco, CA, USA, Jul. 2016, pp. 132–135. doi: 10.1109/IPMHVC.2016.8012912.

[31] S. Bindu, S. B. Umbarkar, H. A. Mangalvedekar, A. Sharma, P. C. Saroj, and K. C. Mittal, 'Peaking Capacitor Parameter Evaluation With Transfer Function Model', *IEEE Trans. Plasma Sci.*, vol. 42, no. 2, pp. 336–339, Feb. 2014, doi: 10.1109/TPS.2013.2294344.

[32] S. Bindu, H. A. Mangalvedekar, A. Sharma, P. C. Saroj, D. P. Chakravarthy, and A. K. Ray, 'Development of Transfer Function Model and Analysis of the Peaking Capacitor and Switch', *IEEE Trans. Plasma Sci.*, vol. 41, no. 8, pp. 2415–2420, Aug. 2013, doi: 10.1109/TPS.2013.2268944.

[33] L. Yuan, L. X. Ping, L. Jing, H. Hui, W. Yongwei, and Z. Fuxin, 'High-voltage multi-pulse generator based on series-PFL', in *2007 16th IEEE International Pulsed Power Conference*, Jun. 2007, vol. 2, pp. 1332–1334.

[34] L. Pecastaing *et al.*, 'Compact self Marx generator with integrated PFL for an ultra-wideband source', *J.- Korean Phys. Soc.*, vol. 59, pp. 3463–3467, Jan. 2011.

[35] S. J. MacGregor, S. M. Turnbull, F. A. Tuema, and J. Harrower, 'The performance of a simple PFN Marx generator', in *Proceedings of 1996 International Power Modulator Symposium*, Jun. 1996, pp. 194–197. doi: 10.1109/MODSYM.1996.564484.

[36] Z. Zhang, L. Yang, and W. Zhan, 'Optimization of PFN-Marx generator', *High Power Laser and Particle Beams, 2018, 30: 055006.*

[37] G. N. Glasoe and J. V. Lebacqz, 'Pulse generators', *MIT Rad Lab Ser N. Y. NIcGraw-Hill*, p. 755, 1948.

[38] B. H. McGuyer, 'Note: Investigation of a Marx generator imitating a Tesla transformer', *Rev. Sci. Instrum.*, vol. 89, no. 8, p. 086102, Aug. 2018, doi: 10.1063/1.5035286.

[39] Mankowski, J. Dickens, M. Kristiansen, J. Lehr, W. Prather, and J. Gaudet, 'Subnanosecond corona inception in an ultrawideband environment', *IEEE Trans. Plasma Sci.*, vol. 30, no. 3, pp. 1211–1214, Jun. 2002, doi: 10.1109/TPS.2002.801655.

[40] L. Pecastaing, M. Rivaletto, A. S. de Ferron, R. Pecquois, and B. M. Novac, 'Development of a 0.6-MV Ultracompact Magnetic Core Pulsed Transformer for High-Power Applications', *IEEE Trans. Plasma Sci.*, vol. 46, no. 1, pp. 156–166, Jan. 2018, doi: 10.1109/TPS.2017.2781620.

[41] R. Pecquois *et al.*, 'Synchronized spark gaps combined to multi-primary windings resonant transformer for wideband applications', in *2010 IEEE International Power Modulator and High Voltage Conference*, Atlanta, GA, USA, May 2010, pp. 353–356. doi: 10.1109/IPMHVC.2010.5958366.

[42] G. A. Mesyats *et al.*, 'Repetitively pulsed high-current accelerators with transformer charging of forming lines', *Laser Part. Beams*, vol. 21, no. 2, pp. 197–209, Apr. 2003, doi: 10.1017/S0263034603212076.

[43] S. Li, J.-M. Gao, H.-W. Yang, and B.-L. Qian, 'A high-voltage, long-pulse generator based on magnetic pulse compressor and Blumlein-type rolled strip pulse forming line', *Laser Part. Beams*, vol. 33, no. 3, pp. 511–518, Sep. 2015, doi: 10.1017/S0263034615000567.

[44] R. Pecquois *et al.*, 'Compact 600 kV multi-primary windings resonant transformer to drive an electromagnetic source', in *2012 IEEE International Power Modulator and High Voltage Conference (IPMHVC)*, San Diego, CA, USA, Jun. 2012, pp. 633–636. doi: 10.1109/IPMHVC.2012.6518824.

[45] R. Pecquois, L. Pecastaing, M. Rivaletto, A. S. De Ferron, and R. Vezinet, 'MOUNA: An Autonomous, Compact, High-Power, and Wideband Electromagnetic Source Based on a Novel Resonant Pulsed Transformer', *IEEE Trans. Plasma Sci.*, vol. 40, no. 5, pp. 1407–1415, May 2012, doi: 10.1109/TPS.2012.2189138.

[46] T. Maysonnave *et al.*, 'Investigation of Switch Designs for the Dynamic Load Current Multiplier Scheme on the SPHYNX Microsecond Linear Transformer Driver', *IEEE Trans. Plasma Sci.*, vol. 42, no. 10, pp. 2974–2980, Oct. 2014, doi: 10.1109/TPS.2014.2313372.

[47] J. Mankowski, J. Dickens, and M. Kristiansen, 'High voltage subnanosecond breakdown', *IEEE Trans. Plasma Sci.*, vol. 26, no. 3, pp. 874–881, Jun. 1998, doi: 10.1109/27.700858.

[48] P. Sarkar, S. W. Braidwood, I. R. Smith, B. M. Novac, R. A. Miller, and R. M. Craven, 'A Compact Battery-Powered Half-Megavolt Transformer System for EMP Generation', *IEEE Trans. Plasma Sci.*, vol. 34, no. 5, pp. 1832–1837, Oct. 2006, doi: 10.1109/TPS.2006.881886.

[49] M. Lin, J. Sun, X. Zhan, X. Yao, and H. Zhou, 'Development of a compact high-voltage pulser for hypervelocity microparticles injector', *Rev. Sci. Instrum.*, vol. 90, no. 8, p. 083305, Aug. 2019, doi: 10.1063/1.5095435.

[50] J. Mankowski, J. Dickens, and M. Kristiansen, 'A subnanosecond high voltage pulser for the investigation of dielectric breakdown', in *Digest of Technical Papers. 11th IEEE International Pulsed Power Conference (Cat. No.97CH36127)*, Jun. 1997, vol. 1, pp. 549–554 vol.1. doi: 10.1109/PPC.1997.679394.

[51] 'IEEE Standard for Pulse Transformers', *ANSIIEEE Std 390-1987*, pp. 1–32, Oct. 1987, doi: 10.1109/IEEESTD.1987.79640.

[52] D. Bortis, G. Ortiz, and J. W. Kolar, 'Design Procedure for Compact Pulse Transformers with Rectangular Pulse Shape and Fast Rise Times', *IEEE Transactions on Dielectrics and Electrical Insulation Vol. 18, No. 4; August 2011*.

[53] A. R. ONDREJKA, ‘Peak Pulse Voltage Measurement (Baseband Pulse)’, *PROCEEDINGS OF THE IEEE, VOL. 55, NO. 6, JUNE 1967*.
[54] L. Zhang, L. Sun, Y. H. Han, S. Wang, C. Guo, and C. X. Wang, ‘Development of a Broadband Capacitive Voltage Divider for Measuring Nanosecond Impulse’, in *2018 2nd IEEE Conference on Energy Internet and Energy System Integration (EI2)*, Beijing, Oct. 2018, pp. 1–6. doi: 10.1109/EI2.2018.8582076.
[55] M. R. Ulmaskulov, S. A. Shunailov, K. A. Sharypov, and E. M. Ulmaskulov, ‘Picosecond high-voltage pulse measurements’, *Rev. Sci. Instrum.*, vol. 92, no. 3, Art. no. 3, Mar. 2021, doi: 10.1063/5.0028419.
[56] D. G. Pellinen and M. S. Di Capua, ‘Two-megavolt divider for pulsed high voltages in vacuum’, *Rev. Sci. Instrum.*, vol. 51, no. 1, pp. 70–73, Jan. 1980, doi: 10.1063/1.1136021.
[57] A.-P. Elg, S. Passon, J. Meisner, and J. Hällström, ‘High Voltage Topologies for Very Fast Transient Measurements’, in *Proceedings of the 21st International Symposium on High Voltage Engineering*, vol. 598, B. Németh, Ed. Cham: Springer International Publishing, 2020, pp. 1316–1327. doi: 10.1007/978-3-030-31676-1_123.
[58] W. He, H. Yin, A. D. R. Phelps, A. W. Cross, and S. N. Spark, ‘Study of a fast, high-impedance, high-voltage pulse divider’, *Rev. Sci. Instrum.*, vol. 72, no. 11, pp. 4266–4269, Nov. 2001, doi: 10.1063/1.1408937.
[59] Z. Li, ‘Improved CuSO4 HV pulse divider’, *Rev. Sci. Instrum.*, vol. 59, no. 7, pp. 1244–1245, Jul. 1988, doi: 10.1063/1.1139706.
[60] D. G. Pellinen, Q. Johnson, and A. Mitchell, ‘A picosecond risetime high voltage divider’, *Rev. Sci. Instrum.*, vol. 45, no. 7, pp. 944–946, Jul. 1974, doi: 10.1063/1.1686773.
[61] D. G. Pellinen and I. Smith, ‘A Reliable Multimegavolt Voltage Divider’, *Rev. Sci. Instrum.*, vol. 43, no. 2, pp. 299–301, Feb. 1972, doi: 10.1063/1.1685617.
[62] F. F. Mazda, *Electronic Instruments and Measurement Techniques*, Cambridge University Press, New York, New Rochelle, Melbourne, Sydney. 1987.
[63] I. A. D. Lewis and F. H. Wells, *Millimicrosecond Pulse Techniques*, Pergamon Press Ltd., London. 1954. Accessed: Oct. 01, 2022.
[64] S. Jayaram, X. Xu, and J. D. Cross, ‘High divider ratio fast response capacitive dividers for high voltage pulse measurements’, in *IAS ’95. Conference Record of the 1995 IEEE Industry Applications Conference Thirtieth IAS Annual Meeting*, Orlando, FL, USA, 1995, vol. 2, pp. 1201–1205. doi: 10.1109/IAS.1995.530436.
[65] W. A. Edson and G. N. Oetzel, ‘Capacitance voltage divider for high-voltage pulse measurement’, *Rev. Sci. Instrum.*, vol. 52, no. 4, pp. 604–606, Apr. 1981, doi: 10.1063/1.1136644.
[66] M. M. Brady and K. G. Dedrick, ‘High-Voltage Pulse Measurement with a Precision Capacitive Voltage Divider’, *Review of Scientific Instruments 33, 1421 (1962);*, p. 33, Dec. 29, 2004.
[67] R. Pecquois *et al.*, ‘Novel concept for a compact and inexpensive 0.5 MV capacitive probe’, 4th Euro-Asian Pulsed Power Conference, 2012.

[68] R. Pecquois *et al.*, 'Simple and compact capacitive voltage probe for measuring voltage impulses up to 0.5 MV', *Rev. Sci. Instrum.*, vol. 83, no. 3, p. 035001, Mar. 2012, doi: 10.1063/1.3690906.
[69] J. Wang, W. Ding, and A. Qiu, 'Capacitive sensor for fast pulsed voltage monitor in transmission line', *Rev. Sci. Instrum.*, vol. 90, no. 3, Art. no. 3, Mar. 2019, doi: 10.1063/1.5050276.
[70] R. D. Shah, R. J. Cliffe, P. Senior, B. M. Novac, and I. R. Smith, 'An ultrafast probe for high-voltage pulsed measurements', in *PPPS-2001 Pulsed Power Plasma Science 2001. 28th IEEE International Conference on Plasma Science and 13th IEEE International Pulsed Power Conference. Digest of Papers (Cat. No.01CH37251)*, Las Vegas, NV, USA, 2001, vol. 2, pp. 1020–1023. doi: 10.1109/PPPS.2001.1001716.
[71] G. E. Leavitt, J. D. Shipman, and I. M. Vitkovitsky, 'Ultrafast High Voltage Probe', *Rev. Sci. Instrum.*, vol. 36, no. 9, pp. 1371–1372, Sep. 1965, doi: 10.1063/1.1719905.
[72] B. Cadilhon, 'Etude et réalisation d'un ensemble autonome d'émission d'ondes électromagnétiques de forte puissance', p. 281, 2008.
[73] C. A. Ekdahl, 'Capacitively-coupled inductive sensors for measurements of pulsed currents and pulsed magnetic fields', *Rev. Sci. Instrum.*, vol. 51, no. 12, pp. 1649–1651, Dec. 1980, doi: 10.1063/1.1136141.
[74] C. A. Ekdahl, 'Voltage and current sensors for a high-density z-pinch experiment', *Rev. Sci. Instrum.*, vol. 51, no. 12, pp. 1645–1648, Dec. 1980, doi: 10.1063/1.1136140.
[75] R. Kumar, B. M. Novac, and I. R. Smith, 'Simple, Noninvasive and Wide-Band Current and Voltage Sensors for Use with Coaxial Cables', *16th IEEE International Pulsed Power Conference*, 2007, pp. 486-489, doi: 10.1109/PPPS.2007.4651887.
[76] T. C. Wagoner *et al.*, 'Differential-output B -dot and D -dot monitors for current and voltage measurements on a 20-MA, 3-MV pulsed-power accelerator', *Phys. Rev. Spec. Top. - Accel. Beams*, vol. 11, no. 10, p. 100401, Oct. 2008, doi: 10.1103/PhysRevSTAB.11.100401.
[77] L. Wang, J. Han, M. Li, X. Zhang, T. Sun, and T. Lei, 'A compact capacitive probe for high-voltage diagnostic in Z-pinches', *Rev. Sci. Instrum.*, vol. 84, no. 3, p. 033504, Mar. 2013, doi: 10.1063/1.4797460.
[78] M. Favre, H. Chuaqui, A. M. Leñero, E. Wyndham, and P. Choi, 'A miniature capacitive probe array for transient high voltage capillary discharges', *Rev. Sci. Instrum.*, vol. 72, no. 4, pp. 2186–2190, Apr. 2001, doi: 10.1063/1.1359191.
[79] Jin-Liang Liu, Bing Ye, Tian-Wen Zhan, Jia-Huai Feng, Jian-De Zhang, and Xin-Xin Wang, 'Coaxial Capacitive Dividers for High-Voltage Pulse Measurements in Intense Electron Beam Accelerator With Water Pulse-Forming Line', *IEEE Trans. Instrum. Meas.*, vol. 58, no. 1, pp. 161–166, Jan. 2009, doi: 10.1109/TIM.2008.927195.

[80] P. Choi and M. Favre, ‘A fast capacitive voltage monitor for low impedance pulse lines’, in *Digest of Technical Papers. Tenth IEEE International Pulsed Power Conference*, Jul. 1995, vol. 2, pp. 880–885 vol.2. doi: 10.1109/PPC.1995.599723.
[81] S. W. Lim, C. Cho, Y. S. Jin, Y. B. Kim, and Y. Roh, ‘Design and Test of an Electric Field Sensor for the Measurement of High-Voltage Nanosecond Pulses’, *IEEE Trans. Plasma Sci.*, vol. 41, no. 10, pp. 2946–2950, Oct. 2013, doi: 10.1109/TPS.2013.2281052.
[82] M. BLANCHET, ‘Atténuateurs d’impulsion haute tension et de haut courant’
[83] ‘SI Brochure: The International System of Units (SI)’, 2019.
[84] *International vocabulary of metrology - Basic and general concepts and associated terms (VIM)*, 3rd ed., vol. JCGM 200:2012. BIPM, 2012.
[85] ‘METROLOGY - IN SHORT 3rd Edition’. EURAMET. [Online]. Available: https://www.euramet.org/publications-media-centre/documents/metrology-in-short
[86] ‘KCBD database for Pulsed High Voltage and Current Traceability, BIPM’. https://www.bipm.org/kcdb/cmc/search?domain=PHYSICS&areaId=2&keywords=&specificPart.branch=7&specificPart.service=22&specificPart.subService=52&specificPart.individualService=-1&_countries=1&publicDateFrom=&publicDateTo=&unit=&minValue=&maxValue=&minUncertainty=&maxUncertainty.
[87] T. Huiskamp, F. J. C. M. Beckers, E. J. M. van Heesch, and A. J. M. Pemen, ‘B-Dot and D-Dot Sensors for (Sub)Nanosecond High-Voltage and High-Current Pulse Measurements’, *IEEE Sens. J.*, vol. 16, no. 10, pp. 3792–3801, May 2016, doi: 10.1109/JSEN.2016.2530841.
[88] R. A. Serway and J. Jewett, *Physics for Scientists and Engineers with Modern Physics*. Brooks/Cole; International ed of 9th revised ed édition (1 février 2013).
[89] J. J. MANKOWSKI, ‘HIGH VOLTAGE SUBNANOSECOND DIELECTRIC BREAKDOWN’, Graduate Faculty of Texas Tech University, 1997.
[90] M. R. Ulmaskulov, S. A. Shunailov, K. A. Sharypov, and E. M. Ulmaskulov, ‘Picosecond high-voltage pulse measurements’, *Rev. Sci. Instrum.*, vol. 92, no. 3, p. 034701, Mar. 2021, doi: 10.1063/5.0028419.
[91] S. Awan, B. Kibble, and J. Schurr, *Coaxial Electrical Circuits for Interference-Free Measurements*, Institution of Engineering and Technology. 2011.
[92] K. A. Zheltov, *Picosecond High-Current Electron Accelerators*, Energoatomizdat. Moscow, 1991.
[93] Mistry, K.K., Lazaridis, P.I., Zaharis, Z.D. et al. *Time and Frequency Domain Simulation, Measurement and Optimization of Log-Periodic Antennas*. Wireless Pers Commun 107, 771–783 (2019). https://doi.org/10.1007/s11277-019-06299-w.
[94] T. Weiland, M. Timm, and I. Munteanu, ‘A practical guide to 3-D simulation’, *IEEE Microw. Mag.*, vol. 9, no. 6, pp. 62–75, Dec. 2008, doi: 10.1109/MMM.2008.929772.
[95] M. Steer, ‘Microwave and RF Design: Networks’, *Open Textbook Library*, 2019. https://open.umn.edu/opentextbooks/textbooks/756 (accessed Oct. 18, 2022).

[96] A. M. Nicolson and G. F. Ross, ‘Measurement of the Intrinsic Properties of Materials by Time-Domain Techniques’, *IEEE Trans. Instrum. Meas.*, vol. 19, no. 4, pp. 377–382, Nov. 1970, doi: 10.1109/TIM.1970.4313932.
[97] G. A. Mesyats, S. D. Korovin, V. V. Rostov, V. G. Shpak, and M. I. Yalandin, ‘The RADAN series of compact pulsed power Generators and their applications’, *Proc. IEEE*, vol. 92, no. 7, pp. 1166–1179, Jul. 2004, doi: 10.1109/JPROC.2004.829005.
[98] K. Liu, Q. Hu, J. Qiu, and H. Xiao, ‘A high repetition rate nanosecond pulsed power supply for nonthermal plasma generation’, *IEEE Trans. Plasma Sci.*, vol. 33, no. 4, pp. 1182–1185, Aug. 2005, doi: 10.1109/TPS.2005.852404.
[99] L. Pecastaing, J. Paillol, T. Reess, A. Gibert, and P. Domens, ‘Very Fast Rise-Time Short-Pulse High-Voltage Generator’, *IEEE Trans. Plasma Sci.*, vol. 34, no. 5, pp. 1822–1831, Oct. 2006, doi: 10.1109/TPS.2006.883346.
[100] S. K. Lyubutin, S. N. Rukin, B. G. Slovikovsky, and S. N. Tsyranov, ‘High-Power Ultrafast Current Switching by a Silicon Sharpener Operating at an Electric Field Close to the Threshold of the Zener Breakdown’, *IEEE Trans. Plasma Sci.*, vol. 38, no. 10, pp. 2627–2632, Oct. 2010, doi: 10.1109/TPS.2010.2045396.
[101] A. Pokryvailo, Y. Yankelevich, and M. Shapira, ‘A compact source of subgigawatt subnanosecond pulses’, *IEEE Trans. Plasma Sci.*, vol. 32, no. 5, pp. 1909–1918, Oct. 2004, doi: 10.1109/TPS.2004.835943.
[102] C. Spikings, N. Seddon, T. Bearpark, and R. Perks, ‘High performance attenuators’, in *IEE Symposium on Pulsed Power ’99 (Digest No. 1999/030)*, Apr. 1999, p. 15/1-15/6.
[103] J. E. Dolan, H. R. Bolton, and A. J. Shapland, ‘A 50 /spl Omega/, 50 kV ceramic disc coaxial load’, in *Digest of Technical Papers. Tenth IEEE International Pulsed Power Conference*, Jul. 1995, vol. 2, pp. 1443–1448 vol.2. doi: 10.1109/PPC.1995.599820.
[104] I. A. Harris, ‘The theory and design of coaxial resistor mounts for the frequency band 0–4000 Mc/s’, *Proc. IEE - Part C Monogr.*, vol. 103, no. 3, pp. 1–10, Mar. 1956, doi: 10.1049/pi-c.1956.0001.
[105] A. Tag, J. Leinhos, G. Hechtfischer, M. Leibfritz, and T. Eibert, ‘Design, simulation, and fabrication of broadband coaxial matched loads for the frequency range from 0 to 110 GHz’, *Int. J. Microw. Wirel. Technol.*, vol. 6, no. 3–4, pp. 297–304, Jun. 2014, doi: 10.1017/S1759078714000142.
[106] C. Kohn, ‘The Radio Frequency Coaxial Resistor Using a Tractorial Jacket’, *Proc. IRE*, vol. 43, no. 8, pp. 951–960, 1955, doi: 10.1109/JRPROC.1955.278202.
[107] ‘E5071C ENA Vector Network Analyzer’. Keysight (formely Agilent’s Electronic Measurement).
[108] T. Wu, ‘Precision measurement of attenuation and phase-shift at microwave and millimeter-wave frequencies’, Doctoral thesis, 2012.
[109] L. Ariztia *et al.*, ‘Development and Test of a 500-kV Compact Marx Generator Operating at 100-Hz PRF’, *IEEE Trans. Plasma Sci.*, vol. 50, no. 9, pp. 3123–3130, Sep. 2022, doi: 10.1109/TPS.2022.3192286.

[110] *Evaluation of measurement data — Guide to the expression of uncertainty in measurement (GUM)*. JCGM 100:2008 BIPM.

[111] G. A. Mesyats *et al.*, 'Formation of 1.4 MeV runaway electron flows in air using a solid-state generator with 10 MV/ns voltage rise rate', *Appl. Phys. Lett.*, vol. 112, no. 16, p. 163501, Apr. 2018, doi: 10.1063/1.5025751.

[112] M. R. Ulmaskulov *et al.*, 'Four-channel generator of 8-GHz radiation based on gyromagnetic non-linear transmitting lines', *Rev. Sci. Instrum.*, vol. 90, no. 6, p. 064703, Jun. 2019, doi: 10.1063/1.5091075.

[113] M. R. Ulmaskulov, S. A. Shunailov, K. A. Sharypov, and M. I. Yalandin, 'Multistage converter of high-voltage subnanosecond pulses based on nonlinear transmission lines', *J. Appl. Phys.*, vol. 126, no. 8, p. 084504, Aug. 2019, doi: 10.1063/1.5110438.